Investigation of High-Frequency Perturbations of the Surface Geomagnetic Field

by

Brett A. McCuen

A dissertation submitted in partial fulfillment
of the requirements for the degree of
Doctor of Philosophy
(Climate and Space Sciences and Engineering)
in the University of Michigan
2023

Doctoral Committee:

Professor Mark B. Moldwin, Chair
Associate Professor Branko Kerkez
Professor Michael W. Liemohn
Professor James A. Slavin

Brett A. McCuen

bmccuen@umich.edu

ORCID iD: 0000-0001-7389-6037

ACKNOWLEDGMENTS

This dissertation research was supported by the National Science Foundation (NSF) Division of Atmospheric and Geospace Sciences (AGS) grants 2013433 and 1848724 and the National Aeronautics and Space Administration (NASA) Living With a Star (LWS) grant 80NSSC20K1779. I would like to give immense thanks to my mentors and co-authors throughout the research of this dissertation: Dr. Mark B. Moldwin, Dr. Mark J. Engebretson, Dr. Erik S. Steinmetz, Dr. James M. Weygand, and Dr. Yukitoshi Nishimura. Special thanks goes to the dissertation committee members for their guidance and review of this research: Dr. Branko Kerkez, Dr. Michael W. Liemohn and Dr. James A. Slavin.

This research would not be possible without access to many high-quality, open-source data bases. I gratefully acknowledge: the MACCS team (space.augsburg.edu/maccs/, MACCS is operated by the University of Michigan and Augsburg University and funded by the U.S. NSF via grants AGS-2013433 and AGS-2013648), the SuperMAG collaborators (supermag.jhuapl.edu/), INTERMAGNET for promoting high standards of magnetic observatory practice (www.intermagnet.org), the Geological Survey of Canada (geomag.nrcan.gc.ca/obs/canmos-en.php), I.R. Mann, D.K. Milling and the rest of the CARISMA team for data (www.carisma.ca/), the Canadian Space Agency for support of AUTUMNX(autumn.athabascau.ca/), NASA contract NAS5-02099 and V. Angelopoulos for use of data from the THEMIS Mission (specifically: Martin Connors and C.T. Russell and the rest of the AUTUMN/AUTUMNX team for use of the GMAG data, S. Mende and C. T. Russell for use of the GMAG data and NSF for support through grant AGS-1004814.; S. Mende and E. Donovan for use of the ASI data, the CSA for logistical support in fielding and data retrieval from the GBO stations, and NSF for support of GIMNAST through grant AGS-1004736). In Chapter 4, the work of my co-author Dr. Yukitoshi Nishimura at Boston University was supported by NASA grant 80NSSC18K0657, 80NSSC21K1321 and 80NSSC22K0323, NSF grant AGS-1907698 and AGS-2100975, and AFOSR grant FA9559-16-1-0364. In Chapters 2, 3 and 4, the work of my co-authors Dr. Mark Engebretson and Dr. Erik Steinmetz was supported by NSF AGS-2013433.

TABLE OF CONTENTS

LIST OF FIGURES

FIGURE

LIST OF TABLES

TABLE

LIST OF APPENDICES

LIST OF ACRONYMS

AE Auroral Electrojet

AFRL Air Force Research Laboratory

AGU American Geophysical Union

AUTUMNX Athabasca University THEMIS UCLA Magnetometer Network eXtension

BBF Bursty Bulk Flow

CANMOS CANadian Magnetic Observatory System

CARISMA Canadian Array for Realtime InvestigationS of Magnetic Activity

CGM Corrected Geomagnetic

CGSM Canadian Geospace Monitoring Program

CME Coronal Mass Ejection

CNN Convolutional Neural Network

Dst Disturbance Storm-Time

EEJ Eastward Electrojet

FAC Field-Aligned Current

FN False Negative

FP False Positive

GIC Geomagnetically Induced Current

GBO Ground-Based Observatory

GMD Geomagnetic Disturbance

GMAG Ground Magnetometer

GPC Gaussian Process Classifier

GRL Geophysical Research Letters

HSS Heidke Skill Score

IGRF International Geomagnetic Reference Field

IMF Interplanetary Magnetic Field

IoU Intersection-over-Union

JGR Journal of Geophysical Research Letters

MACCS Magnetometer Array for Cusp and Cleft Studies

MHD Magnetohydrodynamic

M-I Magnetosphere-Ionosphere

MLT Magnetic Local Time

MPE Magnetic Perturbation Event

NASA National Aeronautics and Space Administration

NSF National Science Foundation

OB Oblique

POD Probaility-of-Detection

PBI Poleward Boundary Intensification

Pc Pulsation Continuous

Pi Pulsation Irregular

RBF Radial Basis Function

SC Sudden Commencement

SCW Substorm Current Wedge

SECS Spherical Elementary Current Systems

SI Sudden Impulse

SMR SuperMAG Ring-Current

SME SuperMAG Electrojet

SVM Support Vector Machine

THEMIS Time History of Events and Macroscale Interactions During Substorms

TLA Transient-Large-Amplitude

TCV Traveling Convection Vortices

TH Tyler Hussey

TN True Negative

TP True Positive

UCLA University of California, Los Angeles

ULF Ultra-Low Frequency

VI Vertical Incidence

WDC World Data Center

WEJ Westward Electrojet

ABSTRACT

This dissertation presents a comprehensive analysis of high-frequency transient-large-amplitude (TLA) geomagnetic perturbations in ground magnetometer data. TLA events are large ($\geq$ 6 nT/s), rapid ($<$ 60 seconds) magnetic field changes, or dB/dt. This dissertation characterizes TLA signatures and investigates their relation to other space weather events in order to gain insight into the small-scale magnetosphere-ionosphere processes that cause them and may also give rise to GIC.

In the initial discovery study, TLA events at five stations of the Magnetometer Array for Cusp and Cleft Studies (MACCS) throughout 2015 were identified. The events were characterized based on amplitude and frequency of occurrence, diurnal trend, and relation to geomagnetic storms, auroral substorms and nighttime geomagnetic disturbance events (GMD), also referred to as nighttime magnetic perturbation events (MPE). We show that TLA events occurred most often at local magnetic nighttime and while TLA events were observed at all five MACCS stations, a majority of individual events (74%) were observed at only one station, inferring a localized spatial scale smaller than $\sim$ 580 km. The main driver for TLA events in 2015 was not sudden commencements (SC) or sudden impulses (SI) that are the most rapid global-scale space weather events. Rather, TLA events showed stronger association to smaller-scale processes like substorms and nighttime GMDs.

The timescales and amplitudes of TLA dB/dt intervals are similar to noisy magnetic signatures caused by external interferences or internal instrumental defects, making detection of only TLA events a tedious and time-consuming manual process. An automated high-frequency magnetic disturbance classifier was developed to identify second-timescale, high-frequency dB/dt intervals in ground magnetic field data and discriminate between noise-type or geophysical TLA events. The full process utilizes insights gained from a statistical analysis of both types of events to implement constraints as well as a machine learning support vector machine to make the final classification of TLA or noise-type dB/dt. This method is a useful capability both for data quality control and the continued investigation of small-scale surface geomagnetic perturbations.

Finally, the automated high-frequency disturbance classifier was used to gather a large database of TLA events for all latitude ranges and throughout Solar Cycle 24 from 2009 to 2019. Characteristics of the expanded TLA database show results consistent with the initial study and with nighttime GMDs. TLA event occurrence peaked in the declining phase of the solar cycle and

trended similarly with the number of substorm onsets per day. Nearly all of the most extreme GMD events had associated TLA intervals in the same location and while GMDs have an effective radius of $\sim$275 km, TLA events exhibited even more localized spatial scale. From an analysis of a TLA-related GMD event, we show that these events are associated with dipolarization fronts on the nightside at geosynchronous orbit and fast plasma flows toward Earth, and are closely temporally related to poleward boundary intensifications (PBI) and auroral streamers in the ionosphere. The highly localized behavior and connection to the most extreme GMD events suggests that TLA intervals are a ground manifestation of rapid and complex ionospheric current structures coupled to the magnetosphere that can drive GICs. The analysis of high-frequency TLA geomagnetic perturbation events in this dissertation gives new perspective of small-scale magnetosphere-ionosphere (M-I) phenomena that can lead to GIC.

CHAPTER 1

Introduction

1.1 Space Weather Impacts

Space weather events occur due to the interaction of highly active solar wind with the Earth's magnetosphere, causing electromagnetic and magnetohydrodynamic disturbances to propagate throughout the magnetosphere-ionosphere (M-I) system. These events have impacts that can directly effect society on Earth.

The geomagnetic storm is the largest and longest type of space weather event. The largest geomagnetic storms are triggered by an interplanetary shock incident on the magnetopause that compresses the dayside magnetosphere. The interplanetary shock can be due to high speed solar wind streams or a coronal mass ejection (CME). The sudden compression increases the magnetopause current (shown in Figure 1.1) and pushes it closer to Earth, causing the worldwide average horizontal magnetic field on the ground in the equatorial region (called the Dst index) to rapidly increase. The compression is called a sudden commencement (SC) when it is followed by extended periods (several hours) of southward interplanetary magnetic field (IMF) causing geomagnetic storm phases to develop (it is termed a sudden impulse (SI) when storm phases do not follow it). The period of southward IMF and subsequent ring current enhancement characterizes the main phase of the storm: increased dayside magnetic reconnection causes more solar wind energy transport into the magnetosphere, enhancing the cross-tail current and ultimately increasing particle injection into the ring current. The ring current expands Earthward and continues a chain reaction of M-I disturbances down to Earth's surface. The recovery phase occurs when the southward IMF weakens or disappears completely, the reconnection rate decreases and the ring current decays. Thus the large-scale perturbations of the storm subside.

The auroral substorm is the most frequent type of geomagnetic activity, occurring 4-6 times per day (Borovsky and Yakymenko, 2017). Substorms happen concurrently with geomagnetic storms when the M-I system is highly disturbed, but occur in the absence of storm activity as well. Similarly to storms, substorms occur when the IMF turns southward and increased energy from the solar

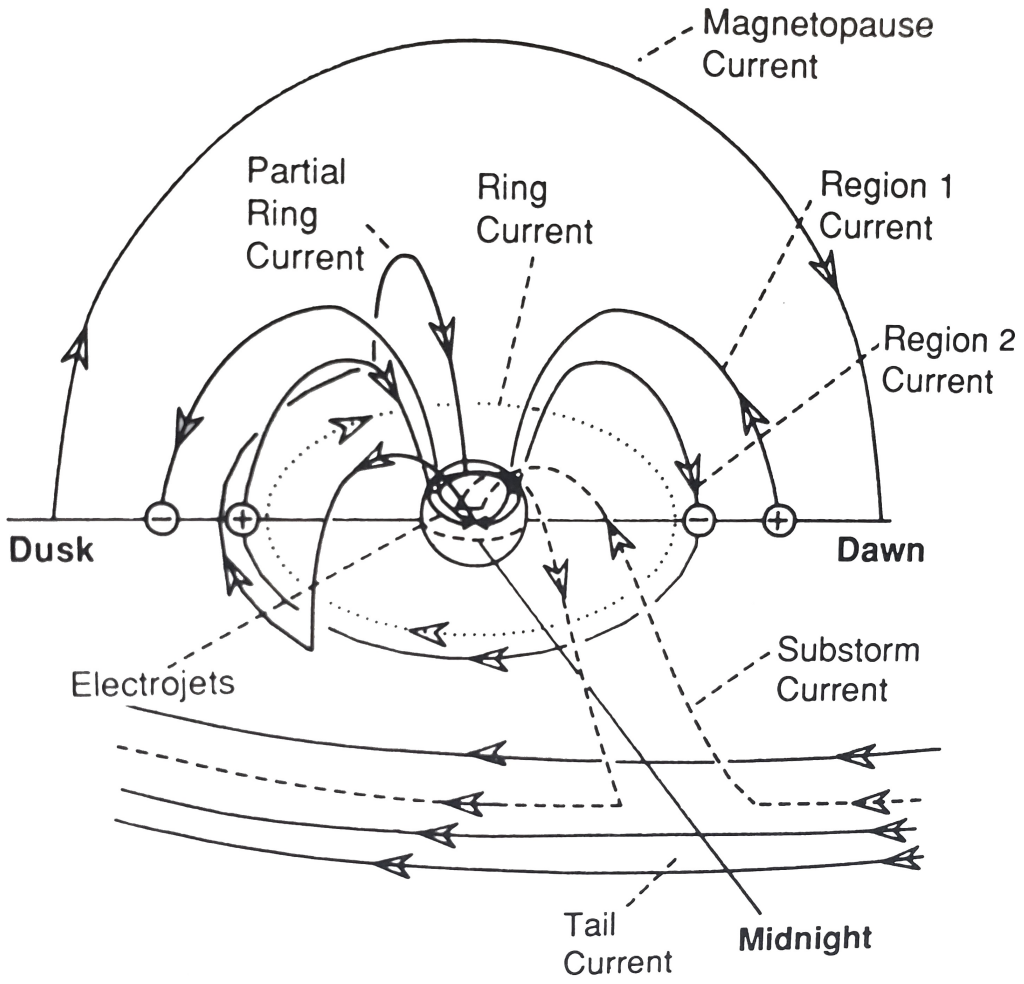

Figure 1.1: Diagram of some of the primary M-I currents involved in geomagnetic storms and substorms. The orientation of this figure is from the nightside of the Earth looking toward the dayside i.e., sunward. Image from Kivelson and Russel (1995).

wind flows into the magnetosphere, however the physical processes and primary current systems differ. As dayside reconnection occurs, magnetic flux is transferred from the solar wind and stored in the magnetotail, increasing pressure in the tail lobes resulting in thinning of the plasma sheet and formation of a neutral point in the near-tail; this is the growth phase. The expansion phase occurs when nightside reconnection occurs and the stored energy in the magnetotail is explosively released along field lines into the ionosphere (McPherron et al., 1973; Russell and Mcpherron, 1973; McPherron, 1979). The expansion phase forms a new current system: the substorm current wedge (SCW, Figure 1.1). The SCW diverts current from the tail in the Region 1 field-aligned current (FAC) orientation and closes via a westward auroral electrojet in the ionosphere. The auroral electrojet (AE) index is an effective measure of electrojet activity and is derived from the difference of the maximum and minimum horizontal magnetic field values recorded in the auroral

zone (approx. 60-75° geomagnetic latitude (MLAT)).

Figure 1.2 shows the orientation of the field-aligned current (FAC) systems from Le et al. (2010). The FACs extend from the outer magnetosphere down to the ionosphere where they close parallel to the surface via Pedersen currents. The upward and downward FAC generate rotational current systems called Hall currents that are also oriented parallel to the surface. These current systems are always present, but become enhanced during intervals of geomagnetic storm and/or substorm activity. Intensifications of the Hall currents during storms and/or substorms are referred to as the westward electrojet (WEJ) and eastward electrojet (EEJ). The FAC system is a highly effective vehicle for energy transport from the magnetosphere to the ionosphere and the surface of Earth.

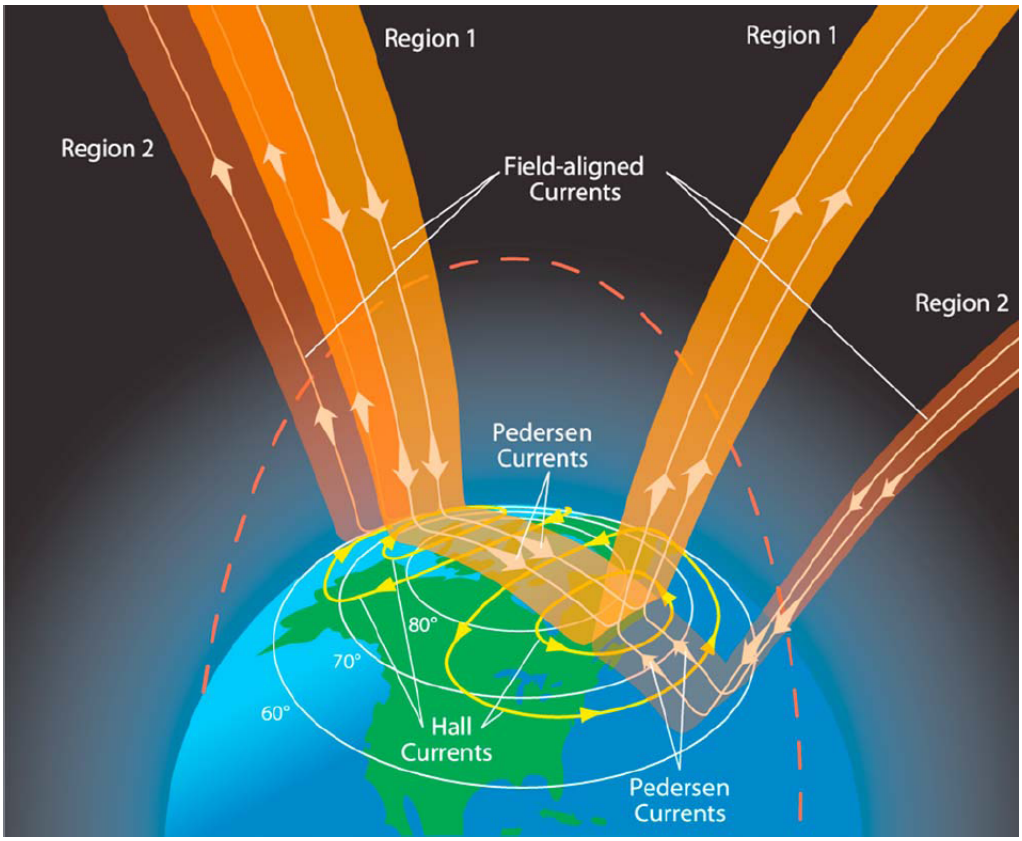

Figure 1.2: Diagram of field-aligned currents showing their closure in the ionosphere via Pedersen currents and subsequent Hall currents.

Enhancements and spatial redistribution of these current systems cause disturbances of the surface geomagnetic field. This effect is described by Faraday's law of induction: temporally varying magnetic fields always accompany spatially varying electric fields. From this physical principle, large variations of the surface geomagnetic field over time drive currents through conductive systems on Earth. These are referred to as geomagnetically induced currents (GIC).

GICs flow through long, parallel (to Earth's surface) systems like railways, pipelines and power grids (Boteler and Beek, 1999). Following an extreme space weather event, GICs can be large enough to cause severe damage to and even total failure of power systems resulting in major power outages and costly repairs.

The largest geomagnetic storm on record occurred in 1859 and is called the Carrington Event. The storm was so intense that the auroral oval expanded as far south as Hawai'i and large GICs flowed through and caused damage to telegraph transmission lines (Boteler, 2006). In more recent history, the geomagnetic storm of March 1989 caused GICs in the HydroQuebec power grid that caused a major power outage lasting nine hours. The 1989 storm was triggered by two large CMEs, the timing of the second CME interacting with Earth corresponded with the collapse of the HydroQuebec power system, and occurred prior to the peak intensity of the storm. When the storm reached maximum strength, the auroral oval expanded to lower latitudes and caused more localized power system issues at locations in the United States (Boteler, 2019).

1.1.1 dB/dt as a proxy for GIC

Following from Faraday's law of induction that describes electromagnetic induction via an electromotive force produced when an electric circuit interacts with a magnetic field, the Maxwell-Faraday equation relates the rate-of-change of the surface geomagnetic field, dB/dt, to the curl of the electric field (i.e., magnetically induced current). Equation 1.1 governs this relationship; this shows that the rotational electric field (i.e., current) is directly proportional to the temporally varying magnetic field.

$$\nabla \times E = -\frac{\partial B}{\partial t} \tag{1.1}$$

As such, dB/dt is often used as a proxy for GICs (Viljanen, 1998). More specifically, the approximate linear relationship between the horizontal component of the surface magnetic field, dH/dt, and the induced geoelectric field was by shown by Bolduc et al. (1998). Because of the directly proportional relationship between GIC and dB/dt, and because dB/dt measurements are more accessible than measuring the actual induced currents or geoelectric field within power lines, large surface dB/dt are studied to gain insight on the spatial and temporal behavior of space weather events that give rise to GICs. It is important to note that effective GICs in power systems are not solely dependent on the strength and direction of dB/dt, but also the spectral characteristics of the electromagnetic perturbations, the ground conductivity structure of the region and the geometry of the power system (Pulkkinen et al., 2017). The ground conductivity and power system geometry are issues pertaining to the engineering aspects of GICs, this dissertation research is focused on the spatio-temporal characteristics of dB/dt.

The amplitude and timescale of potentially hazardous dB/dt can be characterized by the associated M-I current activity that causes the disturbances on the ground. Kataoka and Ngwira (2016) organized dB/dt and the resulting GIC into three general categories: 1) RC-type: slow dB/dt with 10-60 minute timescale and amplitudes of hundreds of nT, associated with ring-current evolution that causes global GICs most effectively at low magnetic latitudes, 2) AE-type: fast dB/dt with timescale of several minutes and thousands of nT amplitude caused by auroral electrojet activity giving rise to GICs in high magnetic latitude regions, and 3) SC-type: global, transient dB/dt with timescale of several seconds and amplitudes of tens of nT, caused by sudden commencements. The RC- and AE- types are mainly dependent on the southward component of the interplanetary magnetic field and the solar wind speed, whereas the SC-type is mostly dependent on the dynamic pressure of the solar wind. Prior to the research presented in this dissertation, large, second-timescale dB/dt have been thought to be primarily related to SCs, as they are the most rapid space weather event. However, our research shows that second-timescale dB/dt with very large amplitudes are much more common than SCs alone, and often occur related to smaller-scale space weather events.

Because of the potential severity of space weather impacts on society and technological infrastructure, the more accessible and directly proportional value of GICs- dB/dt- is studied heavily in an effort to understand the behavior of both the M-I dynamics that give rise to the dB/dt and the engineering aspects of how large dB/dt generates GICs and how these GICs affect power systems. An ultimate goal is the ability to forecast severe space weather occurrences and predict the behavior of the magnetic field perturbations that will result.

1.2 Small-Scale Phenomena Related to GIC

The most extreme space weather events are geomagnetic storms that are triggered by the collision of a coronal mass ejection (CME) with Earth's magnetosphere (Gosling, 1993). Severe storms like the Carrington Event or the March 1989 storm are those that have been shown to generate the most damaging GICs on the largest scale. Thus, studies of GICs are often focused on analyzing the largest, longest geomagnetic storms (and subsequently the largest and longest dB/dt at the surface). However, beyond the largest events that cause disturbances of global-scale M-I currents, smaller-scale processes (often related to auroral substorms) that enhance finer-scale structures in ionospheric currents also play a key role in generating GIC.

It is often assumed that the geoelectric field impinging on a power system is spatially uniform across the scale-size of the system. However, a study by Pulkkinen et al. (2015) found that while large-scale geoelectric fields enhancements occur (generated by ionospheric currents and subsequent geomagnetic field disturbances), extreme peaks of the geoelectric field are much more localized. They show that single station peaks are often twice as large as the regional average ("regional

average" here refers to distances of the order of 500 km). Engebretson et al. (2019a,b) confirmed this by showing that nighttime geomagnetic disturbances (GMD) with 5-10 minute timescale are highly localized, with half-amplitude radius of ∼275 km. The structure of the geoelectric field in the localized regions where maxima occur can also greatly vary from regional and global extremes and these peaks often occur on short periods, so the geoelectric field can be temporally localized as well.

The nature of localized enhancements observed on the ground points to localized sources in the ionosphere (Boteler and Beek, 1999). Ngwira et al. (2015) expanded on the study by Pulkkinen et al. (2015) and provides further evidence for localized geoelectric field extremes. Possible source mechanisms suggested for the localized geoelectric field peaks are localized substorms, rapid intensifications of the Eastward Electrojet (EEJ) and bursty bulk flows (BBF) in the magnetotail.

BBFs are characterized by ∼10-minute timescale Earthward plasma flow velocity enhancements in the magnetotail corresponding with magnetic field dipolarizations and ion temperature increases (Angelopoulos et al., 1992). BBFs can produce north-south (N-S) aligned auroral streamers in the ionosphere (Henderson et al., 1998) that can then evolve into omega bands (Henderson et al., 2002). It is important to note that omega bands are related to fast Earthward flows (Partamies et al., 2017), but they can also be caused by Kelvin-Helmholtz instability driven by flow shears in the inner-plasma sheet (Liu et al., 2018b).

Ngwira et al. (2018) and Dimmock et al. (2020) further reinforce the regional variability of dB/dt and subsequent geoelectric field extremes. Dimmock et al. (2020) shows that regional variation of dB/dt is coupled to energy deposition in the magnetosphere and the results of Ngwira et al. (2018) agree that the localization of surface dB/dt is likely related to magnetospheric currents mapping to local ionospheric structures. Dimmock et al. (2020) suggests that GICs are primarily driven by small-scale spatiotemporal structures superimposed on the large-scale westward electrojet. The findings of Weygand et al. (2021) are consistent with this concept, showing that most localized nighttime GMDs capable of causing GICs occur underneath the WEJ and many under the Harang current system.

As previously mentioned in Chapter 1.1.1., the spectral characteristics of the geomagnetic perturbations are an important aspect of the resultant GICs. Shorter and higher-frequency perturbations in the Pi 1-2 range (16.7-1000 mHz) are not capable of directly causing large GICs due to the skin-depth effect of conductive media. These frequencies can only penetrate the lithosphere to shallow depths, resulting in smaller current induction loops that are not substantial within large-scale conductor systems like a power grid. However, large-amplitude, second-timescale geomagnetic perturbations often occur within longer space weather events that can generate substantial GICs in Earth's surface. Further, dB/dt in this frequency range may cause GIC that could impact small-scale conductors like free-floating electronics and sensors that are more sensitive to smaller

induced currents.

This dissertation is focused on the analysis of these rapid geomagnetic perturbations, referred to as transient-large-amplitude (TLA) perturbations. Nighttime GMDs are of particular interest in regard to TLA dB/dt because many GMDs have TLA dB/dt occurring prior to or within the overall disturbance. Investigation of the relationship between GMDs and TLA dB/dt is a central aspect of this dissertation.

An example of a TLA event is shown in the bottom panel of Figure 1.3, showing magnetic field data for ∼45 minutes at the RANK station on 17 December, 2017. The specific TLA dB/dt intervals are marked near 06:10 UT with the open circles (start of the interval) and closed circles (end of the interval) in each component. This TLA event occurred within an overall nighttime GMD event that began around 06:05 UT and peaked at about 06:15 UT.

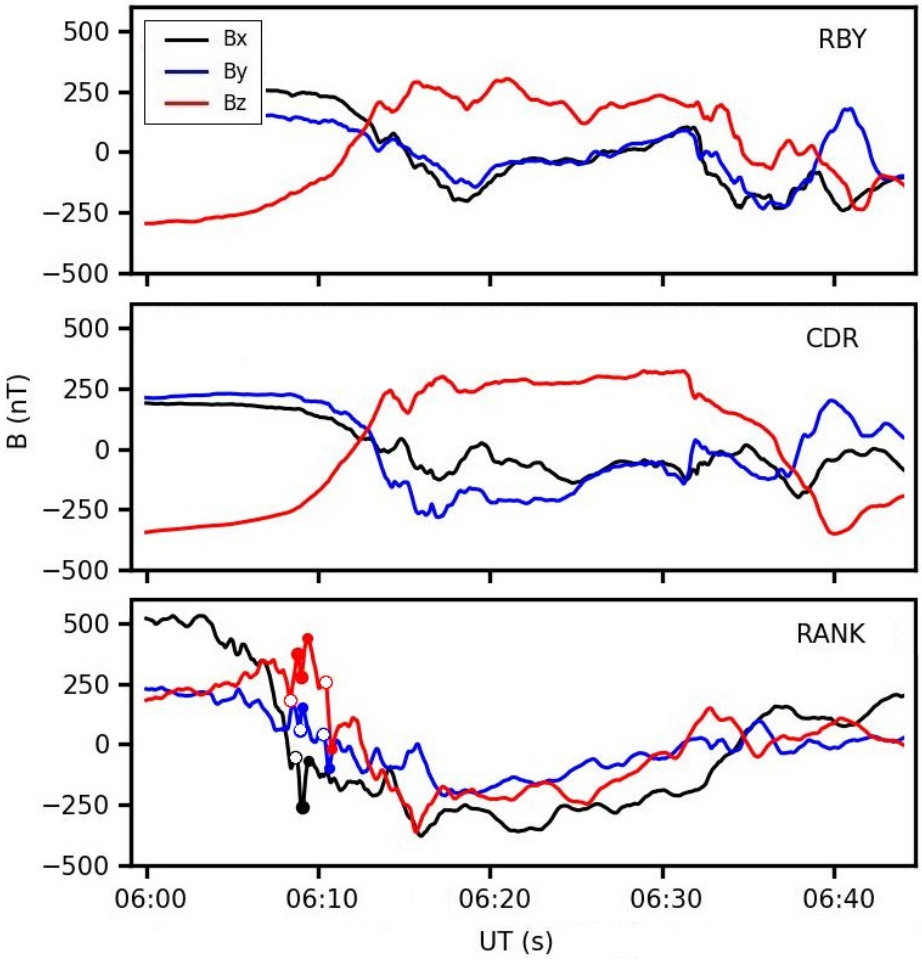

Figure 1.3: Magnetic field data from three stations on December 17, 2017. The Bx component is displayed in black, By in blue and Bz in red. The TLA intervals are signified by hollow circles denoting the start of the interval and filled circles denoting the end of the interval. The mean B value in the each component has been subtracted.

The other station data are shown in the panels above RANK in Figure 1.3 because they show nighttime GMD events from about 06:10 to 06:20 UT as well as 06:30 to 06:40 UT (Engebretson, 2023). The GMDs at RBY and CDR both have maximum derivative amplitudes exceeding 10 nT/s. The RANK station measured TLA dB/dt that also exceeded 10 nT/s, and the overall magnetic field change during the entire interval was also largest at RANK, with ΔBz of nearly 800 nT from 06:09 to 06:15.

The dB/dt values for every half-second measurement over the same interval shown in Figure 1.3 are displayed in Figure 1.4. The scale of the y-axes are the same for all three panels; while there are dB/dt peaks at RBY and CDR when the nighttime GMDs are occurring, the dB/dt values at RANK when the TLA event occurred were the largest of the three stations. Figures 1.3 and 1.4 show examples of a scenario in which nighttime GMDs occurred at three stations with TLA dB/dt occurring within the largest GMD at only one of the three locations.

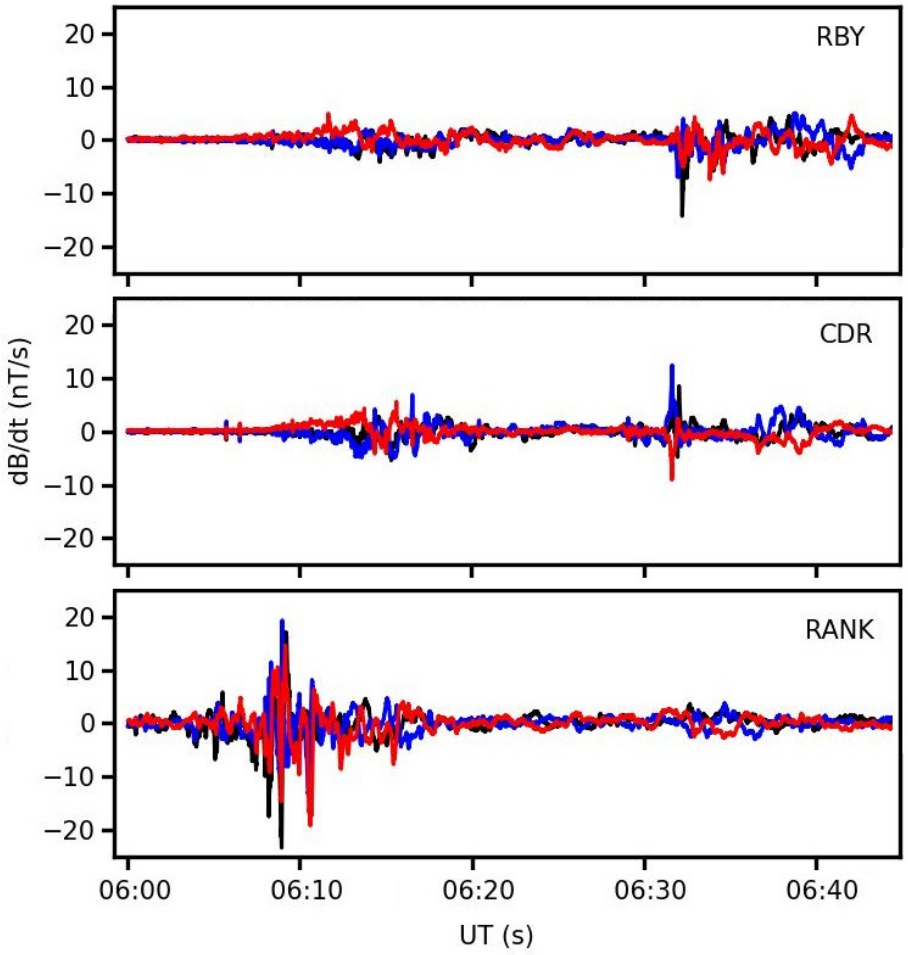

Figure 1.4: Magnetic field dB/dt data for three stations on December 17, 2017. The dBx/dt values are displayed in black, dBy/dt in blue and dBz/dt in red.

1.3 ULF Wave Context

Low-frequency waves in plasma are such that the frequency of the wave perturbations are lower than the natural frequencies of the plasma (i.e., plasma frequency, ion gyrofrequency). Because plasma is composed of charged particles, both mechanical properties (i.e., pressure, density) and electromagnetic properties (i.e., electric currents, magnetic field) effect the ionized gas; the result is magnetohydrodynamic (MHD) waves.

MHD waves are described by three solutions to the basic set of MHD equations consisting of fluid equations, Maxwell's equations and Ohm's law (McPherron, 2005). These solutions define three characteristic MHD wave modes: the (1) fast and (2) slow modes are compressional waves with speeds relative to the (3) Alfvén wave speed. The Alfvén wave is a non-compressional (constant pressure and density) wave that propagates parallel to the magnetic field lines. The Alfvén wave behaves like beads (particles) on a string (magnetic field line) and thus effectively channels energy along field lines through different regions of the M-I system. Alfvén waves play an important role in M-I coupling as they carry FACs (Keiling, 2009) and are essential in establishing quasi-static FAC as shown in Figure 1.2.

Ultra-low frequency (ULF) waves in the magnetosphere are magnetohydrodynamic plasma waves in the frequency range from about 1 mHz to 10 Hz. ULF waves in the magnetosphere are classified by their waveform and wave period (Jacobs et al., 1994) The two waveform classifications are pulsation continuous (Pc) for quasi-sinusoidal waveforms and pulsation irregular (Pi) for irregular waveforms; these waveforms are then divided into subclasses based on wave period as shown in Figure 1.5.

ULF waves have multiple generation mechanisms including sources in the solar wind, magnetopause instabilities and interactions within the magnetosphere (e.g., Engebretson et al., 1987; Walker, 1981). These waves play a key role in transporting energy throughout the M-I system. The wave frequency and polarization is dependent on the source of energization and subsequently the region where energization occurs. When measured on the ground, the ULF wave frequency depends on where the local field line maps to in the magnetosphere, and the locations of magnetospheric regions is variable depending solar wind dynamic pressure and magnetic field conditions.

Pc-1 and Pc-2 frequencies measured on the ground are caused by electromagnetic ion-cyclotron (EMIC) resonances generated in the equatorial region of the magnetosphere (Roldugin et al., 2013) and are associated with the recovery phase of geomagnetic storms and auroral particle precipitation (Engebretson et al., 2008). Not shown in Figure 1.5, Ps6/Pi3 magnetic pulsations are quasi-periodic sequences of GMDs with $\sim$5-40 minute periods and they often accompany omega band auroral structures (Opgenoorth et al., 1983).

Pi 1-2 have long been understood to be substorm-related and well-correlated with bright, ac-

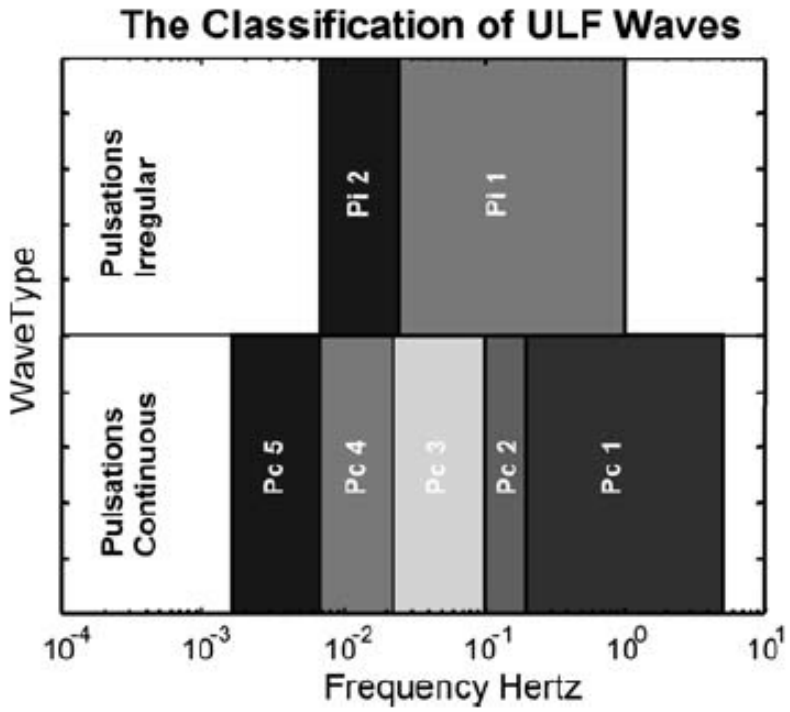

Irregular Pulsations

Class	Low edge Period (s)	High edge Period (s)
Pi 2	150	45
Pi 1	45	1

Continuous Pulsations

Class	Low edge Period (s)	High edge Period (s)
Pc 5	600	150
Pc 4	150	45
Pc 3	45	10
Pc 2	10	5
Pc 1	5	0.2

Figure 1.5: ULF waveform classifications in frequency range (left) and period range (right). Adapted from Jacobs et al. (1994).

tive aurora (Rooney and Sherman, 1934). Pi pulsations are currently understood to originate from cross-tail current disruption triggering Alfvén waves carrying FACs that establish the substorm current wedge (Milling et al., 2008; Baumjohann and Glassmeier, 1984), resulting in particle precipitation into the local E-region ionosphere (Engebretson et al., 1983; Oguti et al., 1984). Further, Pi2 pulsations have been linked to BBFs in the near-Earth magnetotail (Kepko and Kivelson, 1999).

The TLA dB/dt intervals that are the focus of this dissertation are geomagnetic perturbations in the Pi 1 and short Pi 2 frequency ranges. TLA dB/dt are referred to as high-frequency disturbances because they fall in the highest range of the ULF wave frequency band, but they are not necessarily sinusoidal, more often these perturbations have irregular waveform like Pi pulsations. TLA dB/dt show similarities to Pi pulsations in timescale and frequency, as well as some space weather drivers but they are not defined as Pi 1-2 pulsations because they do not always show a direct association to substorm onsets.

1.4 Machine Learning Applications to Space Weather

Second-timescale dB/dt are often excluded from space weather studies because these higher frequencies of the magnetic field are effectively low-pass filtered when computing the resultant geo-

electric field (Pulkkinen et al., 2006, 2013). Thus, 1-minute resolution magnetic field data have long been the accepted standard for space weather research. However, there has been a more recent demand for higher temporal resolution magnetic field data in GIC research in order to increase accuracy and reduce bias in GIC forecasting (Gannon et al., 2017; Grawe et al., 2018).

The challenge that arises with the use of high-rate ($\leq$ 10 s) magnetic field measurements is that noisy signatures are present. Data measured at or averaged over 1-minute helps to exclude or remove instrumental artifacts and/or noisy data due to interference. Using high-rate magnetic field data requires an alternative method to reduce contaminated data. Many current automated data-cleaning processes may remove some noisy dB/dt intervals but do not remove them all, and can also remove important geophysical TLA dB/dt that are very similar in timescale and amplitude to variations caused by magnetic noise sources.

Machine learning is the field of data science that uses algorithms to build models that "learn" the behavior of some set of training data, then makes predictions, detections or classifications of new, unseen data based on the learned behavior and improves performance with increased experience in such decision-making (Mitchell, 1997). Machine learning was developed in the late 1950's and has grown in popularity since, evolving with new models and new applications to problem solving in various fields.

In recent years, machine learning applications to space weather problems have grown significantly (Goss, 2020). Numerous machine learning models have been used to predict magnetic field values for forecasting purposes, such as feed-forward and convolutional neural networks (Reiss et al., 2021) as well as linear, random forest and gradient boosting regressors (Pinto et al., 2022). Further, machine learning techniques have been employed for the specific task of magnetic field data cleaning as well. Finley et al. (2023) used a convolutional neural network to identify and remove noisy magnetometer data from interference by other components aboard a spacecraft. Hoffmann and Moldwin (2022) used an unsupervised machine learning clustering algorithm to separate the ambient magnetic field from spacecraft noise.

In this dissertation, we present a new technique to identify large, second-timescale magnetic field disturbances and classify them as either noise-type or geophysical. As the use of magnetic field data with high temporal resolution becomes more imperative in space weather research, the technique allows for the use of such high-rate data without averaging the data or using other automated data cleaning methods that can remove meaningful geophysical signatures.

1.5 Guiding Questions

This thesis is focused on analyzed high-frequency, TLA dB/dt in surface magnetic field data. The following list compiles the central guiding questions for this dissertation research.

1. **How often do TLA signatures occur? What are their amplitude characteristics and spatiotemporal behavior?** How do TLA events present on large spatiotemporal scales i.e., throughout a solar cycle and at all magnetic latitudes?

2. **How can TLA dB/dt be effectively identified in high-rate magnetic field data to enable continued analysis without a time-consuming manual identification process?** Are there distinctions between the characteristics of magnetic noise and high-frequency geophysical dB/dt and how can these be exploited to make TLA identification more efficient? How can machine learning be applied to the problem of detecting TLA intervals in magnetic field data and what implications might this have for the space weather community as a whole?

3. **Are TLA signatures significant in the context of space weather events that can cause GICs?** What is the relationship of TLA intervals with larger space weather events and what can be learned about small-scale M-I dynamics from this relationship?

1.6 Outline

This dissertation is organized as follows. Chapter 2 addresses the first guiding question. This chapter presents an initial discovery study of TLA dB/dt intervals in magnetic field data and asserts their importance in the investigation of GICs. This analysis includes one year of magnetic field data from several magnetometer stations in north-east Canada; we investigate their behavior throughout daily magnetic local time as well as the entire year, discuss the localization of events within the region and contextualize them in relation to geomagnetic storms, substorms and nighttime GMDs. Chapter 3 answers the second guiding question and presents a new technique to identify high-frequency dB/dt and classify intervals as either noise-type or geophysical. The performance of the method is analyzed and the implications of this method for scientific community are explored. Chapter 4 provides a more comprehensive analysis that addresses the first and third guiding question. This chapter presents a study of TLA dB/dt that occurred throughout Solar Cycle 24 at a large number of stations in the high-latitude region. The study provides more data to show the spatiotemporal behavior of TLA events and discusses their association to nighttime GMDs that can cause GICs. Then a case study of a TLA-related GMD event is presented that provides evidence for potential solar wind drivers and M-I processes responsible for these events. Chapter 5 presents our conclusions and their impacts, and discusses future work.

CHAPTER 2

Characterization of Transient-Large-Amplitude Geomagnetic Perturbation Events

This chapter presents an initial discovery study of TLA dB/dt measured on the ground in the context of GICs. This research was originally published in the American Geophysical Union's Geophysical Research Letters journal under the title "Characterization of Transient-Large-Amplitude Geomagnetic Perturbation Events. Geophysical Research Letters" (McCuen et al., 2021). The work is presented as published with minor formatting adjustments. The tables of TLA events and space weather association information, as well as the algorithm developed for this research are available on the University of Michigan Deep Blue data repository (https://doi.org/10.7302/9t46-0092). The results presented in this chapter rely on the SC Event List calculated and made available by Observatori de L'Ebre, Spain from data collected at magnetic observatories. The authors thank Mike Hapgood for his comments as a referee of this publication.

2.1 Introduction

Space weather events occur due to the interaction of active solar wind with near-Earth space, activating magnetohydrodynamic (MHD) and electromagnetic transfer processes that propagate throughout the magnetosphere-ionosphere (M-I) system down to the surface of Earth. Perhaps the most critical concern regarding space weather is the threat of large geomagnetically induced currents (GIC) to technological infrastructure on Earth. Flowing through man-made conductors on Earth like railways, pipelines and power grids, GICs can be large enough to cause damage to transformers resulting in major power outages and costly equipment damage (Boteler et al., 1998; Pulkkinen et al., 2017). GICs are the result of a horizontal surface electric field **E** induced in Earth's surface that is driven by large changes of the surface magnetic field, dB/dt, via Faraday's law of induction. Hazardous GICs associated with large, rapid magnetic disturbances often result from the most disruptive geomagnetic storms and auroral substorms. Therefore, significant efforts

of the geophysical community are aimed at developing global MHD models of geomagnetic storm and substorm activity and incorporating the magnetotelluric response of the Earth to compute GICs (Pulkkinen et al., 2015; Zhang et al., 2012). However, beyond the largest space weather events, several studies suggest that there are more rapid, small-scale and localized processes involved in generating some extreme GICs (Dimmock et al., 2020; Engebretson et al., 2019a, 2021; Ngwira et al., 2015, 2018; Opgenoorth et al., 2020).

Impulsive geomagnetic disturbances as a source of GICs were first reported by Kappenman (2005). More recently, Belakhovsky et al. (2019) presented case studies of impulsive magnetic events such as sudden commencements (SC), dayside traveling convection vortices (TCV), nightside geomagnetic disturbance events (GMD) (also known as nighttime magnetic perturbation events (MPE)), and irregular Pi3 pulsations that can all induce substantial GIC. These impulsive disturbances are in the lower range of the ultra-low frequency (ULF) band from 1-22 mHz with periods of 1-10 minutes. Shorter-timescale ($<$ 1 minute) perturbations of the geomagnetic field are much less effective at generating GICs due to their frequency content. Because of the skin depth effect in a conducting medium, lower frequencies penetrate deeper into the Earth, increasing the size of the induction loop and subsequent induced currents while higher frequencies can only penetrate to shallow depths, resulting in much smaller induction loops that are incapable of driving GICs (Oyedokun et al., 2020). While extreme dB/dts with second timescales do not cause GICs on Earth directly, we show here that they often occur in close relation to or within larger impulsive disturbances that *are* capable of generating GICs. These rapid magnetic perturbations in the Pi 1-2 frequency range may be ground manifestations of small-scale ionospheric current systems that play an important role in driving localized, but considerable GICs.

In this study, we present occurrences of transient-large-amplitude (TLA) dB/dts that occurred at one or more of six stations of the Magnetometer Array for Cusp and Cleft Studies (MACCS) throughout 2015. These perturbations all have amplitudes comparable to geomagnetic disturbances that cause large GICs, but have timescales less than 60 seconds. We investigate them here in an effort to gain insight on the transient structures of the geomagnetic field and small-scale M-I coupling mechanisms relevant to GICs. We have characterized these events based on their frequency of occurrence, spatial and temporal dependence, and association (or lack thereof) to longer impulsive magnetic events, substorms and storms.

2.2 Data Set and Identification Technique

The magnetometer data used in this study are from six ground stations of the MACCS array. The stations are located in north-east Nunavut, Canada (geographic and corrected geomagnetic (CGM) coordinates are listed in Supporting Information Table S1, the stations are shown with

lines of CGM latitude in the map of Supporting Information Figure A.1.) This chapter refers to station locations in CGM coordinates that were calculated for the year of 2015 with the IGRF transformation tool of the World Data Center (WDC) for Geomagnetism, Kyoto. The MACCS magnetometers collect 8 samples per second in three axes, then average and record the data at two samples per second (Hughes and Engebretson, 1997). The half-second sampling rate and high sensitivity (0.01 nT resolution) of the MACCS magnetometers is sufficient to detect shorter period Pi 1 and 2 pulsations. The geomagnetic variations measured by the magnetometers are in local geomagnetic coordinates: *X* (north-south), *Y* (east-west) and *Z* (vertical).

A semi-automated algorithm was developed to identify dB/dt signatures in magnetometer data with user-specified duration and magnitude. After initial data processing to remove instrument artifacts and smooth the data with a sliding average (if desired and with user-specified window length), the algorithm is essentially a series of filters. First the algorithm calculates the slope between each and every data point and determines the sign of the slope (assigns a 1 if positive slope, -1 if negative slope). If the sign of the slope changes for at least 1-second (two data points), the data point at which this change occurs (i.e., local minima or maxima) is flagged. Then the last filter recalculates the new dB/dt between each local maxima and minima and returns the information of the signature if it meets the conditions of the defined thresholds for dB/dt and Δt. The final product returned from the algorithm is a seven column matrix, each row represents an individual event and provides the start and end time of the event, start and end B value, the time elapsed of the event: *dt*, the change in magnetic field amplitude: *dB*, and the total derivative amplitude of the interval: dB/dt.

We used this algorithm to identify dB/dt signatures with amplitude 6 nT/s or higher and duration less than 60 seconds. The dB/dt threshold is comparable to the surface magnetic field perturbations ($\sim$8 nT/s) that caused the HydroQuebec power grid to fail during the geomagnetic storm of March 1989 (Kappenman, 2006). Further, the timescale threshold of $<$60 seconds makes these dB/dt intervals distinct from common GIC studies that focus on longer magnetic field changes $>$1 minute.

We characterize a transient-large-amplitude (TLA) event as one or more of these dB/dt signatures if they occur within 1-hour of another (regardless of the axis measured in and the station measured at). Note that in this chapter we refer to events as TLA dB/dt intervals grouped by hour *and* station (i.e., TLA events occurring at multiple stations within an hour is one event), in the rest of this dissertation TLA events are separated by station location (i.e., TLA dB/dt groups at multiple stations are counted as multiple events).

Because of the timescale and magnitude of the dB/dts sought, many of these signatures are similar in nature to magnetometer noise caused either by instrumental artifacts or magnetic deviation due to interference by ferromagnetic materials in the vicinity of the magnetometer (Nguyen et al., 2020). Therefore, each event returned from the routine was visually inspected to confirm that it

appeared to be of physical nature or remove it if it was a result of noise. The manual classifications of either geophysical TLA events or noise-type events were based on documented shapes and amplitudes of noise in fluxgate magnetometer data (Khomutov et al., 2017), and inspection of the behavior of the magnetic field on second-timescale. Noise-type events consistently showed very sharp variation of the magnetic field on a second-timescale while geophysical events exhibited smoothly varying magnetic field changes on second-timescale.

In our manual inspection process, we found that the events resulting from magnetometer noise have several characteristics that make them possible to automatically detect. Our future work will incorporate a machine learning noise identification method that will help to fully automate the dB/dt search algorithm and contribute to magnetic noise cleaning approaches for other magnetometer arrays.

After the filtering process, a total of 178 transient-large-amplitude dB/dt signatures were identified. The majority of these signatures (61%) were measured in the x-component (north-south), 30% in the y-component (east-west) and 9% in the z-component (vertical). Finally, grouping the dB/dts if they occurred within 1 hour of another signature resulted in a total of 38 TLA dB/dt events. While the primary temporal periods of interest in this study are 1-60 seconds, we also ran the algorithm with the upper limit for the duration of events extended to 5 minutes in order to compare to the 5-10 minute lasting GMDs studied in Engebretson et al. (2019a). Note that we used cleaned, full resolution half-second magnetic field data in this study and GIC measurement often involves averaging magnetometer data over 1 minute (Ngwira et al., 2008; Pulkkinen et al., 2006). Because our identification method relies on changes of the magnetic field lasting at least 1 second, some larger and more extended dB/dts are undetected by our algorithm due to more rapid changes of the slope within.

Our analysis of TLA event dependence on space weather events relies on several databases. The SuperMAG database (Gjerloev, 2012) Ring Current (SMR) index (Newell and Gjerloev, 2012) was used to determine geomagnetic storm activity and the SuperMAG Electrojet indices (SME) (Newell and Gjerloev, 2011) were used to examine auroral substorm activity during the events (supermag.jhuapl.edu/indices/). The association of TLA events with SCs was determined with the International Service of Geomagnetic Indices Sudden Commencement event list (isgi.unistra.fr/events_sc.php).

2.3 Occurrence of Transient-Large-Amplitude (TLA) dB/dt Events

We identified 38 TLA events consisting of one or more dB/dt signatures with magnitude 6 nT/s

or higher and duration less than 60 seconds. Over half of the events (55%) have multiple dB/dt signatures. Seven of the 38 TLA events exhibit dB/dts that last less than 10 seconds; in six of these cases the $<$ 10 s signatures precede a larger-amplitude, longer-timescale dB/dt. Figure 2.1 shows three panels with examples of distinct TLA events identified at the MACCS stations in 2015. The hollow circles in all three panels of Figure 2.1 mark the start of each dB/dt within the TLA event and the solid dots mark the end of each dB/dt. Note that axes in all plots of Figure 2.1 have been adjusted by subtracting the mean $B_{x,y,z}$ value from the interval, so the magnitude of the rate of change of the magnetic field is still to scale.

We expected to find many events occurring due to SCs or sudden impulses (SI, a dayside magnetospheric compression that is not followed by geomagnetic storm phases) as they have been considered the primary driver for the most rapid GICs (Kataoka and Ngwira, 2016). We found only one SC-related event, shown in Figure 2.1a. This is the only SC-related event despite five recorded SCs and two SIs that occurred in 2015 when the MACCS stations were located on the dayside. This TLA event started on 22 June 2015 at 18:33:22 UT (12:41:22 MLT, at RBY), just seconds after a large CME reached Earth causing an SC at 18:33 UT. The largest dB/dt signature of the entire data set occurred in this event at RBY in the y-component, lasting 9.5 seconds with a magnitude of -33.49 nT/s. The dB/dts measured in the y- and z-components at PGG and CDR all last 10.5 seconds or less, with the shortest event in the y-component at CDR with a magnitude of 13.3 nT/s and lasting just 5 seconds.

Shown in Figure 2.1b is an event that occurred on 11 November 2015 beginning at 01:12:20 UT (21:22:36 MLT of 10 November 2015). This event consists of 34 dB/dts measured at all but the NAN station. Of these 34 dB/dts, six have magnitude greater than 10 nT/s and five have duration $<$ 10 seconds. One of the largest dB/dts (16.2 nT/s) was measured at PGG at 1:13:21 UT in the y-component and lasted only 1 second. The TLA dB/dts occur at each station within a $\sim$6 minute interval and occur within a nighttime GMD event (Engebretson et al., 2019b). The TLA and GMD event occur within a longer period of disturbance that lasted $\sim$1 hour; they are not associated with a geomagnetic storm, although a substorm onset occurred at 01:07 UT, about 5 minutes prior to the start of the event. The events were preceded by a steady magnetic field for at least an hour prior to the start of the disturbance around 00:40 UT.

Finally, Figure 2.1c shows a TLA event on 9 October 2015 starting at 04:26:06 UT at the CDR station (23:31:06 MLT of 8 October 2015) where B_x decreases by 135.9 nT in 21 seconds (dB_x/dt = -6.46 nT/s). Then about 14 minutes later, two similar signatures occurred at GJO: a dB_x/dt of -6.87 nT/s at 04:49:37 UT and a dB_y/dt of -6.52 nT/s at 04:41:05 UT. Note, however, that the dB_x/dt at GJO actually lasted 80 seconds, this is one of the signatures identified when extending the upper threshold for the duration of the sample in the search algorithm to 5 minutes rather than 60 seconds. This TLA event occurred on the second day of recovery from a moderate geomagnetic

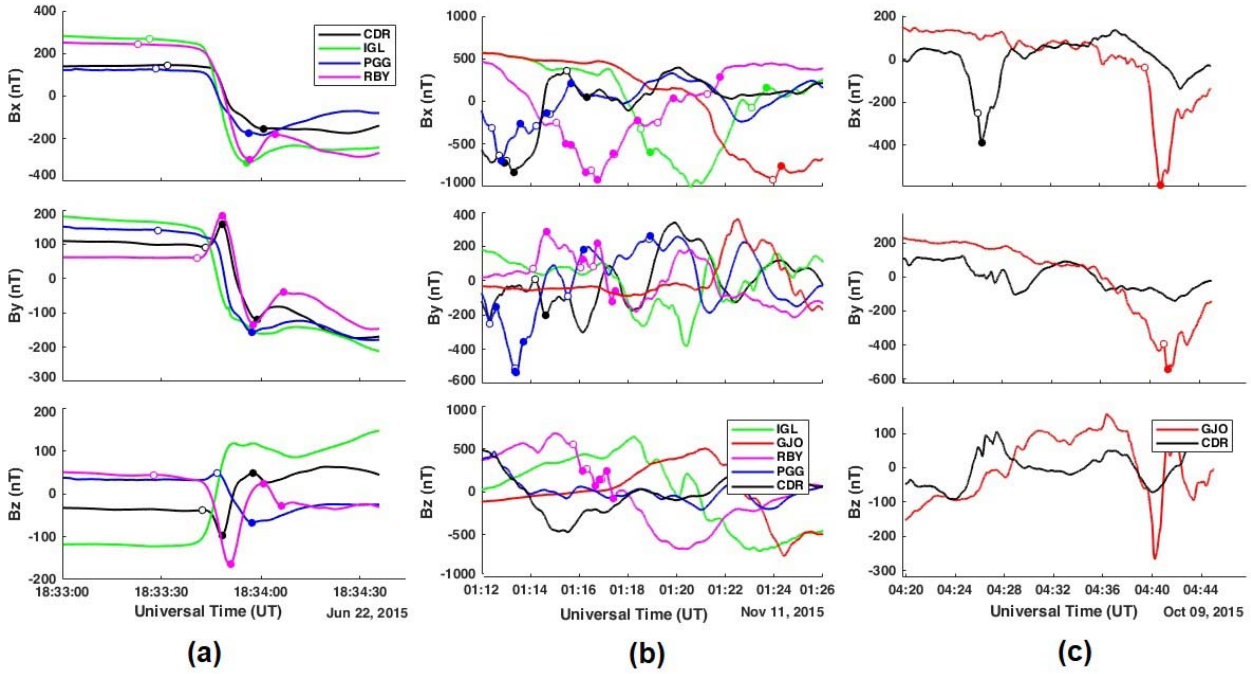

Figure 2.1: (a): A TLA event that occurred on 22 June 2015. (b): An event that occurred on 11 November 2015. (c) An event that occurred on 9 October 2015. All three panels show the x, y and z components of the surface magnetic field from top to bottom, respectively. Hollow circles mark the start of a dB/dt signature and solid dots mark the end.

storm and there were marked substorm onsets occurring at 04:13 UT and 4:34 UT. A nighttime GMD was identified at RBY at 04:37 UT in the interval between these two TLA events at CDR and GJO but no TLA signatures were measured within the GMD at RBY (note that the GJO station was not used in the statistical study of Engebretson et al. (2019a)).

2.4 Spatial and Temporal Characteristics and Space Weather Dependence

There are ten TLA events that consist of at least one dB/dt signature with magnitude exceeding 10 nT/s and half of these occurred within an event that has at least one other $|dB/dt| \geq 10$ nT/s. The ten largest events were measured primarily between 73° and 76° CGM latitude at the PGG and CDR stations: PGG and CDR not only recorded the majority of the largest events but a substantial fraction (52.6% and 44.7%, respectively) of events in general. The GJO (76.86°) station recorded eight events and RBY (75.62°) and IGL (78.63°) recorded four events each. The southern-most station, NAN (65.67°), recorded just two events that were not recorded at any other station. In fact, 74% of the events were measured locally at only one station (the average, absolute distance from

one station to the nearest station is ∼580 km. Note this average excludes NAN as it is the lowest latitude station with only two locally recorded events). Of the other 26% of events measured at more than one station, 4 were recorded relatively simultaneously (as shown in Figures 1a and 1b) while 6 other events had dB/dts at more than one station delayed by at least 2 minutes (and at most 14 minutes, shown in Figure 2.1c).

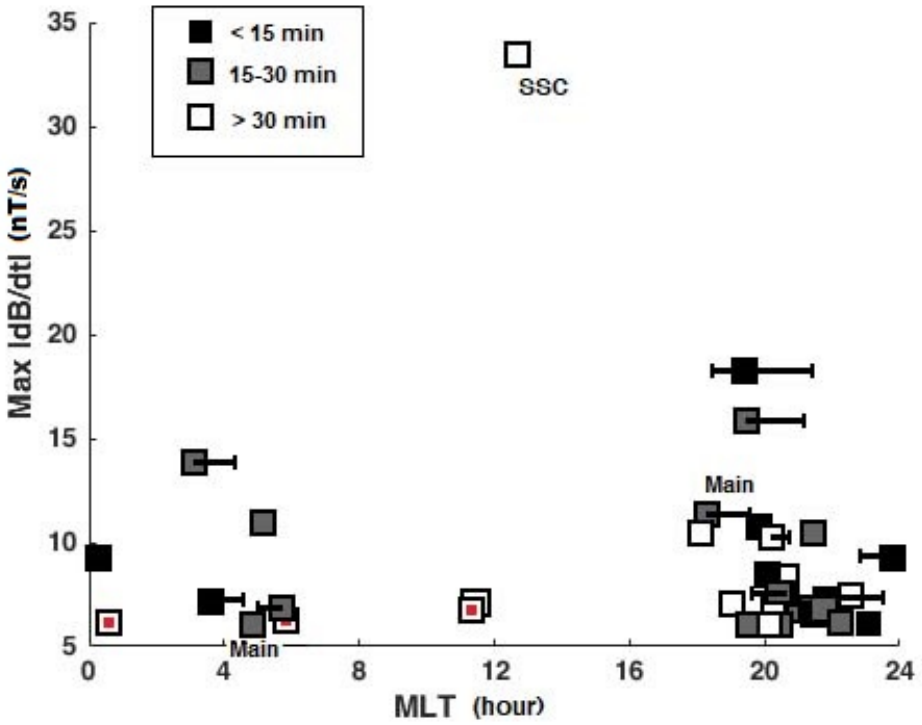

Figure 2.2: Maximum dB/dt as a function of magnetic local time (MLT) of each TLA event found in 2015. The bars extended from some squares signifies the duration of an event with multiple dB/dts. The opacity of squares is based on the temporal proximity after the nearest substorm onset. The inner red squares signify unrelated events that occurred more than 30 minutes from substorm onset and in the absence of a storm or nighttime GMD.

TLA events occurred substantially more often in the Fall-Winter months with 57.9% of events occurring in October through December. To illustrate the occurrence of TLA events as a function of magnetic local time as well as the association to geomagnetic storms and substorms, Figure 2.2 shows the maximum dB/dt of each TLA event throughout 2015 as a function of MLT. The events that occurred between 18-6 MLT are plotted as squares with opacity according to temporal proximity of prior substorm onset: the black squares signify that the event started within 15 minutes after the nearest substorm onset and during nighttime hours of 18-6 MLT, the grey squares are events that occurred 15-30 minutes after substorm onset and the white squares occurred more than 30 minutes after the nearest substorm onset (daytime events were automatically marked as

white squares). These onset delays were determined with the SuperMAG Newell and Gjerloev (2011) Substorm Event List (supermag.jhuapl.edu/substorms/). The bars extending from some of the squares in Figure 2.2 signify the full duration of the event if it consisted of multiple dB/dts, showing at what point throughout the event that the maximum dB/dt occurred. Only three events occurred in the commencement or main phase of a geomagnetic storm, these are labeled in Figure 2.2. There are also five events that occurred on the first day of recovery from a geomagnetic storm and four events that occurred on the second day of recovery.

Figure 2.2 shows that a vast majority (92.1%) of events occurred at nighttime between 18-6 MLT with peak number of events (71.1%) in the pre-midnight sector from 18-24 MLT. A large number of the events (73.7%) occurred within 30 minutes of substorm onset, but it is clear from Figure 2.2 that not all of the nighttime events show this association to substorm onsets (see white squares occurring at nighttime). While there is a strong association of TLA events to substorm onsets, 26.3% of events occurred more than 30 minutes after a substorm onset, with a small subset of events (10.5%) that occurred more than 2 hours after substorm onset. Figure 2.2 also shows that the ten largest TLA events ($\geq$ 10 nT/s) were more likely to occur between 18-24 MLT and within 30 minutes of a substorm onset, but they did not always occur within 30 minutes of substorm onset.

Comparison to the nighttime GMD events of Engebretson et al. (2019a) found that 73.7% of TLA events either preceded an GMD at one of the six stations within 30 minutes or occurred within the longer-timescale perturbation. Seven of the ten largest $>$ 10 nT/s TLA events were associated to GMDs that also exceeded $>$ 10 nT/s but on 5-10 minute timescales. The GMDs that have TLA dB/dts associated with them comprise less than 5% of the entire set of GMDs identified in 2015, however over half the GMDs that have TLA signatures are among the set of largest GMDs ($>$ 12 nT/s) identified at the MACCS stations during 2015.

Less than 10% of TLA events occurred in the absence of a geomagnetic storm and more than 30 minutes after the nearest substorm onset or nighttime GMD, we classify these as unrelated events (marked in Figure 2.2 as squares with red centers). While TLA events can occur during quieter geomagnetic conditions, there is a clear tendency for these signatures to appear during conjunctions of space weather events. The Venn diagram of Figure 2.3 shows the number of TLA events based on their association to other geomagnetic disturbances, showing the overlapping (and lack thereof) of events that can give rise to TLA dB/dts. It was previously noted that the percentage of TLA events related to substorms and nighttime GMDs is the same, but Figure 2.3 shows that these are not the same set of events. TLA events were most likely to occur in association with a nighttime GMD that commenced within 30 minutes of a substorm onset, however this was not *always* the case. The higher density to the right side of the diagram illustrates that TLA events generally did not occur due to a global geomagnetic event alone; more often there were other, smaller-scale processes involved.

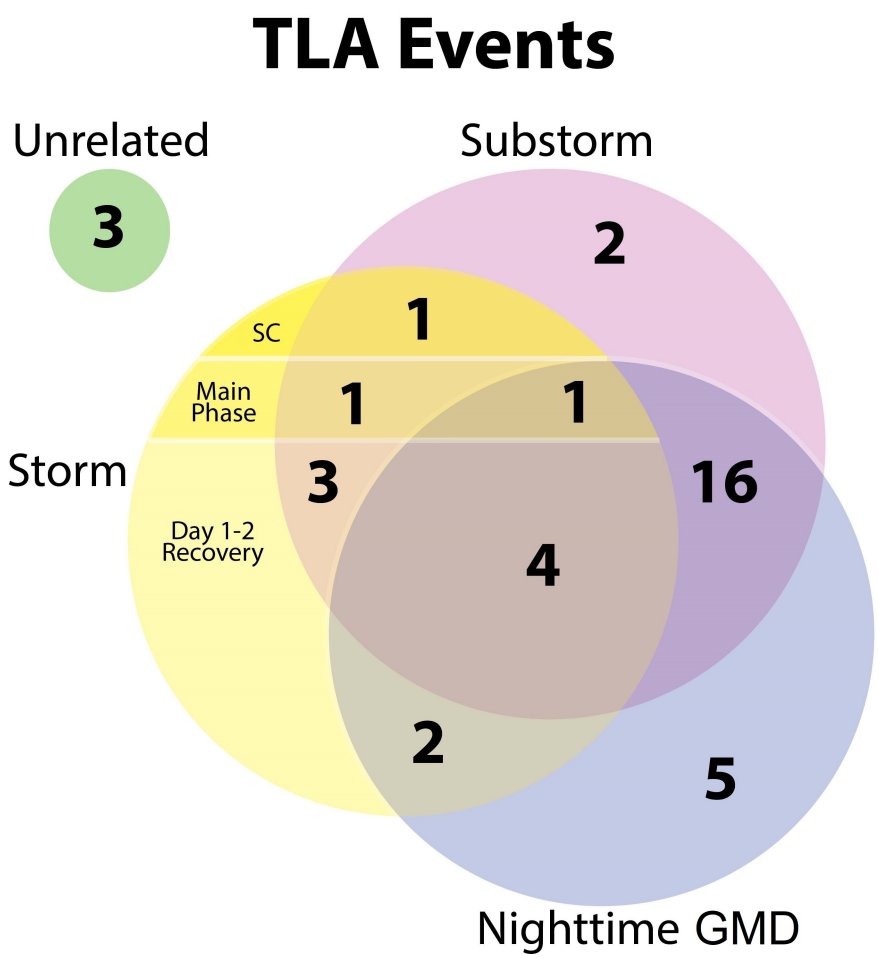

Figure 2.3: Venn diagram of number of TLA events related to geomagnetic storms (with cells specified for storm phases), substorms, and nighttime GMDs, as well as the distinct unrelated events.

2.5 Discussion and Conclusions

While TLA dB/dt variations do not drive GICs directly, we show here that they often occur in close relation to or within larger geomagnetic disturbances- like substorms and nighttime GMDs- that can cause GICs. We found that SCs were not the main driver for TLA events; though the large SC that occurred on 22 June did cause the largest amplitude perturbation, it was the only TLA event associated to an SC despite many occurring over the course of the year. There is a strong association of these events to the onset of substorms as well as an association to nighttime GMDs, but it can be seen in Figure 2.3 that this is not a perfect correlation (i.e., not all nighttime events are substorm-related). The relationship with substorm onsets appears to be a complicated one, as several events occurred multiple hours after the nearest substorm onset, and many of the substorm-related events also occurred during the main phase or recovery of a geomagnetic storm.

In addition to a clear association to substorm onsets, we found that a majority of our events either preceded or occurred within a nighttime GMD (Engebretson et al., 2019a). These nighttime GMDs are large-amplitude magnetic disturbances with 5-10 minute timescale; the study surveyed GMDs observed in this region of north-east Canada from 2014-2017. Like GMDs, the TLA events identified were often, but not always, associated with substorms on a similar two-thirds basis. Using the spherical elementary current systems (SECS) method (Amm and Viljanen, 1999) and the implementation of this technique by Weygand et al. (2011), a superposed epoch analysis was conducted to investigate the average equivalent ionospheric currents (EIC) and inferred field-aligned currents (FAC) during 21 nighttime GMDs that occurred at CDR from mid-2014 to 2016. Engebretson et al. (2019a) found that the largest of these GMDs were associated to intense westward ionospheric currents 100 km above CDR, coinciding with a region of shear between upward and downward FAC. They also found that the largest horizontal dB/dts occurred slightly south of CDR in a localized region of $\sim$275 km. Our TLA events show some similarities to these GMDs: 1) Of all six stations, the PGG and CDR stations measured the greatest number of events as well as the largest-amplitude events ($|dB/dt| \geq$10 nT/s) and 2) we found only ten events that were measured by more than one station, so the majority of our events ($\sim$73.7%) were measured locally at just one station. The localized nature of many TLA disturbances implies that the source currents are localized in the ionosphere (Boteler and Beek, 1999).

More recent research has found extreme local enhancements of the geoelectric field with spatial scale $\sim$250-1600 km (Ngwira et al., 2015); these peak geoelectric fields occur during geomagnetic storms but are highly localized in nature, suggesting smaller-scale, localized ionospheric processes as a source mechanism. Ngwira et al. (2015) suggested localized substorm events as a possible source mechanism for generating localized geoelectric extremes, but the exact processes responsible is yet unknown. The tendency of TLA events to occur within some of the largest GMDs and soon after substorm onset suggests that the TLA dB/dts are signatures of rapid, small-scale ionospheric currents, which could be related to the localized substorm events proposed by Ngwira et al. (2015). However, TLA events also occurred independently of both substorms and GMDs, (as well as geomagnetic storms). Localized instabilities that often occur during substorms but can occur in association with other magnetotail phenomena were suggested by Engebretson et al. (2019a) as a cause for nighttime GMDs. Further investigation of the role of TLA dB/dts within nighttime GMDs may shed light on the fine-scale M-I processes responsible. Our future work will involve an expanded search for TLA events and will include a superposed epoch analysis to investigate the small-scale ionospheric current systems involved in driving TLA events.

In order to better understand our events in the context of these GMDs, we extended the upper threshold of the search algorithm to identify disturbances lasting up to 5 minutes with magnitude $>$ 6 nT/s. We found 25 additional dB/dts that were all related to TLA events that we had already

identified. Interestingly, only one signature lasted slightly longer than 2 minutes. We hypothesized that the absence of magnetic perturbations in the 2-5 minute timescale range could be due to algorithm bias. Because the method of the routine searches for changes in the direction of the slope (dB/dt) with the condition that the change last for at least 1 second, and we used raw magnetic field data without any smoothing method, it was possible that the algorithm could be missing collections of dB/dt signatures lasting 2-5 minutes because there are shorter timescale variations occurring within them that did not meet the threshold of 6 nT/s. To test this theory, we applied a 10-point sliding average filter on the magnetic field data (as was done in Engebretson et al. (2019a)) so that any of these shorter variations would be smoothed over, then ran the search algorithm for disturbances lasting up to 5 minutes again. When the data were smoothed, the algorithm identified all the same events as with raw data and identified 17 new events. With the smoothed data, all the events with signatures lasting > 60 seconds were the same apart from one case where the smoothed data marked the magnetic field response to the SC at RBY as a disturbance lasting 60.5 seconds rather than 34 seconds. This occurred in many cases where the 10-point smoothing altered the exact moment the signature started or ended (subsequently altering the amplitude characteristics as well). While the smoothing method resulted in many signatures marked as having longer duration, there was still only a small number of dB/dts with > 1 minute timescale (32 as opposed to 25 with raw data) and the longest signature lasted 147 seconds. By comparing our results with smoothed data, we verified the methodology of the algorithm and determined that the absence of large-amplitude (> 6 nT/s) magnetic disturbances with timescale 2.5-5 minutes is not due to algorithm bias. This finding suggests that all longer-timescale magnetic perturbations at these stations consist of more rapid variations lasting less than $\sim$2.5 minutes, with a vast majority < 60 seconds.

What we learned from the error analysis of this study is that a common smoothing method on the data altered the timing and amplitude of the events (sometimes removing signatures altogether), suggesting that the short-timescale nature of the geomagnetic field could often be altered with common data processing methods or missed altogether with 1-minute or even 10-second averaged magnetic field data. While TLA events show a clear association with substorm activity as well as many shared characteristics with nighttime GMDs, they are not consistently related to these space weather events. We found a small subset of TLA events that are unrelated to geomagnetic storms, auroral substorms and nighttime GMDs. TLA events show a localized behavior with a weak association to geomagnetic storms, suggesting that there are other physical mechanisms, even beyond substorms, for localized extreme enhancements in the geomagnetic field. Finally, we show that these signatures can have amplitude of the same order as events that can drive GICs and they often occur in close temporal relation to or within these longer-timescale disturbances. Our future work will include a statistical analysis on an expanded set of TLA events to investigate the physical processes in the M-I system driving them and their relation to current-inducing events.

CHAPTER 3

Automated High-frequency Geomagnetic Disturbance Classifier: A Machine Learning Approach to Identifying Noise while Retaining High-Frequency Components of the Geomagnetic Field

This chapter presents a methodology for a technique to identify high-frequency dB/dt in magnetic field data and classify it at either noise-type or geophysical. This work was published in the AGU Journal of Geophysical Research: Space Physics under the title "Automated High-Frequency Geomagnetic Disturbance Classifier: A Machine Learning Approach to Identifying Noise While Retaining High-Frequency Components of the Geomagnetic Field" (McCuen et al., 2023b). The research is presented as published with minor formatting adjustments and removal of a repeated figure from Chapter 2. The data used for this analysis as well as the fully automated geomagnetic disturbance classifier are available on the University of Michigan's Deep Blue data repository (doi.org/10.7302/78zf-yw59).

3.1 Introduction

Space weather occurs due to solar disturbances such as solar flares and coronal mass ejections that activates magnetohydrodynamic and electromagnetic disturbances that propagate throughout the magnetosphere-ionosphere (M-I) system down to the surface of Earth. One ground manifestation of severe space weather events is geomagnetically induced currents (GIC), perhaps the most critical space weather concern. Flowing through man-made conductors on Earth like railways, pipelines and power grids, GICs can be large enough to cause damage to transformers resulting in major power outages and costly equipment damage (Pulkkinen et al., 2017). GICs are the result

of a horizontal surface electric field **E** induced in Earth's surface that is driven by large changes of the surface magnetic field, dB/dt, via Faraday's law of induction. Thus, the dB/dt is often used as a proxy to study GIC.

While large GICs often occur during global space weather events like sudden commencements (SC) and geomagnetic storms that cause major changes in the global large-scale M-I currents, it has been known for some time that smaller-scale phenomena are capable of causing GICs as well. An example of such phenomena are nighttime geomagnetic disturbances (GMD), also known as nighttime magnetic perturbation events (MPE), that are often associated with substorm activity and may be a result of other magnetotail phenomena that commonly occurs during substorms (Engebretson et al., 2019a). GMDs have 5-10 minute timescales, relatively small spatial scales ($\sim$275 km) compared to global events and are related to localized ionospheric instabilities.

It was shown by Viljanen (1997) that smaller-scale ionospheric currents play a key role in producing very large dB/dt at the surface. Several recent studies also suggest that beyond the largest space weather disturbances, there are more rapid, localized and small-scale processes involved in generating some extreme GICs (Engebretson et al., 2021; Ngwira et al., 2015; Pulkkinen et al., 2015). Dimmock et al. (2020) found that the localized horizontal magnetic field derivative can vary by a factor of three times the spatial average and thus these regional extremes are not accurately represented in global geomagnetic activity indices. Further, Dimmock et al. (2020) found that enhancements in regional dB/dt are linked to increased energy deposition in the magnetosphere mapping to local ionospheric structures and thus play a key role in modeling GIC during strong storms.

Less is understood about rapid and regional dB/dt enhancements because magnetic field data with 1-minute temporal resolution has long been the accepted standard in space weather research. This is because higher-frequency, second-timescale variations are effectively low-pass filtered when computing the geoelectric field (Pulkkinen et al., 2006, 2013). However, these second-scale magnetic field changes may be especially important in understanding small-scale dynamics of space weather events. While magnetic disturbances in this Pi 1-2 frequency range do not cause GICs directly, they have been found to occur prior to and/or during some GIC-capable space weather events, nighttime GMDs in particular (McCuen et al., 2021).

We refer to rapid dB/dt enhancements as transient-large-amplitude (TLA) events: instances of high-frequency, short-timescale magnetic field variations ($<$ 60 s) that have large dB/dt values over 6 nT/s and occur within a 1-hour window. McCuen et al. (2021) (Chapter 2) found that TLA dB/dt intervals identified in 2015 often occurred in the pre-midnight sector (magnetic local time, MLT), 30 minutes after a substorm onset and in association to many of the most extreme nighttime GMDs. Of 175 GMDs at four MACCS stations in 2015 (IGL, RBY, PGG, CDR), nearly half of the 52 largest events (maximum dB/dt values greater than 10 nT/s) had associated TLA dB/dt intervals.

Engebretson et al. (2019a) used a superposed epoch spherical elementary current systems (SECS) analysis on 21 strong events at the CDR station to conclude that they were associated with westward overhead currents that coincided with a region of shear between upward and downward field-aligned currents (FAC). The TLA event in Figure 1 is one of these strongest GMDs identified at CDR in the study of Engebretson et al. (2019a); the example shows many TLA intervals within the GMDs and appears to exhibit a westward moving disturbance as the minimum of the negative bays in the Bx component appear successively in each station from east to west (see map of MACCS stations in Section 3.2). A westward current in the ionosphere can generate a magnetic field with field lines that point northward above the current region and southward below, resulting in large negative depressions in the Bx component of the ground magnetometers. While there is some evidence for the processes responsible for generating GMDs, their exact physical mechanisms and the current systems involved are still under investigation. Analyzing these higher-frequency perturbations within the GMDs and observing the ionospheric behavior during such events allows for more detailed understanding of regional dB/dt enhancements, small-scale ionospheric currents, the dynamics of shear regions between upward and downward FAC and the potential connection to other magnetotail phenomena.

While substorms and GMDs have minutes to tens of minute timescales, there is clear evidence of higher-frequency (<60 s) behavior within many of these events. Because many of the GMDs that exhibited TLA signatures were amongst the most intense events but were not related to the most extreme space weather events (i.e., SCs and/or global geomagnetic storms), this suggests that more localized, small-scale ionospheric currents are involved in generating these large disturbances. Further, because the GMDs that exhibited TLA intervals prior to or within the overall disturbance were some of the largest GMDs of the dataset suggests that TLA signatures may be good indicators of the strongest small-scale events that have the capability to cause GICs.

Analysis of the second-timescale behavior of the surface magnetic field is a pathway to understanding the small-scale dynamics of M-I current systems that can give rise to GIC. Studying these high-frequency signatures will improve the understanding of rapid and localized magnetic field behavior and associated ionospheric currents. This more detailed knowledge of the fine-scale nature of the geomagnetic field can aid in improving modeling and forecasting of space weather events.

While it is necessary to analyze high-frequency TLA variations in ground magnetic field data in order to advance our understanding of small-scale M-I dynamics, the challenge in this task is retaining these high-frequency signatures in global magnetic field databases. Advancements in technological capabilities (Love and Finn, 2017) and the need for improved accuracy in measuring dB/dt (Tõth et al., 2014) have motivated the shift toward using higher temporal resolution magnetic field measurements for space weather applications. However, common data processing methods

often reduce or remove transient-large-amplitude signatures via their data cleaning or noise removal procedures because the signatures are similar in amplitude and timescale to that of magnetometer noise. The term magnetometer noise refers to two main sources of error in magnetometer readings: instrumental defect and/or magnetic deviation caused by interference of ferromagnetic materials (e.g., cars, technological devices, other instrumentation) in the vicinity of the magnetometer (Nguyen et al., 2020). Either of these sources can cause rapidly varying and irregular data measurements that have similar amplitude and timescale characteristics to TLA signatures.

Because of the similarity of noise-type data to TLA signatures, the geophysical TLA dB/dt are often reduced or removed with the noise signatures in common data processing procedures. Intermagnet, a worldwide magnetometer database commonly used for M-I and GIC research, uses a frequency band pass filter of 0.008-0.2 Hz (5-125 seconds) on 1-second data to remove error artifacts (St-louis et al., 2014). SuperMAG is a widely-used, global magnetic field data collaboration that provides uniformly processed data from over 300 ground based magnetometers (Gjerloev, 2012). SuperMAG offers 1-second (averaged if raw data has higher resolution) resolution magnetic field data that has undergone an automated data cleaning procedure. Both of these procedures can alter or remove higher-frequency variations of the field. Beyond data processing procedures by commonly used databases, many magnetic field data are averaged over 1-minute or more in practice for GIC and space weather studies. Even though many magnetic field arrays offer 1-second magnetic field data, the data averaging and processing techniques used often remove or modify TLA variations.

The problem remains, TLA variations that are important to retain for space weather studies can be removed or reduced in common data cleaning and processing, but are difficult to distinguish from noise in raw data. Numerous methods have been used to characterize and statistically analyze noise in magnetometer data (Khomutov et al., 2017; Nguyen et al., 2020) but challenges in anomaly detection have motivated the use of more modern machine learning techniques to identify and remove outliers from magnetometer data (Mitra et al., 2020; Xu et al., 2020). The data cleaning process for large magnetic field databases usually requires an experienced magnetologist to determine whether some signals are natural or noisy. In the case of TLA signatures that are similar in frequency and amplitude to error artifacts, machine learning algorithms can be especially useful for making these types of determinations without the need for human supervision.

In this chapter, we present the full methodology for a geomagnetic disturbance classifier that identifies occurrences of high-frequency (0.017-1 Hz) signals in magnetic field data and classifies whether they are a result of noise interference or geophysical sources. This process utilizes statistical characteristics of both noise-type and geophysical dB/dt signatures to define a high frequency geomagnetic disturbance event and implements a machine learning classification algorithm to classify the dB/dt signatures by their sources.

This chapter is organized as follows. Chapter 3.2 describes the magnetometer data used in this study and section 3.3 outlines the dB/dt search algorithm. Chapter 3.4 discusses and illustrates the noise-shapes identified in data from MACCS, and Chapter 3.5 describes the statistical characteristics of the noise-type and TLA dB/dt intervals and events. The filters implemented into the search algorithm based on the analysis of Chapters 3.4 and 3.5 are explained in Chapter 3.6. In Chapter 3.7, the machine learning approach used to fully automate the search algorithm is described and the results discussed (the cross-validation process is detailed in Appendix B.1.) Chapter 3.8 examines the effect of a common data processing procedure on the high frequency signatures being studied and discusses the data products provided by the procedure developed. Finally, Chapter 3.9 discusses our results and the implications for space weather studies followed by our conclusions.

3.2 Data Sets

This study uses magnetic field data from three geomagnetic and space physics magnetometer databases, as well as data processed through the SuperMAG data service that includes all three databases. The MACCS data are used for the initial identification of TLA dB/dt signatures and the noise classification for algorithm improvement. Then, we use data from a magnetometer site within the Athabasca University THEMIS UCLA Magnetometer Network eXtension (AUTUMNX) (Connors et al., 2016) as well as data from the CANadian Magnetic Observatory System (CANMOS) (Nikitina et al., 2016) to compare how well the dB/dt search process performs on magnetic field data from different systems.

Station	Geographic Latitude	Geographic Longitude	Corrected Geomagnetic Latitude	Corrected Geomagnetic Longitude
IGL	69.3	278.2	77.6	355
GJO	68.6	264.2	76.8	329.8
RBY	66.5	273.8	75.2	347.2
PGG	66.1	294.2	73.2	19.9
CDR	64.2	283.4	72.6	3.0
IQA	63.8	291.5	71.4	15.2
INUK	58.8	281.9	67.6	0.02
NAN	56.4	298.3	63.1	22.5

Table 3.1: Location coordinates of stations used in this study.

The geographic and geomagnetic coordinates of the magnetic observatories used in this study are listed in Table 4.1 and shown on the map in Figure 4.1 with lines of corrected geomagnetic (CGM) latitude and longitude for 2015. The CGM coordinates were calculated using the AACGM-

v2 Calculator (available at http://sdnet.thayer.dartmouth.edu/ aacgm/aacgm_calc.php#AACGM) for epoch 2015.

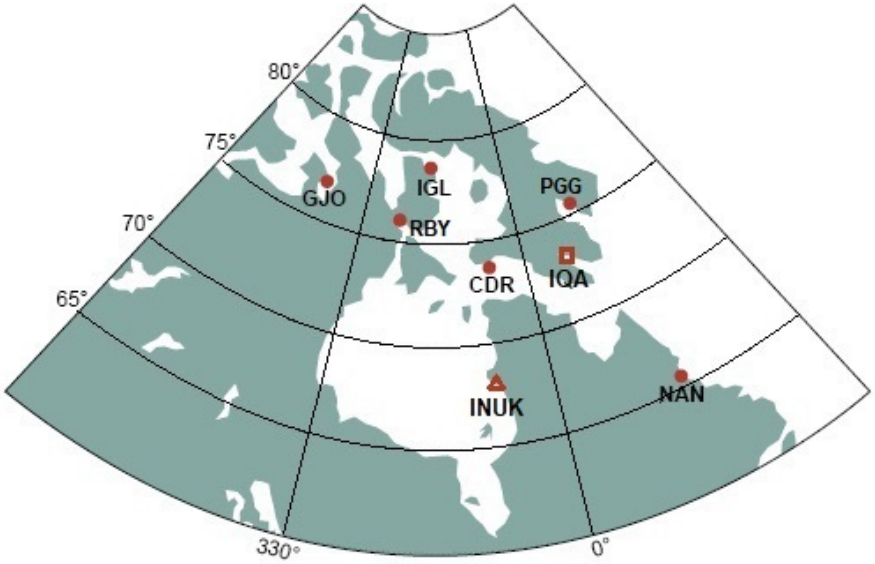

Figure 3.1: Station locations shown on a map of Nunavut, North-East Canada. Circles represent locations of MACCS stations, the square is the location of the CANMOS IQA station and the triangle signifies the AUTUMNX INUK station. Lines of latitude and longitude are in corrected geomagnetic coordinates.

The ground-based stations used in this study are all in the near vicinity of Inuit communities in arctic Nunavut, Canada. Many of the MACCS stations are located at the local airport, configured such that the computing instrumentation is kept inside the airport or nearby facility and the sensor is located away from the building inside a small, enclosed box on the ground. The IGL magnetometer sensor is located right within the local town of Igloolik near the Igloolik Research Centre where the rest of the station equipment is held. The PGG magnetometer is located $\sim$1 km outside of town near the Pangnirtung water reservoir. In all cases of the MACCS magnetometer stations, their locations make them susceptible to man-made noise interference from multiple sources (cars, snowmobiles, nearby facilities, etc.). The CANMOS station and AUTUMNX station are also susceptible to local interference from human activity, however these observatories are dedicated solely to magnetic field data acquisition and do not rely on local facilities like an airport to house instrumentation. This allows the CANMOS and AUTUMNX observatories to be located further from town centers and aids in prevention of noise contamination.

The magnetometers used in this study at the MACCS and the IQA station of CANMOS are Narod ringcore fluxgate magnetometers designed and supplied by Dr. Barry Narod of Narod Geophysics, Ltd., Vancouver, B.C., Canada (Hughes and Engebretson, 1997). The AUTUMNX in-

struments are THEMIS-class fluxgate magnetometers provided by UCLA (Russell et al., 2008) and based on the design for the earlier Sino Magnetic Array at Low Latitudes (SMALL) terrestrial vector fluxgate magnetometers (Gao et al., 2000).

The Narod magnetometers collect 8 samples per second in three axes, then average and record the data at two samples per second for MACCS data and one sample per second for the CANMOS data. The AUTUMNX magnetometers record the magnetic field at 2 Hz. The data used from AUTUMNX and CANMOS observatories have resolution of 0.01 nT, the MACCS data have a 0.025 nT data resolution, and all three have timing accuracy of at least 1 ms. The high-resolution, sampling rate and timing accuracy are sufficient to detect short-timescale Pi 1-2 pulsations. The magnetometer data used from MACCS and AUTUMNX are in geomagnetic coordinates: H (geomagnetic north-south), D (geomagnetic east-west) and Z (vertical). The data from CANMOS is in geographic coordinates: X (geographic north-south), Y (geographic east-west) and Z (vertical).

3.3 dB/dt Search Algorithm

We developed an initial algorithm to identify changes of the magnetic field with user-specified magnitude and duration. The initial algorithm works in the following main steps: 1) calculate the change in magnetic field strength (ΔB) divided by the timestep (Δt): dB/dt (or slope) between each pair of successive data points and label the sign of the slope (labeled as a -1 for negative slope, +1 for positive slope and zero for zero slope), 2) mark the points when the sign of the slope changes for at least two measurement cycles (i.e., local minima and maxima) and 3) recalculate the new dB/dt between the local minima and maxima and return the information if the signature also meets the user-specified criteria for timescale, minimum and maximum ΔB and dB/dt.

Because the search criteria are such that the slope must have the same sign for two measurement cycles (step 2), the algorithm relies on the sampling frequency of the data and should be used for magnetic field data with 1-second or higher temporal resolution for high-frequency studies. However, the same dB/dt search procedure can be performed on data averaged over a longer time period to identify dB/dt signatures with varying timescales (i.e., performing the dB/dt search algorithm on 1-minute averaged data will identify dB/dt signatures that last at least 2 minutes).

There is also an intermediate step after Step 1 that deals with the instances of zero slope that last only one measurement cycle: if a zero slope occurs only once in between two like-sign slope values, the sign of the slope is changed to match those slope values. This measure is taken so that a change in slope will only be marked in cases of zero slope if it persists for at least two measurement cycles and is consistent with the minimum dB/dt search to be intervals that last twice the sampling frequency. The final product returned from the algorithm is a nine column matrix; each row represents an individual dB/dt interval and provides the start and end time of the interval,

start and end B value, the time elapsed: dt, the change in magnetic field amplitude: ΔB, and the total perturbation: dB/dt. The final two columns indicate the component that the interval was identified in and the station at which the interval took place.

The method was developed to identify high-frequency (0.017-1 Hz) transient-large-amplitude (TLA) events in the magnetometer data. We define an event as any number of geomagnetic signatures with $<$ 60 seconds timescale and dB/dt $>$ 6 nT/s within a 1-hour event window. The hour windows are defined by the UT clock and determined by measurement frequency (i.e., number of data points in one hour) and are divided consecutively. For example, for a measurement frequency of 2 Hz, the first 7200 data points define the first hour window, and the next hour window is the following 7200 data points. The determination of event windows to have a duration of 1-hour was based on the observed groups of geophysical TLA dB/dt intervals; many TLA occur within a larger 5-15 minute negative bay and could include TLA dB/dt in the 15-20 minutes prior or after the bay (an example of such a TLA event is shown later in Figure 3.6), so 1-hour windows would encompass all of these related TLA dB/dt within one event. Further, there was always at least 1-hour between TLA event windows and often multiple hours or days, so extending the event window time to a relevant timescale (like 90 minutes or 2 hours) did not change the number of TLA events.

The minimum dB/dt threshold was chosen as it is comparable to magnetic field measurements during the March 1989 geomagnetic storm that caused the HydroQuebec power grid failure (Kappenman, 2006). This was the most severe geomagnetic storm of the twentieth century and maximum magnetic field changes during that storm were on the order of 8 nT/s (but lasting much longer than just seconds), so dB/dt of this magnitude are considered large-amplitude.

Unfortunately, these specifications also describe the signals that can occur as a result of instrumentation error or interference by ferromagnetic material (i.e., ”noise”). The term noise is relative to the specific goal of the measurement or problem to be solved. For this study, we use the term noise to refer to two main sources of error in magnetometer readings: instrumental defect and/or magnetic deviation caused by interference of ferromagnetic materials in the vicinity of the magnetometer (Nguyen et al., 2020).

3.4 Noise Shapes Identified in MACCS Data

In order to capture all such magnetic signals of interest with this timescale, we set the initial criteria for the dB/dt search to signatures with 1-60 second timescale, ΔB 6-10,000 nT and dB/dt from 6-1000 nT/s. The similarity of TLA events to noisy signals resulted in the algorithm identifying a majority of signals that were due to noise rather than natural geophysical processes. Because the size and timescale of these signatures fall into the same ranges (and thus the power spectra of geophysical and noise-type events were nearly identical as well), and common data cleaning

techniques can alter or remove TLA signatures, determining whether a given signal is of geophysical nature or a result of noise was done by examining the shape of the signal, the behavior of the magnetic field prior to and after the signal, and the amplitude characteristics of the interval. Thus, we manually separated the noise signals from the natural geophysical perturbations by comparing with the magnetic noise characterization of Khomutov et al. (2017).

The noise shapes described in Khomutov et al. (2017) are compiled from Intermagnet data from observatories located in the mid-latitude, eastern hemisphere. The observatories have various types of fluxgate magnetometers with measurement frequency from 0.2-2 Hz (5-0.5 seconds). The main sources of noisy signals in magnetometer data are both external and internal. Externally, there are large-scale noise sources like DC railways that can impact magnetic field data at large distances, and there are more local sources of ferromagnetic and/or conductive material within the nearby vicinity of the magnetometer sensor. Internally, noisy signals can arise from instrumentation error. While the exact source of a specific noisy signal can vary, the main sources are consistent across observatories and databases. For these main sources of interference with fluxgate magnetometer systems, the characteristic shapes and sizes of the resulting noisy signals in the data are common (Neska et al., 2013; Santarelli et al., 2014; Khomutov et al., 2017). The four most common shapes of noise and their characteristics reported by Khomutov et al. (2017) are defined and illustrated as follows.

Spikes in magnetometer data are large-amplitude ($\sim$ tens of nT), relatively short signals (generally lasting less than a few seconds) with well-defined leading and back edges that have similar amplitudes. Isolated spikes, spikes with large amplitude (many tens of nT), and spikes that last only one measurement cycle have a low probability of being caused by geophysical sources. An example of a spike is shown in Figure 3.2: 1-minute of MACCS magnetometer data taken at the PGG station on 2 July, 2015. The hollow red circles represent the start of a dB/dt interval that is > 6 nT/s and the solid red dots represent the end of the signature. Note that in this example, the starting point of the first dB/dt intervals in the Bx and Bz components appear to occur prior to the start of the visible decrease in the field. This is because the magnetic field strength in the Bx and Bz components begins decreasing very subtly at the starting points marked with open circles in these components; these points mark the time that the field changed the sign of slope (to decreasing) for at least one second and if the slope increased within the intervals it was only for a half-second interval.

The mean B value of each component in the interval shown is subtracted from the data, but this does not change the ΔB and dB/dt amplitudes or the timescales of the intervals from the original data. The entire spike signature lasts about 20 seconds with each interval of large dB/dt lasting 3.5-10.5 seconds. The maximum amplitude of the spike is about 318 nT (dBx/dt beginning at 21:16:17.75 and decreasing for 8.5 seconds). We further define spikes in this noise classification

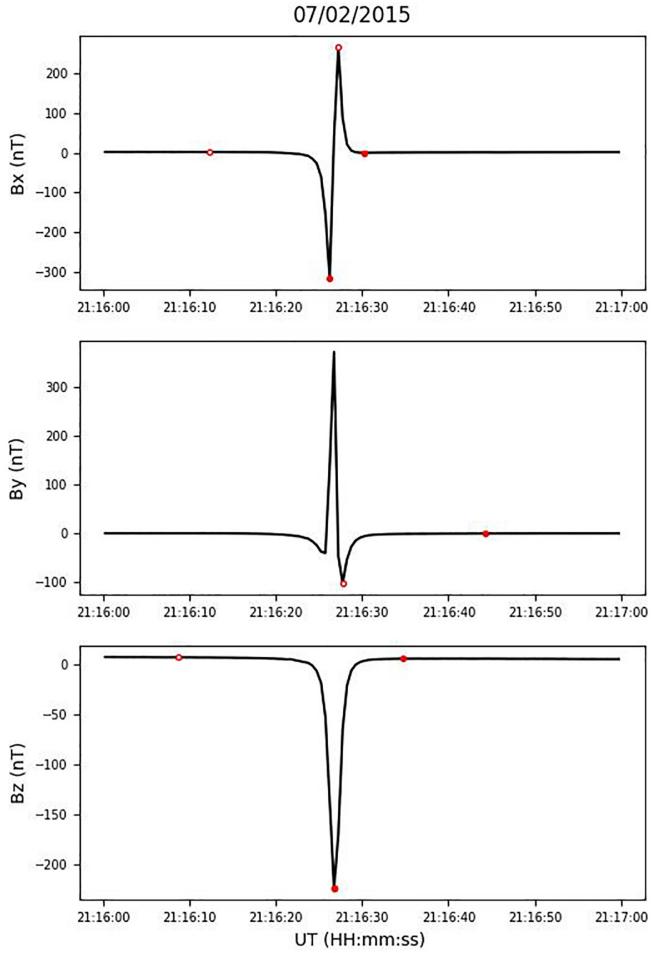

Figure 3.2: A spike in the magnetometer data that occurred on 2 July 2015 at the PGG station. The hollow circles mark the start of each dB/dt signature and the solid dots mark the end. Note that the consecutive solid red dots in the Bz plot (bottom) signify that the negative peak of this spike is both the end of the interval prior and the start of the interval following.

to be instances of three or less large dB/dt signatures (with < 60 s timescale and magnitude > 6 nT/s) occurring within a 1-minute interval.

Figure 3.3 shows an example of a jump shape in the MACCS data. Jumps are much like spikes but with a continuous interval between the leading and back edges. The timescales of these jumps vary; in this study, we specify jumps to have a minimum 1-minute interval sustained between the leading and trailing edges in which the magnetic field does not increase/decrease beyond the starting value of the leading edge (i.e., the very first hollow circle in all three panels of Figure 3.3 at approx. 15:18 UT). Jumps often occur due to changes of the magnetic field distribution via ferromagnetic material.

Random-like noise is usually caused by man-made disturbances which add randomized variations to the background magnetic field. These look like patches of highly frequent dB/dt intervals

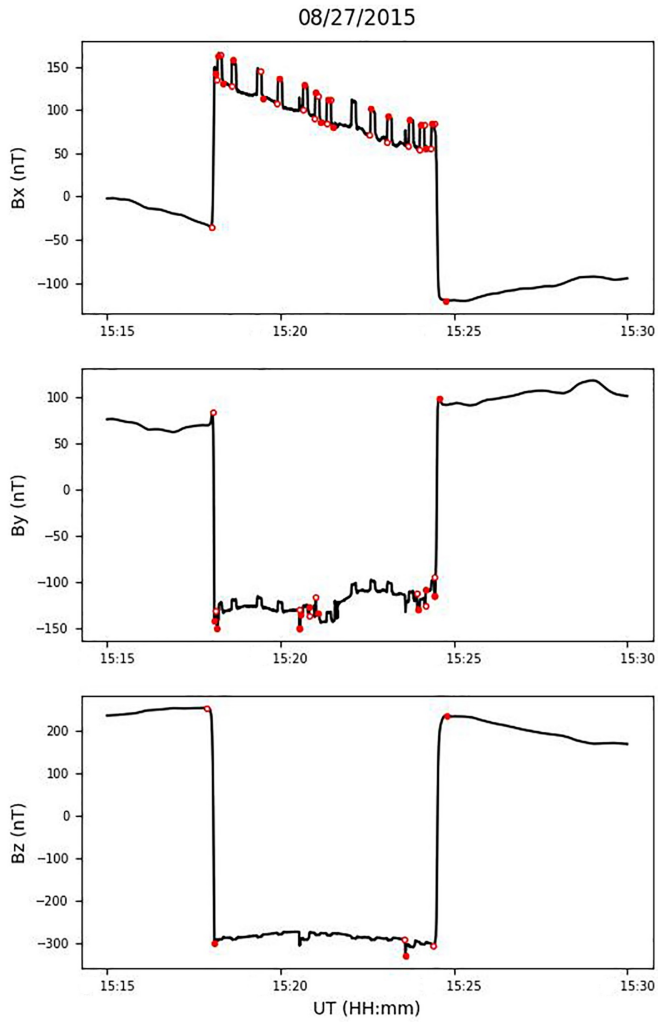

Figure 3.3: A noise jump that occurred at the CDR station on 27 August 2015. Hollow circles mark the start of a dB/dt signature and solid dots mark the end. The mean B value of each component in the interval shown is subtracted from the data.

with randomized shape and amplitude. An example of random-like noise is shown in Figure 3.4. This patch of random noise lasted about 7-minutes; the algorithm identified 93 dB/dt signatures from the three components combined. Figure 3.4b is a zoomed view of a section of this event from 10:16:10-10:17:10 UT showing how some of these variations are presented on a 1-minute timescale. Figure 3.4b shows that, on a 1-minute timescale, these magnetic field variations have dissimilar shapes to classic spikes as defined above although they may appear to be a group of frequent spikes when observed on a slightly longer timescale. While the shape of these magnetic field changes cannot be defined as spikes or a jump, we determine that they are noise variations because of 1) the highly frequent nature and the randomized shapes of the dB/dt intervals, 2) the jagged behavior of these variations on a second-scale (Figure 3.4b) and 3) the shape of the noise group on

a minute-scale (Figure 3.4a) that appears to positively deviate from the background magnetic field in each axis.

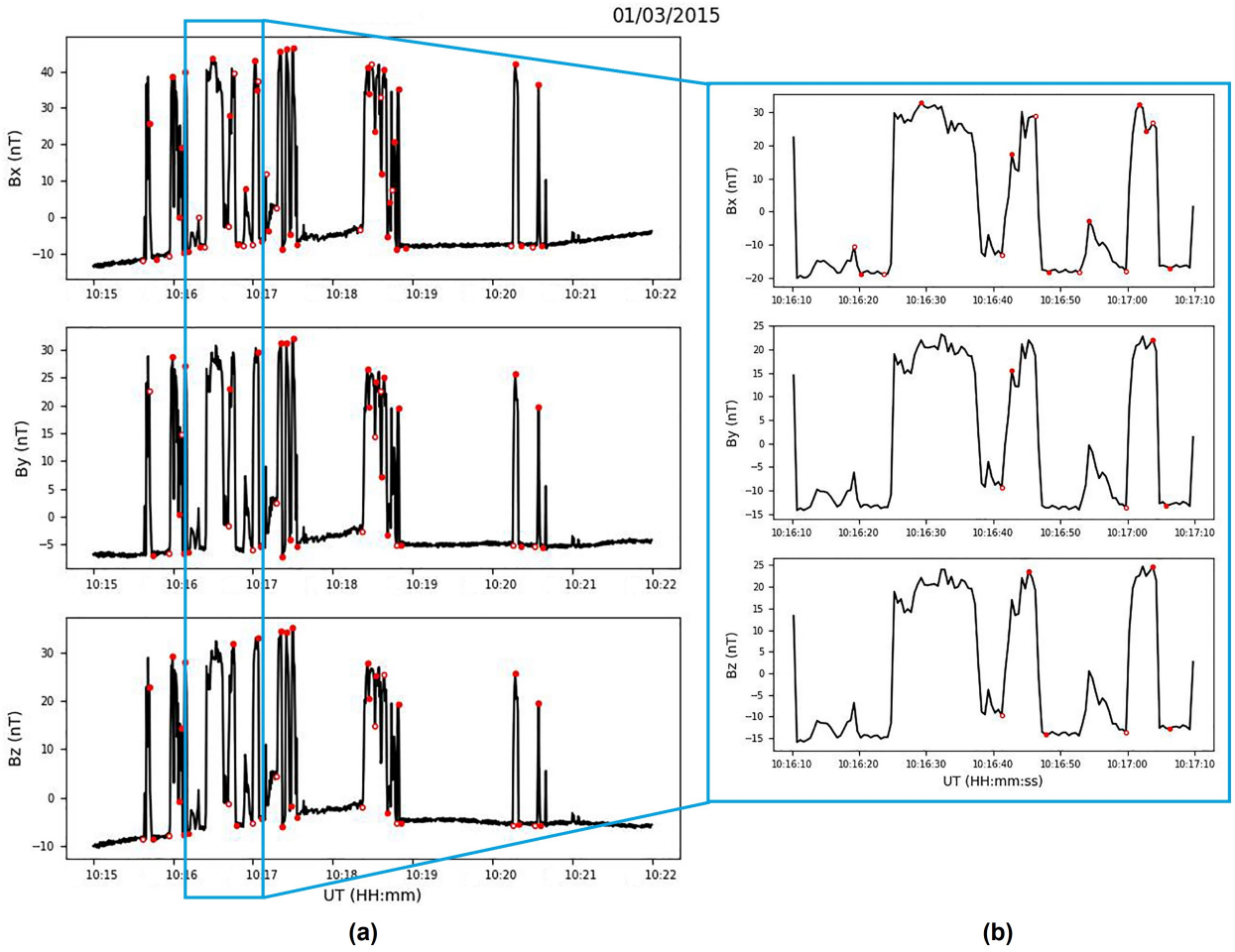

Figure 3.4: (a): Random-like noise that occurred at the IGL station on 3 January 2015. Hollow circles mark the start of a dB/dt signature and solid dots mark the end. (b): A zoomed-in view of 1-minute of the random-like noise-type event shown in (a). The mean B value of each component in the interval shown is subtracted from the data.

The last noise shape found in the MACCS magnetometers throughout 2015 is bay-like noise. An example of bay-like noise is shown in Figure 3.5b: a disturbance that occurred within 1-minute at the PGG station on 20 June 2015. The full high-frequency disturbance event (Figure 3.5a) consists of a bay-like disturbance as well as three separate spikes later in the hour window (note that just 25 minutes of this event are shown to emphasize the shape of the high-frequency intervals within this hour window). The bay-like disturbance is shown with a zoomed view in Figure 3.5b. The magnetic field changes in Figure 3.5b are near 50 nT in the x- and y- components but nearly 150 nT in the z-component. This is a common manifestation of noise in magnetometer data, usually

caused by magnetic field changes near the instrument due to a moving ferromagnetic object (i.e., a vehicle or other instrumentation). It is shaped like a positive/negative magnetic bay that persists for the duration of the passing object (usually seconds). Bay-like noise often has sharp leading and trailing edges like spikes or jumps, but the behavior between these edges is more random and variable. These impulses can be difficult to distinguish from natural signals because negative and positive bays can also occur due to M-I sources. While bay-like noise events have similar shapes to TLA events, the distinction between them is that TLA events often occur within a bay that lasts 5-15 minutes (see TLA event examples in Chapter 2) while noise-type bays generally have a duration of just seconds. Further, this example is decided to be a noise-type event because of the jagged magnetic field variations on a second-timescale, as well as the very similar and smooth behavior of the magnetic field prior to and after the disturbance bay: a common characteristic of noise-type events in magnetic field data.

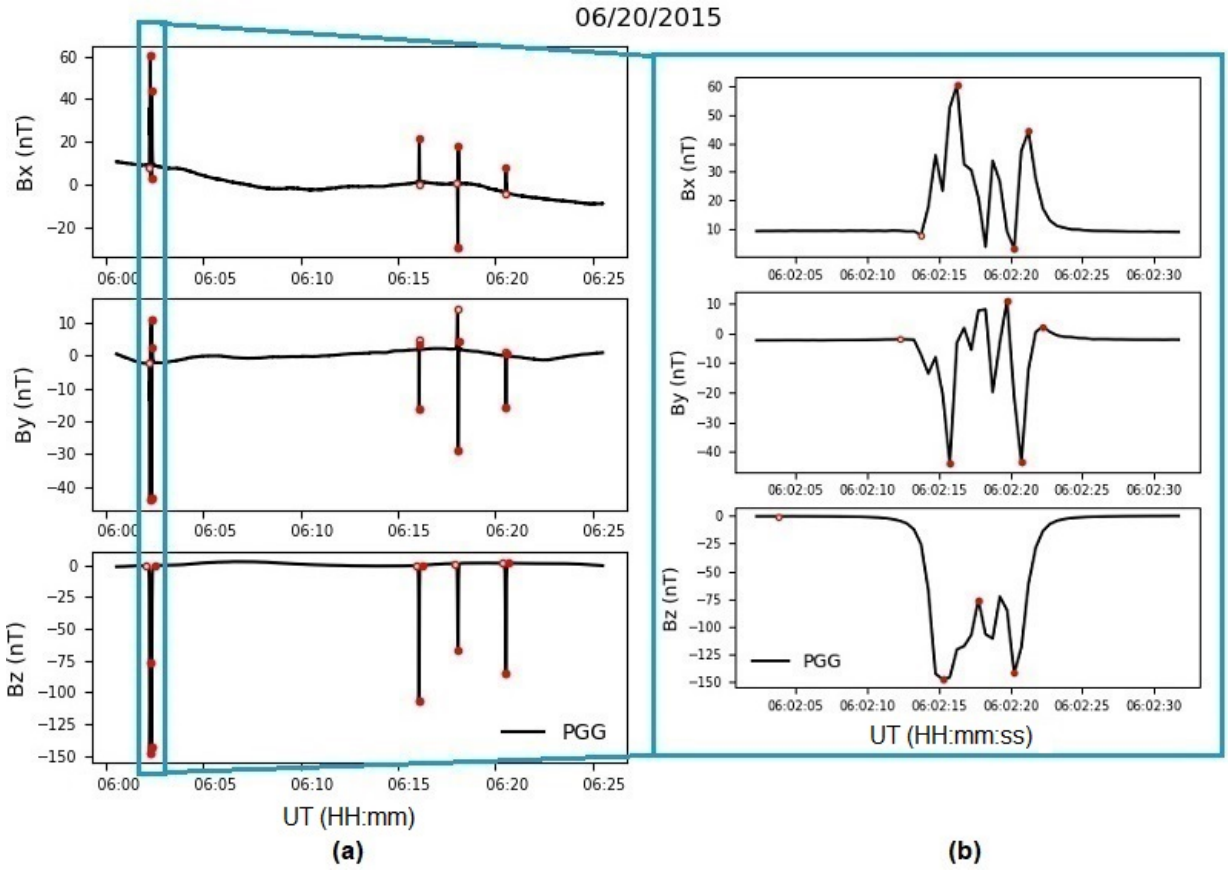

Figure 3.5: (a): A noise-type hour-event that occurred on 20, June 2015 at the PGG station consisting of a bay-like disturbance and three spikes. (b): Bay-like noise in MACCS magnetic field data. Hollow circles mark the start of a dB/dt signature and solid dots mark the end. The mean B value of each component in the interval shown is subtracted from the data.

Figure 3.6 shows an example of a TLA event that occurred on 10 November 2015. The figure

shows dB/dt signatures that occurred at the PGG station but there were also TLA dB/dt observed at two other MACCS stations during this hour. These signatures at the PGG station occur prior to (in the Bx component) and within a large nighttime GMD that began at 00:36 UT. There are twelve total dB/dt signatures in the full event shown in Figure 3.6a with average ΔB of about 274 nT, mean Δt of 33.8 seconds and mean dB/dt of just under 8 nT/s. Figure 3.6b shows one-minute of zoomed-in data from this event from 00:41:30 to 00:42:30 with one TLA-type dB/dt signature in the x- and z- component each. The signature in the z-component of Figure 3.6b has the largest dB/dt amplitude of the event of 10.37 nT/s. Figure 3.6b shows that on a 1-minute timescale, these are smooth changes of the magnetic field rather than jagged edges of noisy data. This is a distinct characteristic of TLA events with geophysical sources: the magnetic field is smoothly varying on a second-timescale rather than rapidly changing with sharp edges as observed in noise-type events.

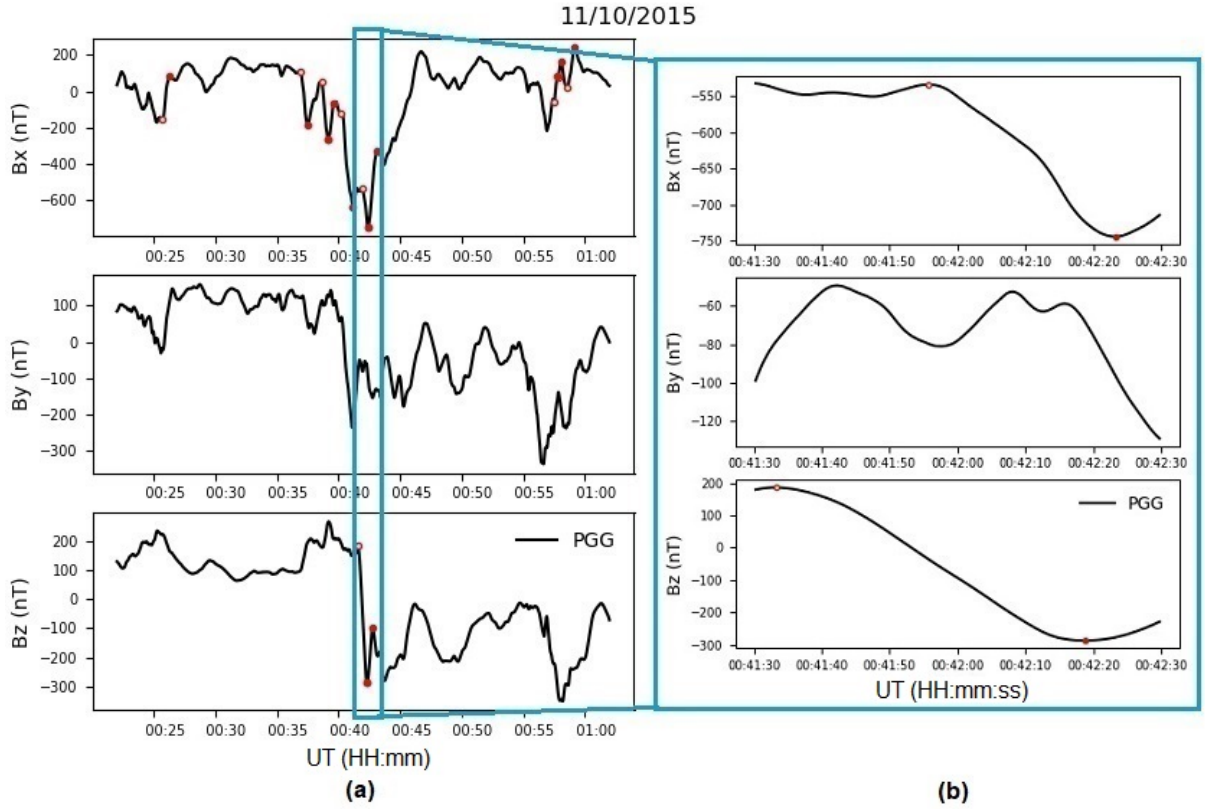

Figure 3.6: (a): A transient-large-amplitude (TLA) geomagnetic event that occurred on 10 November 2015 at the PGG station. Hollow circles mark the start of a dB/dt signature and solid dots mark the end. (b): A zoomed-in view of 1-minute of the TLA event shown in (a). The mean B value of each component in the interval shown is subtracted from the data.

The common feature of these noise shapes in magnetometer data is that they are composed of some combination of second-timescale magnetic field changes with dB/dt $>$ 6 nT/s. These are characteristics equal to that of the geophysical TLA dB/dt that are meaningful in the context of

small-scale M-I currents. However, the TLA event in Figure 3.6 shows dB/dt intervals occurring prior to or within nighttime GMDs that are associated to small-scale ionospheric currents and these TLA dB/dt intervals show smooth variations on a 1-minute timescale.

There are some distinct differences between the dB/dt signatures that arise from noise sources and TLA dB/dt caused by M-I sources. Noise-type dB/dt events can often be identified by the shape of the event, the behavior of the magnetic field prior to and after the event (the highly similar and often steady nature of the magnetic field on either sides of the noise-type perturbation) and the smoothness of the magnetic field on a second-timescale (noise-type events often show sharp magnetic field changes on a second-timescale whereas TLA dB/dt events are always smoothly varying on such fine timescales). These criteria were used to manually separate noise-type and TLA events. This manual classification method based on the descriptions in the study by Khomutov et al. (2017) was expert-verified by one of the co-authors of this study. From the manual separation of events, the numerical characteristics of the dB/dt signatures of each event type were then used to create filters to automatically classify noise-type and TLA dB/dt signatures, discussed in greater detail in the following section.

3.5 Statistical Characteristics of Noise-Type and TLA Events

While some shapes of noise signals are more likely to result from either man-made sources or internal instrumentation issues, all four of the noise types described in section 3.4 can arise from both hardware and external sources. Determining the exact source of noise in magnetic field data can be a challenge, but separating geophysical magnetic signatures from data contaminated with noise from outside interference is a more tangible task. After collecting all dB/dt signatures that satisfy the conditions for a high-frequency event (dB/dt $>$ 6 nT/s, dt from 1-60 s), we manually classified the geophysical events, as well as each type of noise shape identified. Then we analyzed the statistical characteristics of these types of dB/dt events to improve the selection criteria for the search algorithm. The statistical characteristics that set geophysical TLA events apart from noise-type events are described and compared below.

Noise-type events, whether from instrumentation error or external interference, contribute significantly more dB/dt events than geophysical events. From the six MACCS stations throughout 2015, we identified 215 TLA dB/dt (making up 59 separate events) and 845,572 noise-type dB/dt signatures (making up nearly 5500 separate events). Figure 3.7 shows histograms of the number of noise-type dB/dt (orange) and the number of TLA dB/dt (blue) based on their timescale (dt), amplitude (ΔB) and magnitude (dB/dt). All three histograms show the number of events on a logarithmic scale. Figures 3.7b and 3.7c both include a zoomed-in view of the bottom left corner of the full distribution showing the portion containing the geophysical events. It can be seen from all

three plots that the number of noise-type dB/dt identified is orders of magnitude larger than that of TLA dB/dt.

Figure 3.7a shows that noise-type dB/dt signatures were far more likely to last less than 10 seconds whereas TLA dB/dt had a relatively even spread of timescales from 3.5-60 seconds. Noise-type events at the six MACCS stations throughout 2015 had 99.8% of dB/dt intervals that lasted less than 10 seconds compared to just under 10% of the total TLA dB/dt. Further, all of the TLA dB/dt intervals that had dt $<$ 10 seconds occurred within hour event windows that had longer dB/dt from 10-60 seconds, whereas most of the noise-type hour events consisted solely of dB/dt intervals lasting less than 10 seconds. The uniform distribution of Δt of the TLA intervals shows that there are a relatively consistent number of meaningful geophysical signatures over the second-timescale range.

Figure 3.7b shows that noise-type dB/dt signatures were far more likely to be less than 60 nT in amplitude (94.9% of noise-type dB/dt had $\Delta B < 60$ nT/s compared to just 5.5% of TLA dB/dt signatures), however the noise also contributed to outliers thousands of nT higher than any of the TLA dB/dt which had a maximum ΔB = 580.75 nT. A similar trend is seen in the histogram of dB/dt magnitudes (Figure 3.7c) where the TLA dB/dt occupy a small slice under the distribution of the noise-type dB/dt. The zoomed view of Figure 3.7c shows that the largest TLA dB/dt magnitude was $\sim$33 nT/s compared to many noise-type dB/dt magnitudes exceeding 200 nT/s. Reasonable magnitudes for the most extreme second-timescale magnetic field changes are from 40-110 nT/s (Kataoka and Ngwira, 2016).

Noise-type dB/dt signatures occurred more often than TLA dB/dt overall and they also occurred in higher concentration per 1-hour event window. The random-type noise signature was the most frequently occurring. As is shown in Figure 3.4, random-noise events usually sustained longer intervals of highly variable magnetic field that contributed hundreds, sometimes thousands, of characteristic dB/dt signatures while geophysical TLA events often had just a few TLA dB/dt within a longer $\sim$10-20 minute perturbation. We found that a noise event (within a 1-hour window) at an individual station had 154.6 dB/dt intervals on average while geophysical TLA events had an average of 3.2 dB/dt (maximums of 25 and 2370 dB/dt per 1-hour event window respectively). As previously mentioned, the hour windows are defined by the measurement frequency (i.e., number of data points in one hour) and are divided consecutively.

The number of 1-hour windows containing TLA and/or noise-type dB/dt per station is shown in Table 3.2, as well as the number of individual dB/dt signatures identified at each station. In order to numerically describe the distinction between the concentration of dB/dt per hour window for noise-type and TLA events, we calculated the ratio of number of noise-type or TLA dB/dt per event to the total number of dB/dt (with any timescale and any amplitude) within the event hour. Table 3.2 contains the minimum and maximum of these ratios. While TLA and noise-type

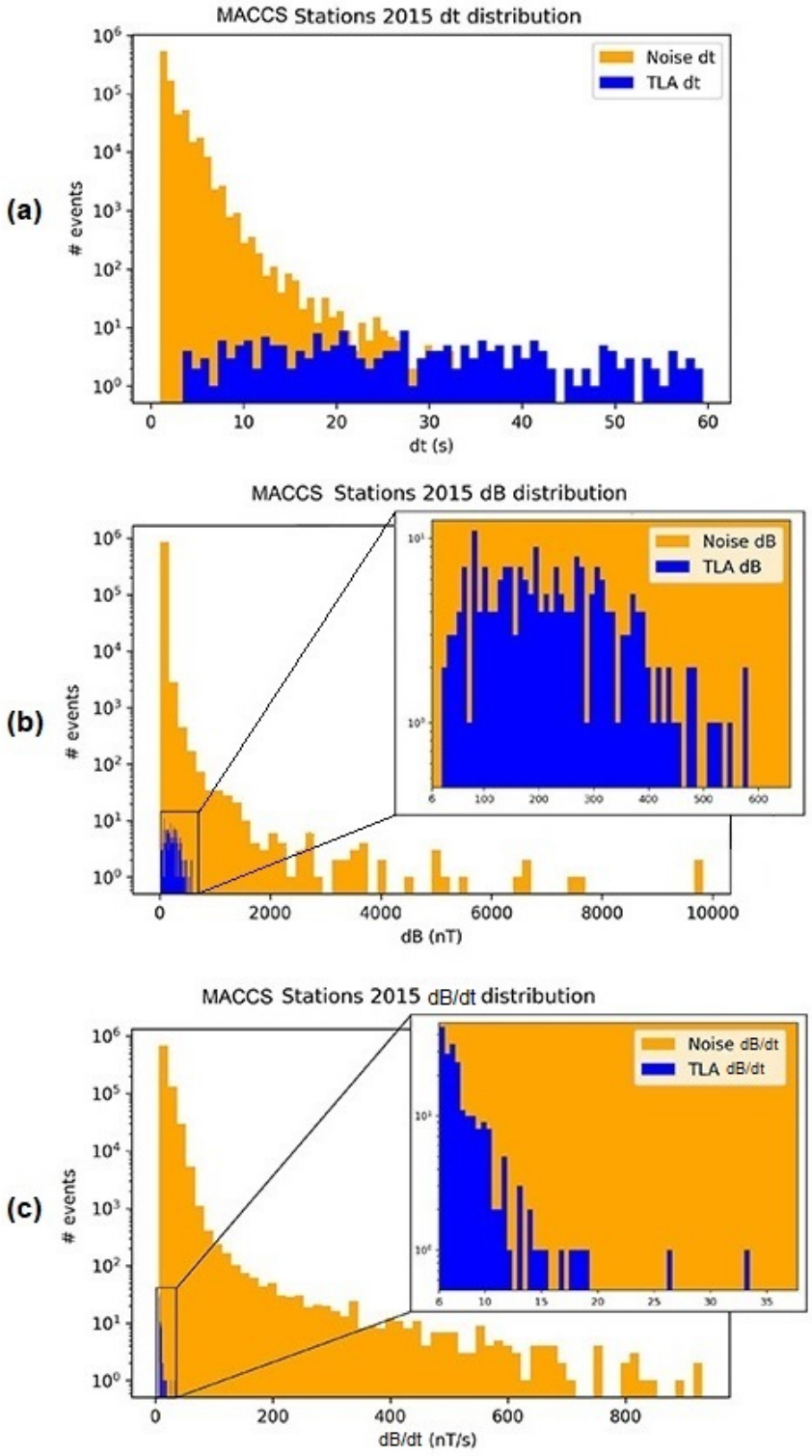

Figure 3.7: Histograms showing number of dB/dt signatures (separated by TLA and noise-type) from all six MACCS stations throughout 2015. (a): Distribution based on dt values, (b): distributions based on ΔB values and (c): distribution based on dB/dt values.

dB/dt events had similar minimum ratios (i.e., both event types exhibited events with very few or even singular high-frequency dB/dt intervals), the maximum ratios between TLA and noise-type dB/dt are very different from one another. TLA dB/dt never populated more than 4% of the total dB/dt within the respective hour event window, while noise-type events more often exhibited hour windows where the dB/dt composed of more than 10% and up to nearly 67% of all the magnetic field changes within the hour.

Station	Total dB/dt	# Noise windows	# TLA windows	Min ratio TLA:All	Max ratio TLA:All	Min ratio Noise:All	Max ratio Noise:All
IGL	33413	2159	4	0.0011	0.0069	0.0001	0.4377
GJO	1369	241	6	0.0019	0.0227	0.0004	0.6667
RBY	65800	991	7	0.0009	0.0085	0.0002	0.2117
PGG	1790	607	20	0.0006	0.0258	0.0002	0.0140
CDR	2353	695	15	0.0005	0.0355	0.0002	0.1998
NAN	741062	759	7	0.0008	0.0033	0.0002	0.5923

Table 3.2: Table showing number of 1-hour event windows that contain noise-type or TLA dB/dt, as well as the minimum and maximum ratios of TLA and noise-type to all dB/dt respectively.

It is worth noting that the maximum ratio of noise-type or TLA type is not directly proportional to the total number of noise-type or TLA event windows. For instance, the GJO station had the least amount of noise-type event windows, but the highest maximum ratio of noise-type to all dB/dt out of all the stations. This is to say that because the ratio is calculated based on the specific hour, it is dependent on the type of noise and how much there is and independent of the overall noise present in the station data.

To summarize the statistical characterization of geophysical TLA and noise-type events in this chapter, there are three main distinctions between geophysical TLA dB/dt events and noise-type dB/dt events:

1. TLA events have at least one dB/dt signature $>$ 6 nT/s that lasts 10 or more seconds within the 1-hour event window.

2. Large, second-timescale dB/dt are more likely to be of geophysical nature if they last from 10-60 seconds and have amplitude 60-1000 nT.

3. Large, second-timescale dB/dt are more likely to be noise if they occur in large concentration per 1-hour window (occupying more than 5% of the total magnetic field changes within the hour window). TLA-type events often have less than 20 dB/dt within an approximately 15-20 minute perturbation.

3.6 dB/dt Search Algorithm Filters

Following from the main characteristics described in the previous section, two main filters were applied to improve the dB/dt search algorithm and reduce the number of noise-type dB/dt identified by the routine. First: the dB/dt search is performed on consecutive 1-hour partitions of data and the requirements to determine a potential TLA event are specified as a 1-hour event window that contains at least one dB/dt that has magnitude 6-100 nT/s, ΔB from 60-1000 nT and timescale 10-60 seconds. Not only are the maximum values for ΔB and dB/dt decreased to the range observed for all TLA-type events, but the requirement that there be at least one signature lasting more than 10 seconds (and effectually having $\Delta B > 60$ nT) is implemented. If there are no signatures that meet this criteria in the hour window, the search procedure moves on to the next hour window. If there are any dB/dt that do fall within these values, the algorithm continues to the next stage.

In the second stage of the dB/dt search, dB/dt intervals with 6-100 nT/s, timescale 1-60 seconds and ΔB 6-1000 nT are identified (i.e., all of the high-frequency dB/dt signatures that could be TLA or noise-type), as well as the total number of dB/dt intervals with any amplitude and timescale within the hour. If the number of high-frequency signatures is more than 5% of the total number of the dB/dt within the hour, then the algorithm rejects all signatures identified. If this ratio is less than 5%, then the algorithm removes any intervals that last less than 2-seconds (as the minimum dt for all TLA events identified from the MACCS stations in 2015 was 3.5 seconds) and returns the remaining dB/dt intervals as the final data product. In this case where all TLA criteria are satisfied, the dB/dt search is also performed for 1-minute prior to the start time of the hour and 1-minute after the start time of the hour (as well as for the two minutes framing the end time of the hour) so that no dB/dt intervals are lost by being split by the hour partition.

The ratio method allows for the 5% threshold to depend on the individual station data and 1-hour environment which can be highly variable across magnetometer arrays, dates and times. In other words, if a station's data are overall highly variable (higher number of total dB/dt on average per 1-hour) then the 5% threshold allows for a larger number of dB/dt— comparative to the instrumentation and/or the surrounding magnetic environment— to be identified before rejecting the hour-window as containing only noise-type dB/dt. This ratio method is a general metric to reduce noise in magnetometer data based on the concentration of short-lived (< 60 s) and large-amplitude (> 6 nT/s) dB/dt intervals per 1-hour event window at an individual station.

To summarize the algorithm filters, the filtered dB/dt search returns magnetic field intervals with dt from 2-60 seconds, ΔB from 6-1000 nT and dB/dt from 6-100 nT *only if:* at least one of these signatures within the 1-hour event window lasts 10 seconds or more, and if these high-frequency intervals (along with those that last less than 2 seconds) do not populate more than 5% of the total dB/dt within the hour window. Implementation of the above conditions into the dB/dt

search process returned all of the same 215 TLA dB/dt and reduced the number of noise-type dB/dt returned by 99.6% (from 845680 to 2970 noise-type dB/dt). The numbers of both TLA and noise-type dB/dt prior to and after the filters are listed in Table 3.3. The filters removed all noise-type dB/dt from the RBY and NAN station, the latter of which had the most noise-type dB/dt in the unfiltered search. The IGL station had the most noise-type dB/dt remaining after the filtered search with 2,669 dB/dt.

Station	Total pre-filter	# TLA dB/dt	# Noise-type pre-filter	Total post-filter	# Noise-type post-filter
IGL	33413	20	33393	2689	2669
GJO	1369	14	1355	50	36
RBY	65800	32	65768	32	0
PGG	2353	61	1729	151	90
CDR	1790	69	2284	242	173
NAN	741062	19	741043	19	0
IQA	92	71	19	71	0
INUK	392	301	87	303	2

Table 3.3: Table with number of dB/dt intervals from 2015 of both TLA and noise-type, before and after the filters described in this section.

In order to better evaluate the performance of the dB/dt search algorithm and the performance filters, the dB/dt search routine was tested with and without the filters on one year of data from both a CANMOS observatory and an AUTUMNX ground magnetometer station. The IQA (Iqaluit) station from CANMOS and the INUK (Inukjuak) station from AUTUMNX were used for comparison because they are both in the same region of NE Nunavut as the other stations used in the original dB/dt study. We used all available data from 2015 (note that AUTUMNX magnetometers (IQA) record magnetic field variation data with a 1-second rather than half-second cadence). The unfiltered dB/dt search results were manually classified as noise-type or TLA events via the criteria described in Sections 3.5 and 3.6 in order to test the accuracy of the filters.

The results of these search algorithms with and without the filters are presented in Table 3.3. In the MACCS stations, all TLA intervals were retained and a vast majority of noise-type signatures were successfully removed. The filters removed all of the noise-type dB/dt from the IQA station and all but 2 noise-type signatures from the INUK station. It is important to note that at the IQA and INUK stations, the filtered dB/dt search removed two events at each station that were classified as geophysical rather than noise-type, but did not meet the TLA selection criteria of having a dB/dt with timescale of 10-60 seconds and a ΔB of at least 60 nT. These were the only events that were removed via the filters that were not classified as noise-type events nor TLA events; these four

events make up six signatures total comprising just 1% of the total geophysical signatures (i.e., total of the "# TLA dB/dt unfiltered & filtered" in Table 3.3) from all eight stations in 2015.

The filtered dB/dt set contains all of the same TLA-type dB/dt signatures as prior to the filters, however there are significantly less noise-type intervals after being filtered. The ΔB, Δt and dB/dt values of the intervals in the filtered data set are much more similar between TLA and noise-type, however the noise-type events still exhibit many more signatures in general, and many more with the smallest Δt and ΔB values from 2-10 s and 6-100 nT (2134 noise-type intervals compared to 20 TLA intervals). The distribution of dB/dt values after the filters has many noise-type signatures with large dB/dt values that only few TLA signatures have (over 500 noise-type intervals have dB/dt value from 20-100 nT/s compared to 2 TLA intervals), although it is still very possible for TLA signatures to have dB/dt intervals in this range from 20-100 nT/s.

The filtered dB/dt signatures have greatly narrowed dB, dt and dB/dt characteristics. The number of dB/dt signatures per noise-type and TLA event is also much more similar in the post-filtered data set. Prior to the filters, the average number of dB/dt signatures per noise-type hour event window (for the six MACCS station used for the noise characterization in section 3.5) was over 150 dB/dt, and after the filters, this average for the same six stations is just over 10 dB/dt intervals. Overall, the filters greatly reduced the total number of noise-type dB/dt but also narrowed the noise-type dB/dt to just those that are most similar to TLA events. However, it can be seen from Table 3.3 that there is still a large number of noise-type dB/dt in the filtered dB/dt set.

What remains after the filters are noise-type and TLA signatures that are most similar in their amplitude and timescale characteristics, as well as the total number of dB/dt intervals within an hour event window. The data in Table 3.3 shows that the specific selection criteria imposed on the TLA dB/dt search algorithm greatly improved the efficiency of the results, removing over 99% of the noise-type dB/dt while retaining all TLA intervals that meet the formal definition of TLA events described in this section and excluding only four geophysical events that did not meet the criteria for a TLA event.

3.7 Support Vector Machine Classification of Noise-Type and TLA dB/dt

While the filters described in section 3.6 improved the accuracy of the dB/dt search algorithm, there were still thousands of noise-type dB/dt (mostly found in the more commonly noisy stations IGL and CDR) which required further separation from the TLA dB/dt. Because the noise-type and TLA dB/dt intervals have very similar statistical characteristics after being filtered, they cannot be further separated with a linear approach and a more complex method of distinguishing the intervals

is needed. As a final measure of separation, we implemented a machine learning classification technique to classify the dB/dt intervals returned from the filtered algorithm as TLA or noise-type. The primary goal with a machine learning classifier was to identify and remove as many noise-type dB/dt as possible while retaining as many TLA-type dB/dt as possible.

The classifier used to identify TLA and noise-type dB/dt from the data set is called a support vector machine (SVM). In recent works, the SVM has been utilized for various space weather applications (e.g., prediction of solar flares using magnetic field data (Bobra and Couvidat, 2015) and prediction of high-latitude ionospheric scintillation with multiple types of solar wind and geomagnetic field data (McGranaghan et al., 2018)). This classifier was tuned and trained using all of the post-filter dB/dt signatures from 2015 and all eight stations (i.e., all of the dB/dt in the post-filter column of Table 3.3). The features used to tune and train the model are the dB, dt and dB/dt (values scaled to between 0-1), the geomagnetic latitude of the station represented as a fraction of 90 degrees, the time represented as a day fraction, and the day of year represented as a year fraction of 365 days (while also accounting for leap years). Thus, all of these features are scaled so that all values are between zero and one.

An SVM is a supervised machine learning technique often used for binary classification (Cortes and Vapnik, 1995). The objective of an SVM is to classify samples by determining the optimal hyperplane- or decision boundary- to separate the samples within the feature space (Suthaharan, 2016). The feature space for a training data set is the N-dimensional vector space that contains all of the feature values of the training set. The optimal hyperplane is determined by maximizing the space from the decision boundary to the nearest data points- or support vectors- in the feature space. If a data set is not linearly separable within the feature space (as in the case of the 2015 dB/dt set), the features are transformed into a higher-dimensional feature space where a linear hyperplane can be derived as decision boundary between classes. This transformation of the features to a higher dimensional space is performed using a kernel function.

The SVM used to classify dB/dt intervals in this study is from the scikit-learn library and uses the radial basis function (RBF) kernel (Pedregosa et al., 2011). The hyper-parameter C is used in the SVM model that introduces a penalty for incorrectly classified samples, the severity of the penalty determined by how large the scalar C is. A large value for C means a higher consequence for misclassified samples, this results in a decision boundary with smaller margins and can lead to overfitting of the training data. A C value that is too low results in very large margins and, in turn, more misclassified samples. The RBF kernel function also uses the hyper-parameter gamma, γ, that defines how much influence a single training example has. A small value of γ means that the similarity radius of each training point is larger and thus more points can be grouped together in the feature space, whereas a large value of γ means that the data points have to be much closer to one another in the feature space in order to be grouped together in the classification. Further

discussion of the tuning process and the hyper-parameter selection for the SVM can be found in Appendix B.1.2 and B.1.3.

In the tuning and testing process, we used three main metrics to evaluate the performance of the SVM model: accuracy score, Probability Of Detection (POD) score, and Heidke skill score (HSS). The accuracy score represents the number of correct classifications (both TLA and noise-type) divided by the total number of predictions. Often the accuracy score does not best represent the performance of the model, so more complex metrics are utilized.

The latter two metrics are based on the model evalution guidelines of Liemohn et al. (2018) and they use the outcomes of the predictions made by the model in the tuning and testing process: H (hits i.e., correct classifications of TLA events), M (misses i.e., TLA events incorrectly classified as noise-type), F (false alarms i.e., noise-type events incorrectly classified as TLA events) and N (correct negatives i.e., noise-type events correctly classified as noise-type events). These metrics make up the contingency table for the model and are also commonly referred to as true positives, false negatives, false positives, and true negatives, respectively. The POD score gives a more specific evaluation of how well the model performs at classifying TLA events, it is given by Eq. (9) of Liemohn et al. (2018):

$$POD = \frac{H}{H + M} \tag{3.1}$$

The POD score is a useful metric here because our purpose is to retain as many TLA events as possible. It ranges between 0 and 1 with higher values being better scores. The Heidke skill score (Heidke, 1926) represents all of the values in the contingency table and gives an evaluation of how well the model performs while excluding the classifications made by random chance (Eq (8) of Liemohn et al. (2018)):

$$HSS = \frac{2[(H \cdot N) - (M \cdot F)]}{[(H + M)(M + N) + (H + F)(F + N)]} \tag{3.2}$$

The HSS is highest at a value of 1 if the model perfectly classifies all of the hits and correct negatives and can result in a negative value if the model has no ability to classify TLA events.

In order to determine the optimal values for γ and C, the SVM model was cross-validated by first splitting the 2015 dB/dt data set into ten separate sets- or "stratified cross-folds"- with equal proportion of each type of sample (TLA and noise-type, of these sets may contain overlapping samples). Then each of these ten folds is split into training (80%) and testing (20%) sets and 49 SVMs are trained and tested for each of these ten data folds. Each of the 49 SVMs have a different combination of seven γ values (from 0.0001-100 in multiples of ten) and seven C values (from 0.001-1000 in multiples of ten). Thus, 49 combinations of γ and C were used to train SVMs on each of 10 separate folds of data for a total of 490 fits to the model. The SVM that has the

highest accuracy and POD score averaged across all ten test folds is chosen to have the optimal hyper-parameters.

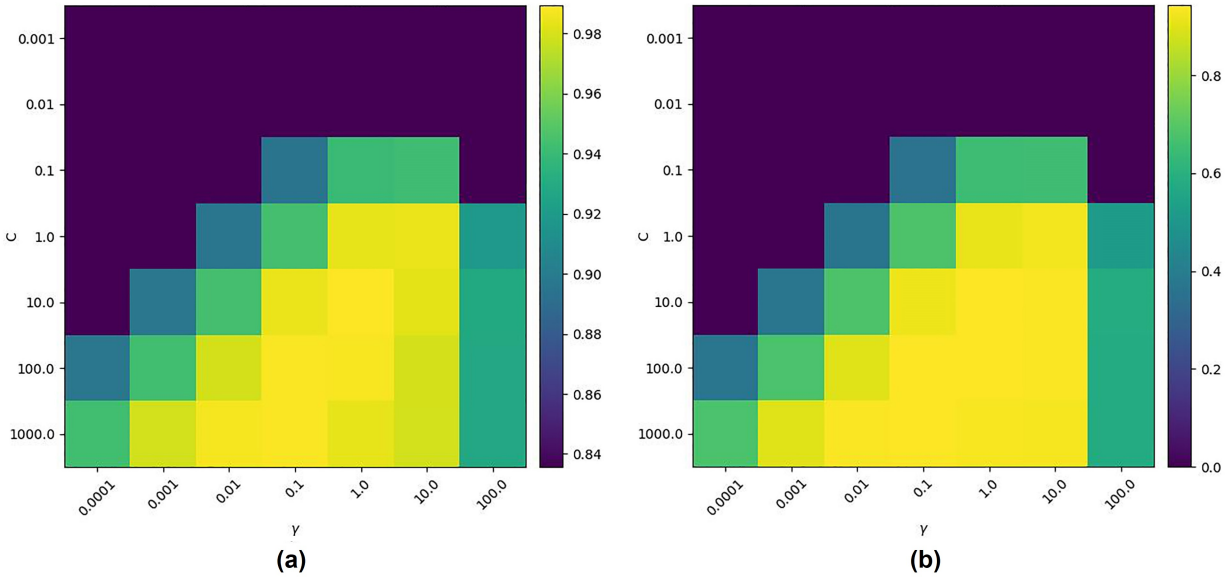

Figure 3.8: (a): Cross-validation grid showing the average accuracy score as the color of each square for each C and γ value for all 49 folds in the tuning process. (b): Same cross-validation grid as in (a) but for the average POD score for all 49 folds. Note that color bars are different for (a) and (b).

The results of the cross-validation process are shown in Figure 3.8: two grids showing the average accuracy and average POD of the ten folds for each C and γ value. In both cases, the hyper-parameters in the SVM that scored the highest average accuracy (0.989) and POD (0.944) scores across the ten folds of training data are $\gamma = 1$ and C = 10.

After the optimal values for γ and C were determined, these hyper-parameters were used to train the final SVM using all of the 2015 dB/dt data. In order to test the model performance, the initial, unfiltered dB/dt search as well as the filtered dB/dt search were performed on all of the same eight stations but for the year of 2016. All dB/dt identified from 2016 were manually classified as noise-type or TLA based on the criteria described in sections 3.4 and 3.5 (i.e., comparison of shapes and amplitudes of the perturbations with those described in Khomutov et al. (2017) and statistical characteristics of events at MACCS stations in 2015) in order to assess the accuracy of the model predictions. The filtered dB/dt search was successful in removing a majority of noise-type dB/dt intervals while retaining all of the TLA signatures. Then the SVM classification was performed on the filtered dB/dt intervals.

The SVM model was chosen because it exhibited the best classification accuracy and POD scores out of four supervised machine learning classification algorithms. The details of the other

three algorithms and their scores are provided in Appendix B.1.2. Table 3.4 lists the number of TLA and noise-type dB/dt returned from the unfiltered and filtered dB/dt search for the year of 2016 as well as the results from the SVM classification. Because the classification is performed on individual dB/dt intervals and many events consist of multiple dB/dt grouped within a 1-hour window, the dB/dt label predictions are grouped if they occur within a 1-hour event window of one another and the final SVM classification of all the dB/dt intervals in the event window is the majority vote of the predictions. If there are an equal number of dB/dt classified as noise-type and TLA within an event window, all dB/dt are labeled as geophysical TLA in order to reduce the number of TLA events removed by the SVM classification.

Station	# Noise-type unfiltered dB/dt	# Noise-type filtered dB/dt	# TLA dB/dt unfiltered & filtered	# Noise-type post-SVM dB/dt	# TLA post-SVM dB/dt	
IGL	131526	5126	13	7	12	
GJO	3078	1	10	0	5	
RBY	192525	249	37	0	32	
PGG	3695	351	23	5	23	
CDR	410	61	53	8	53	
NAN	211736	0	2	0	2	
INUK	7	2	194	2	194	
IQA	182	121	106	0	89	
	Total unfiltered	Total SVM-classified	# Correct noise-type	# Incorrect noise-type	# Incorrect TLA	# Correct TLA
dB/dt:	543597	6349	5889	22	28	410
Hour events:	3010	464	319	8	8	129

Table 3.4: Table with number of dB/dt signatures of both TLA and noise-type returned from the unfiltered and filtered dB/dt search algorithm and after the SVM classification

Table 3.4 shows that there were a total of 543,597 high-frequency dB/dt intervals identified in the 2016 data. These events were manually separated via the criteria described in section 3.4 to obtain a total of 543,159 noise-type dB/dt and 438 TLA dB/dt. After imposing the filters described in section 3.6, just 6349 intervals remain including 5911 noise-type and the same 438 TLA type (the manual classification found no geophysical events that did not meet the criteria for a TLA event). The filtered dB/dt intervals are those that go on to be classified with the SVM.

From the filtered dB/dt search, there are 5911 noise-type dB/dt signatures making up 327 event hours and 438 TLA dB/dt signatures making up 137 event hours. At the bottom of Table 3.4 are the number of dB/dt for each prediction type of the SVM classification. Out of 6349 total dB/dt signatures from the filtered dB/dt search for these eight stations throughout 2016, there are a total

of 6299 correct predictions (i.e., H, "hits") resulting in an accuracy score for individual dB/dt signatures of 0.9923. Further, for the individual dB/dt interval SVM classifications, the POD score is 0.9361 and the HSS is 0.9383.

The dB/dt set returned from the full automated process of filtered dB/dt search with SVM majority-vote classification consists of 410 TLA dB/dt signatures making up 130 TLA hour-events and 22 noise-type dB/dt signatures making up 8 hour-events. In addition to the individual dB/dt predictions, Table 3.4 also includes the SVM prediction results of the hour-event windows. Out of the initial 464 event hours, 448 were classified correctly as having either TLA or noise-type dB/dt within, for an SVM classification accuracy score of full-hour event windows of 0.9655, POD score of 0.9416 and HSS of 0.9171.

There are 22 incorrectly classified noise-type dB/dt signatures (making up 8 separate hour-event windows) that remain in the final data set and 28 incorrectly classified TLA-type dB/dt signatures (making up 8 event-windows) that are removed from the final data set after the SVM classification. All of the noise-type events mislabeled as TLA events consist of 1, 2 or 3 dB/dt in each component of the field that are part of a spike lasting less than 5 minutes; the average Δt and ΔB of the incorrectly classified noise-type intervals is longer and larger than that of the correctly classified noise-type intervals. The TLA events mislabeled as noise also have few dB/dt signatures (6 of 8 have less than 5 dB/dt signatures total) and all occur within a negative bay that lasts 20 minutes or more. The average Δt and dB/dt of the missed TLA events are similar to that of the correctly classified, however the average ΔB for the missed TLA intervals is about 40 nT smaller than that of the correctly classified TLA events. These details suggest that the most difficult events to distinguish are those with very few dB/dt intervals within the hour window: often spikes with longer than average timescale and amplitude, or TLA events with smaller than average amplitude. Because there are still eight hour events with noise-type dB/dt in the final dB/dt set, the final step of this complete dB/dt search process requires that the signatures are still plotted and the TLA-type events manually confirmed. However, the results of the full process in Table 3.4 show that the final dB/dt set is significantly narrowed to a majority of TLA-type events and only a few noise-type events.

The test scores of the SVM classifier on the filtered dB/dt intervals have all been presented above and show that the majority-vote SVM classification performs very well at identifying high-frequency disturbance events and classifying them as noise-type or geophysical.

In addition to providing the characteristics of the individual dB/dt signatures that meet the TLA event filter criteria and the SVM classification, the complete automated process provides a complete high-frequency disturbance event list for a magnetic field data set. The high-frequency event flagging process identifies all hour event windows that have any high-frequency dB/dt (defined as a dB/dt interval with 1-60 second timescale, dB/dt $>$ 6 nT/s and subsequent minimum ΔB of 6 nT)

and initially classifies the hour as a noise-type event. Then, if the requirements are met for these dB/dt to be a potential geophysical TLA event (i.e., the filter criteria: at least one dB/dt interval lasting more than 10 seconds and ratio of high-frequency dB/dt to all dB/dt within the hour being less than 0.05), the SVM majority-vote classification is performed. If the SVM classifies a majority of the high-frequency dB/dt as geophysical, then the classification of the hour window is changed to geophysical event rather than noise-type event. The resulting list is compiled of all of the hour event windows within a data set that contain high-frequency perturbations and includes the SVM majority-vote classification of the hour event as a zero if the dB/dt signatures are determined to be noise-type and a one if they are determined to be of geophysical nature. Thus, the complete high-frequency geomagnetic disturbance classifier can be used to retrieve information on the individual TLA dB/dt signatures as well as to identify hour event windows in the data that contain high-frequency signals and determine the geophysical or noise-type nature of those signals with high accuracy.

To concisely illustrate the performance of the fully automated geomagnetic disturbance classifier (initial dB/dt search, filters, and SVM classification), the contingency matrix for the 2016 test data is shown in Figure 3.9. This contingency matrix shows the four types of classification (H, F, M, N) for the entire set of high-frequency dB/dt intervals identified in the 2016 test data. The statistics in this Figure 3.9 are compiled from the Table 3.4 and show more clearly how well the complete process performs at identifying all second-timescale, high-frequency dB/dt intervals and classifying them as noise-type or geophysical TLA events. The test results for the full data set are listed below the contingency matrix. The accuracy score is quite high, but represents some possibility of correct classifications by random chance because there is such a larger proportion of noise-type dB/dt and event hours compared to TLA. The POD and HSS scores are more indicative of the actual performance of the automated process. The POD and HSS scores are all near 0.94 an show that the fully automated geomagnetic disturbance classifier performs quite well.

This automated high-frequency geomagnetic disturbance classifier can be implemented on large-scale magnetic field databases. As a usable research artifact, we have provided the high-frequency event lists for the six MACCS stations used in this study for the year of 2017 to our data repository (doi.org/10.7302/78zf-yw59). From these lists, we can identify that at the CDR station, 30 of the 104 GMDs that occurred during 2017 (of Engebretson et al. (2019a)) had TLA high-frequency variations associated to them and these are among the largest GMDs that occurred that year ($>$ 10 nT/s). With these event lists, we can cross-reference these events with those from the other stations to identify what other stations to compare the spatial scales and relative strengths of these perturbations in this region which can help identify the M-I phenomena involved. Further, these event lists enable to us to avoid the hours of data that are highly likely to be contaminated with noise-type dB/dt events.

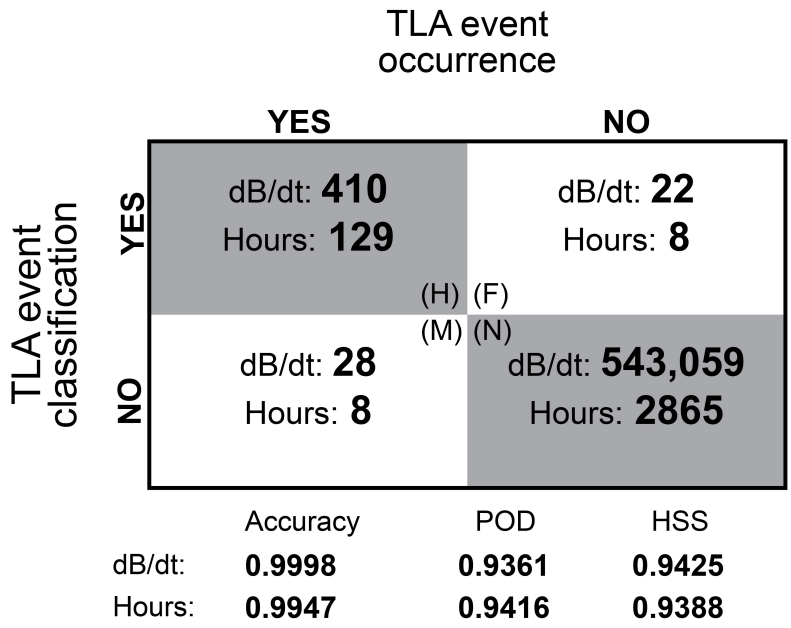

	Accuracy	POD	HSS
dB/dt:	**0.9998**	**0.9361**	**0.9425**
Hours:	**0.9947**	**0.9416**	**0.9388**

Figure 3.9: Contingency matrix and test scores for fully automated geomagnetic disturbance classifier performing on the 2016 test data.

3.8 Effect of Data Processing on High-Frequency Geomagnetic Signatures

We have identified both noise-type and geophysical TLA signals in raw data from MACCS, AUTUMNX and CANMOS magnetic field data as well as processed data from SuperMAG. While further data processing measures like averaging the data over 1-minute- or even 1-second- or using a band-pass filter may remove these signatures altogether, these techniques could also remove TLA signatures that are necessary for the study of small-scale M-I currents.

To briefly examine the effect of a common data processing and resampling procedure on high-frequency signals, we compared dB/dt signatures identified from raw, unprocessed MACCS data with those identified from processed data from the SuperMAG data service for two separate events that occurred at the PGG station in 2015. SuperMAG collects data from contributors (MACCS, AUTUMNX and CANMOS included) and processes it uniformly with the procedure described in Gjerloev (2012). SuperMAG offers 1-second averaged magnetic field data that has undergone the data cleaning (automated and manual) and baseline removal process: separation of the background magnetic field from sources in the M-I system by determining both the yearly trend and diurnal variations of the magnetic field (Gjerloev, 2012), as well as resampling the 2 Hz data to 1 Hz.

The MACCS, AUTUMNX and CANMOS magnetometer stations are all part of the SuperMAG network, so it is convenient to compare raw data from MACCS with processed data from Super-

MAG for the same events. The filtered dB/dt search was conducted on both the raw MACCS data and the processed data from SuperMAG for two events at PGG during 2015. One of these events is the bay-like noise-type event that occurred on 20 June 2015, this event is shown in the unprocessed MACCS data in Figure 3.5 and in the processed SuperMAG data in Figure 3.10. The other event is a TLA event on 10 November 2015, shown in Figure 3.6.

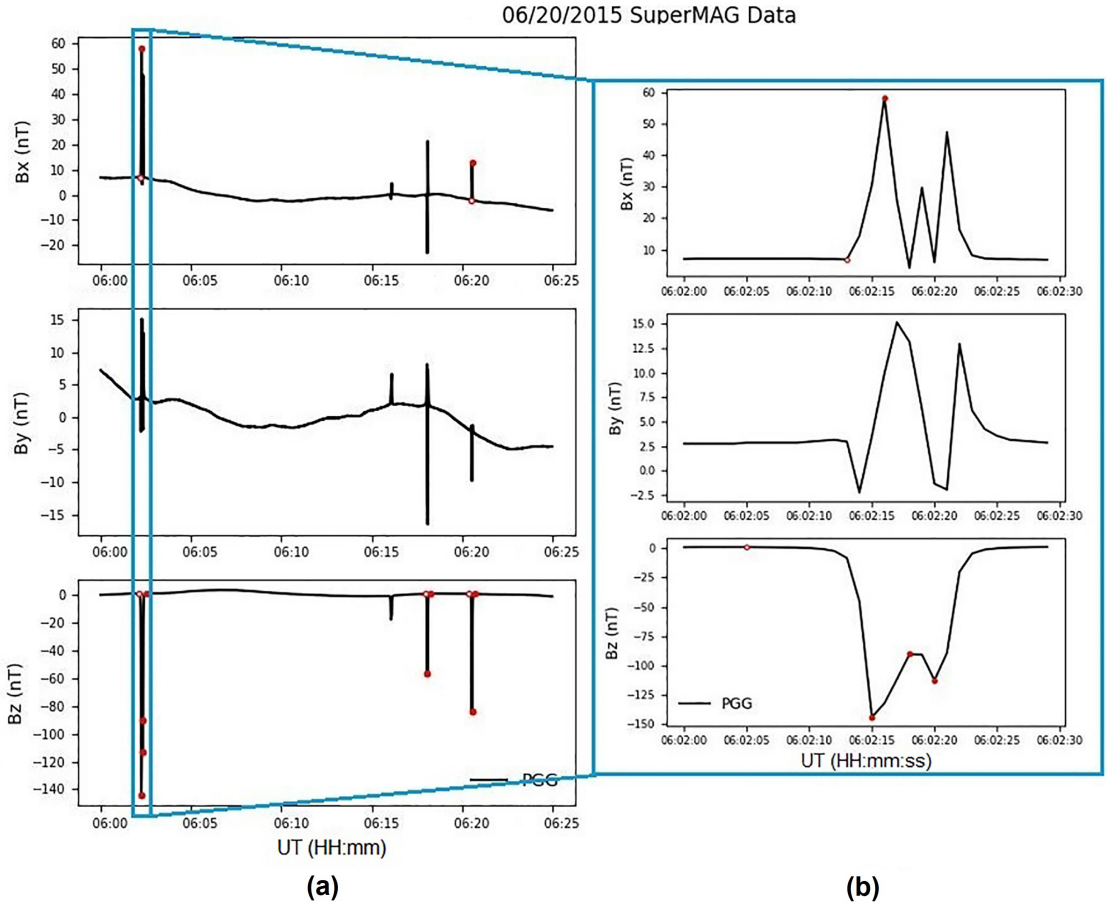

Figure 3.10: Bay-like noise in MACCS magnetic field data that has been processed with the SuperMAG data processing technique. The event occurred on 20, June 2015 at the PGG station. Hollow circles mark the start of a dB/dt signature and solid dots mark the end. The mean B value of each component in the interval shown is subtracted from the data (Note that this mean B value is different than that subtracted from the raw data in Figure 3.5 because all of the values are altered in the SuperMAG data processing.

With the unprocessed MACCS data, the noise-type event on 20 June exhibited 17 high-frequency dB/dt signatures among the four disturbances within the hour. These dB/dt signatures have an average ΔB of 69.8 nT, average Δt of 6.2 seconds, and average dB/dt of 13.1 nT/s. With the processed SuperMAG data (1-second averaged, cleaned and baseline removed) there are just 10 dB/dt signatures that have average ΔB, Δt and dB/dt of 68.7 nT, 6.9 seconds and 11.1 nT/s,

respectively. Figure 3.10a shows that all four of the noise shapes are still present in the processed data, however there are less dB/dt signatures that meet the criteria for a high-frequency disturbance (second-timescale, dB/dt >6 nT/s and ΔB $>$ 60 nT). Further, the zoomed view of the bay-like disturbance in Figure 3.10 shows that the processed data removes some of the high-frequency behavior between the leading and trailing edges of the bay in all three components, but some of the high-frequency dB/dt signatures are still present.

The TLA event on 10 November 2015 at the PGG station exhibited 12 dB/dt signatures in the unprocessed MACCS data (shown in Figure 3.6) and 9 dB/dt signatures in the processed SuperMAG data. This event, like the noise-type event on 20 June 2015, had slightly lower average ΔB (273 nT) and dB/dt (7.6 nT/s) but slightly longer average dt (34.7 s) in the cleaned and processed SuperMAG data. In both noise-type and TLA events, the processed data from SuperMAG exhibits fewer high-frequency dB/dt signatures overall, however in both cases some of these intervals are still present.

This comparative analysis shows that the SuperMAG data processing technique can reduce the amplitude of and even remove some high-frequency dB/dt signatures, but it does not remove the high-frequency noise-type events altogether. The same effect is observed for TLA events. Therefore, it is necessary to implement the automated high-frequency geomagnetic disturbance classifier on unprocessed data to identify intervals where high-frequency disturbances are present and classify them as noise-type or geophysical.

3.9 Conclusions

In this chapter, we have outlined a basic dB/dt search algorithm and detailed the characteristics of the TLA and noise-type dB/dt identified by performing the search algorithm on data from six stations of the MACCS array during 2015. Then, we discussed the filters that were implemented to improve the dB/dt search process based on the characterization of the manually identified noise-type and TLA events and the SVM majority-vote classification of noise-type and TLA dB/dt signatures. Finally, we present an automated high-frequency geomagnetic disturbance classifier for magnetic field data.

The high-frequency geomagnetic disturbance classifier is a new technique that identifies intervals of unprocessed magnetic field data with 1-second or higher temporal resolution that contain high-frequency signals and determines if they are a result of noise or geophysical sources. The full dB/dt search process can identify these event windows and determine the correct source (noise-type or geophysical) with over 96% accuracy.

Because we found that both noise-type and geophysical high-frequency events are present in processed 1-second SuperMAG data, it is recommended that the SuperMAG data processing

method incorporate this automated high-frequency event classifier on the raw, unprocessed magnetic field data and include this list of hour events containing high-frequency intervals and their classifications in the database. This list indicates windows of data that are likely contaminated with noise and undesirable for use in official space weather research, and identifies windows of data that contain high-frequency signals that are likely due to geophysical sources. The detailed information on these dB/dt intervals allows for analysis on the high-frequency behavior of space weather events and small-scale M-I currents.

CHAPTER 4

Magnetosphere-Ionosphere Drivers of Transient-Large-Amplitude Geomagnetic Disturbances: Statistical Analysis and Event Study

This chapter presents a comprehensive analysis of a large database of TLA events. This research was submitted to AGU's Journal of Geophysical Research: Space Physics on April 12, 2023. The database of TLA events used in this study as well as the ASI movie file titled "thg_asi_mosaic_201609300100kuuj.mpeg" is available on the University of Michigan Deep Blue Data Repository (doi.org/10.7302/9par-f788). The GMD event data used in this study are also available on UM Deep Blue (doi.org/10.7302/275e-da06).

4.1 Introduction

Extreme space weather events like geomagnetic storms and substorms can drive large geomagnetically induced currents (GIC) through conductors on Earth's surface. GICs pose a significant threat to technological infrastructure as they can result in costly equipment damage and power outages (Boteler et al., 1998; Pulkkinen et al., 2017). For decades, GICs have been studied with various methods in order to forecast their occurrence and mitigate their consequences. From Faraday's law of induction, the induced currents on the ground are directly related to large changes of the surface geomagnetic field, and thus the magnetic field changes- dB/dt- are often studied as proxy for GICs, though it is the surface geoelectric field and ground conductivity structure that determines the size of the GIC.

The largest and longest space weather events are generally considered to pose the greatest threat to technological infrastructure. These events typically cause geomagnetic field disturbances that last from tens of minutes to several hours and have peak derivative amplitudes exceeding 8 nT/s (Kappenman, 2006). However, recent studies have shown that more rapid and localized processes

are also capable of generating GICs (Engebretson et al., 2019a, 2021; Ngwira et al., 2015; Pulkkinen et al., 2015). Case studies of some of these processes were presented by Belakhovsky et al. (2019), and include sudden commencements (SC), dayside traveling convection vortices (TCV), nightside geomagnetic disturbance events (GMD) and irregular Pi 3 pulsations. All of these space weather processes have timescales of 1-10 minutes and frequency range of 1-22 mHz.

Higher-frequency Pi 1 and Pi 2 magnetic pulsations with irregular waveforms and periods of 1-40 and 40-150 s respectively (Jacobs et al., 1964) have long been studied for their role in substorm dynamics. Pi2 waves are commonly associated with the development substorm current wedge (SCW) (Atkinson, 1967; McPherron et al., 1973); the polarizations of Pi2 magnetic pulsations on the ground have been used to identify the location of the SCW (Lester et al., 1983). Pi 1 pulsations have also been observed in association with substorm onsets (Lessard et al., 2006) and have been shown to be caused by local ionospheric enhancements and particle precipitation (Engebretson et al., 1983; Arnoldy et al., 1987).

While type Pi 1-2 magnetic pulsations are clearly associated with substorm processes, disturbances with these frequencies are not generally associated with GIC activity. Magnetic perturbations in the Pi 1-2 frequency range with second-timescales are less studied in the context of GICs as they are incapable of directly driving large currents through conductors on the surface of Earth. However, it has been shown recently that magnetic field perturbations in this frequency range are an important aspect of larger space weather events that can cause GICs.

The study of Chapter 2 (McCuen et al., 2021) found that high-frequency transient-large amplitude (TLA) dB/dt intervals (17-1000 mHz; 1-60 second periods) with derivative amplitude greater than 6 nT/s often occur prior to or within many of the most intense nighttime geomagnetic disturbance events (GMD) that could drive GICs. Nighttime GMDs are large, isolated geomagnetic perturbations with overall amplitudes of hundreds of nanotesla and 5-10 minute periods (Engebretson et al., 2019a). These events are often associated with substorm onsets, but do not require substorm activity to occur (Engebretson et al., 2021).

It is shown in Chapter 2 that TLA dB/dt intervals are often related to nighttime GMDs and auroral substorms, however this relationship is complex. TLA dB/dt with Pi 1-2 pulsation periods are sometimes involved in substorm processes, but do not always occur in close temporal proximity to substorm onsets or geomagnetic storms. While sudden commencements (SC) have been previously thought to be a primary driver for the most rapid and large-amplitude magnetic field perturbations (Kataoka and Ngwira, 2016), there was only one SC related TLA event despite five other SC events that occurred in 2015 while the MACCS stations were located on the dayside. Rather than SCs and large geomagnetic storms, the largest TLA events were most often associated with smaller-scale processes like GMDs and substorms, suggesting that small-scale ionospheric currents are involved in driving these large-amplitude, high-frequency signatures.

These high-frequency TLA magnetic field intervals show a clear relation to other GIC-causing space weather events, however the exact role these variations play within and in association to larger events is yet unknown. The goals of this study are to (1) more broadly understand the behavior of TLA events throughout the solar cycle, (2) more clearly define how high-frequency perturbations behave within larger space weather events, especially nighttime GMDs and (3) determine the small-scale ionospheric currents and space weather phenomena that give rise to these disturbances. We analyze TLA dB/dt events in magnetometer data from multiple arrays that span the high-latitude region of North America and throughout Solar Cycle 24. We discuss these events in the context of other space weather phenomena and suggest possible physical mechanisms for their generation based on the evidence presented.

4.2 Data

The data used in this chapter are from multiple magnetometer arrays. Table 4.1 gives the geographic and corrected geomagnetic (CGM) coordinates for the stations as well as the array each station is a part of; the map shown in Figure 4.1 shows the locations of these stations in CGM coordinates. The details of each array and instrumentation are outlined below.

Station Code	Geographic Latitude	Geographic Longitude	Corrected Geomagnetic Latitude	Corrected Geomagnetic Longitude	Observatory System
IGL	69.3	278.2	77.7	354.9	MACCS
GJO	68.6	264.2	76.9	328.48	MACCS
RBY	66.5	273.8	75.3	347	MACCS
PGG	66.1	294.2	73.3	19.9	MACCS
CDR	64.2	283.4	72.6	2.9	MACCS
SALU	62.2	284.4	70.8	4.0	AUTUMNX
RANK	62.8	267.7	71.8	337.4	CARISMA
YKC	62.48	245.5	68.9	304	CANMOS
FCC	58.8	265.9	67.85	334.9	CANMOS
GILL	56.4	265.3	65.5	334.3	CARISMA
WHIT	61.01	224.8	63.5	281	THEMIS GBO
KJPK	55.3	282.2	62.4	359.9	AUTUMNX
ATHA	54.71	246.7	61.5	308.5	CARISMA
MEA	54.62	246.7	61.44	308.43	CANMOS

Table 4.1: Location coordinates of stations used in this study. The CGM coordinates were calculated using the AACGM-v2 Calculator (available at http://sdnet.thayer.dartmouth.edu/aacgm/aacgm_calc.php#AACGM) for epoch 2014. Note epoch 2014 was used as it is the median year of Solar Cycle 24.

1) The Magnetometer Array for Cusp and Cleft Studies (MACCS) is a system of magnetometers located in north-east Nunavut, Canada from about 65° to 80° geomagnetic latitude (Engebretson et al., 1995). MACCS is operated by Augsburg University and the University of Michigan and is funded by the National Science Foundation (NSF). The MACCS stations contain fluxgate magnetometers with axes aligned with the Earth's magnetic field (H: magnetic north-south, D: east-west, Z: vertical with positive direction downward into Earth). The MACCS magnetometers measure the magnetic field at 8 Hz and then average and record the measurements at 2 Hz (half-second cadence); the measurements are accurate to 0.025 nT.

2) The Canadian Array for Realtime InvestigationS of Magnetic Activity (CARISMA) is a system of ground-based magnetometers located across central Canada (Mann et al., 2008). CARISMA is operated by the University of Alberta as part of the Canadian Geospace Monitoring Program (CGSM) and is funded by the Canadian Space Agency (CSA). Like MACCS, the CARISMA system consists of fluxgate magnetometers that measure the magnetic field at 8 samples/second. The stations used in this chapter offer final data products that are averaged to 2 samples/s and rotated from the geographic coordinates they are originally measured in to local geomagnetic coordinates. These magnetometer systems offer 0.025 nT resolution data.

3) The the CANadian Magnetic Observatory System (CANMOS) (Nikitina et al., 2016) is a ground magnetometer array operated by Natural Resources Canada (NRCan). CANMOS employs fluxgate magnetometers across Canada that sample the magnetic field at 8 Hz, then resamples to 1 Hz after despiking and performing a 9-point rectangular filter. The CANMOS data have 0.01 nT resolution. The data from CANMOS is in geographic coordinates: X (geographic north-south), Y (geographic east-west) and Z (vertical).

4) The Athabasca University Time History of Events and Macroscale Interactions During Substorms (THEMIS) University of California, Los Angeles (UCLA) Magnetometer Network eXtension (AUTUMNX) (Connors et al., 2016) is located in the eastern region of Canada. The AUTUMNX instruments are fluxgate magnetometers provided by UCLA that measure the magnetic field with 0.01 nT resolution at 2 samples/second and in local geomagnetic coordinates.

5) THEMIS Ground-Based Observatory (GBO) systems (Russell et al., 2008) are a part of the larger collaboration of stations that contribute magnetic data to the THEMIS Ground Magnetometer (GMAG) cooperative. THEMIS GBO stations are operated by UCLA, contain UCLA instruments as in (4) and thus have the same resolution, measurement frequency and coordinate system as mentioned above.

4.3 Methodology

A high-frequency TLA event is defined as a 1-hour period at a single station in which there is

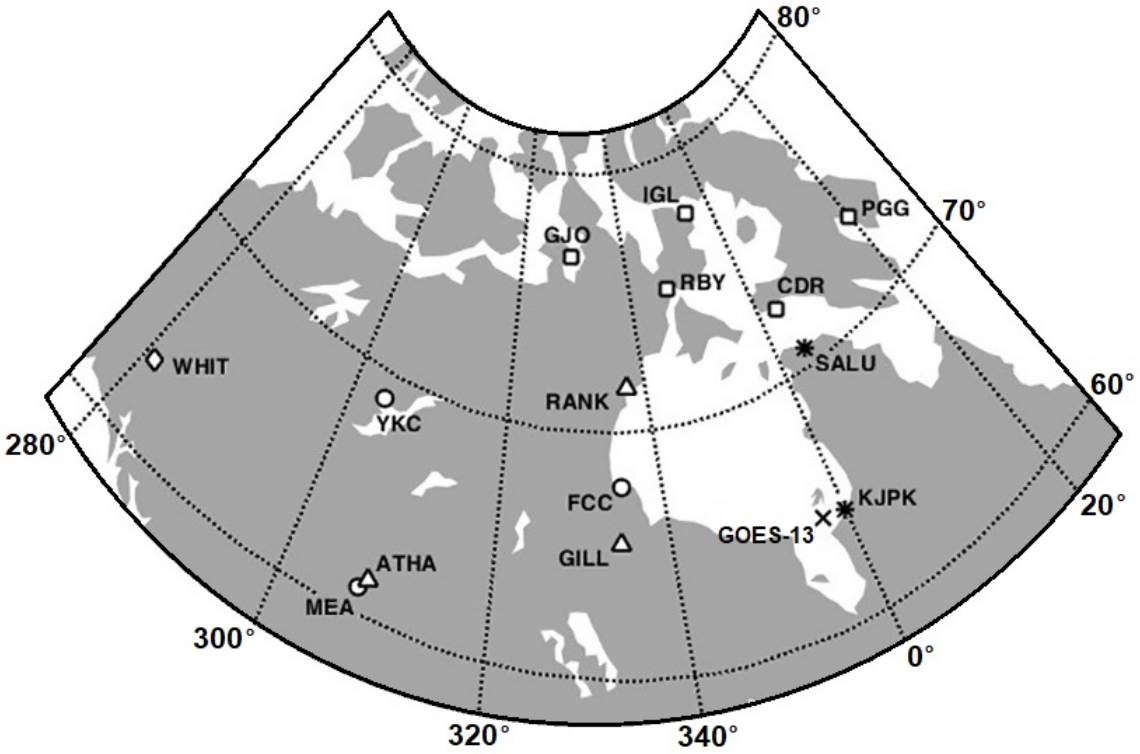

Figure 4.1: Locations of the magnetometer stations used in this study. The symbols for each station represent the array to which they belong: squares signify MACCS stations, triangles signify CARISMA stations, circles are for CANMOS stations, the diamond is for the THEMIS GBO and the asterisks represent AUTUMNX stations. The X marks the magnetic footprint of the GOES-13 spacecraft (determined using tools from SSCWEB https://sscweb.gsfc.nasa.gov/) during the event discussed in Section 6.1. Lines of the latitude and longitude are shown in corrected geomagnetic coordinates for epoch 2014.

at least one dB/dt interval with timescale from 2-60 seconds and magnitude greater than 6 nT/s (subsequent $\Delta B > 60$ nT). The lower derivative amplitude threshold of 6 nT/s was chosen as it is comparable to the 8 nT/s disturbances observed during the geomagnetic storm of March 1989 that caused significant power system damage (Kappenman, 2006). Note that geomagnetic disturbances during storms persist for timescales much longer than 60 seconds, but the 6 nT/s threshold serves as a baseline for what is considered to be large dB/dt.

TLA events often present as clusters of these dB/dt intervals in multiple components of the magnetic field data at a given station. In order to identify instances of TLA events in ground magnetic field data, an automated dB/dt search procedure was designed. The automated procedure is necessary because the characteristics of TLA dB/dt intervals are very similar to that of magnetometer "noise", referred to in this study as signals resulting from outside interference or instrumentation error that do not have geophysical sources. Noise-type signals in magnetometer data

are often very short-timescale and large-amplitude dB/dt intervals, so identifying TLA signatures and distinguishing them from noise-type signals is an imperative aspect of this research.

The automated geomagnetic disturbance classifier is described thoroughly in Chapter 3 and discussed briefly here. The basic algorithm functions by partitioning every hour of data consecutively based on the number of data points and the measurement frequency (i.e., for the 2 Hz MACCS data, the first hour partition is the first 7200 data points and the second hour partition is the following 7200 data points). Then, instances where the sign of the slope of the magnetic field changes and remains the same for at least two measurement cycles (i.e., for 1 consecutive second for 2 Hz data or 2 seconds for 1 Hz data) are identified. The consistency of sign change for two cycles is required to reduce single-point errors/spikes in the data or highly variable data due to noise interference.

After the slope sign changes are identified, the time difference between each slope sign change is calculated (i.e., the Δt between each change of slope direction) as well as the change in magnetic field strength (ΔB), and the rate-of-change of the interval (dB/dt). Finally, this first step of the process identifies all of the intervals between changes of the sign of the slope that last from 1 to 60 seconds and have rate-of-change of at least $|6|$ nT/s.

The next steps of the algorithm incorporate a filtering process that has requirements derived from the statistical analysis of geophysical and noise-type events described in McCuen et al. (2023). The first condition is that at least one dB/dt interval identified from the first step in each hour-window of data lasts 10 seconds or more. This condition is defined because all of the geophysical events identified in the MACCS data for 2015 met this criteria, whereas a large number of hour windows with only noise-type dB/dt exhibited only intervals that lasted less than 10 seconds. If any dB/dt identified in an hour-window lasts more than 10 seconds and has derivative amplitude of at least $|6|$, the ratio filter is performed.

This ratio filter finds the ratio of the number second-timescale dB/dt $>$ 6 nT/s to the total number of dB/dt intervals within the hour (in which the magnetic field changes for at least two measurement cycles, for any timescale and magnitude). If this ratio is less than 5%, then the dB/dt intervals identified in the hour advance to the next step in the process. This condition is implemented because many noise-type events in magnetometer data consist of more than 5% concentration of large, second-timescale dB/dt (hundreds, sometimes thousands of dB/dt within an hour period), so this ratio filter excludes instances that are highly likely to be a result of noise interference rather than geophysical source. The 5% ratio threshold is another requirement derived from the analysis of McCuen et al. (2023).

Finally, if the first two qualifiers are met, (i.e., if there are second-timescale dB/dt $>$ 6 nT/s intervals and at least one interval with 10-60 second timescale, and the 5% ratio filter is passed) then a support vector machine (SVM) classification is performed on the dB/dt intervals to classify them as either geophysical TLA or noise-type. The SVM classification is performed on the

dB/dt intervals within the hour window and the majority vote of these individual classifications is assigned to all of the dB/dt intervals within the hour. Then, if the SVM classifies a majority of the dB/dt intervals as TLA, they are returned as a data product.

4.4 Solar Cycle Dependence of TLA Events

A subset of stations were selected to examine the solar cycle dependence of TLA events. This subset excludes TLA event data from the MACCS stations and consists of events from stations below 63° CGM for epoch 2014 (Table 4.1). These stations were selected because there is more uniform data availability throughout the solar cycle (see Supporting Information Table S1 for yearly data availability).

To explore the occurrence of TLA events in comparison to both sunspots and substorms throughout Solar Cycle 24, we reference Figure 4.2: the number of substorms per day from late 2009 to 2020 (shown in blue) and the number of TLA events per day (shown in black). The number of substorm onsets are from the SuperMAG substorm event list (Newell and Gjerloev, 2011); this method defines substorm onsets as the initial minute in which the SML index drops sharply by 45 nT in the next three minutes and has a sustained negative bay of at least 100 nT over the following half-hour. The SML index is the lower envelope of N-component magnetic field measurements at stations between 40° and 80° magnetic north and reflects the maximum strength of the westward auroral electrojet. This index makes up half of the overall SuperMAG electrojet index, SME, derived by subtracting the SML values from the upper-envelope of N-component values (SMU) from the same set of stations (the SME index is derived using the same concept as the AE index only with many more stations over a larger range from $+40°$ to $+80°$ MLAT). Each of these values were subjected to a rolling 30-day average and then normalized to values between zero and one. The vertical red dashed lines show the times of Solar Minimum and Maximum for Solar Cycle 24 (note that the following Solar Minimum was in April 2020, just beyond the range shown in Figure 4.2). Figure 4.2 shows that the number of TLA events per day generally follows the number of substorms per day, and the number of both events increases during the declining phase of the solar cycle as the number of sunspots decreases.

Next, the association of TLA event occurrences to ring current activity and solar wind speed throughout the solar cycle is examined. Figure 4.3a displays the probability density of all SuperMAG Ring Current Index (SMR) (Newell and Gjerloev, 2012) values for 2009-2019 (shown in red) compared with the SMR values during the minute of the maximum dB/dt interval of each TLA events from 2009-2019. Figure 4.3a shows that SMR values have a narrow distribution that peaks near zero with average value of -6 nT and standard deviation of $\sim$ 15 nT, while the distribution for TLA events is shifted to more negative values, peaking from 0 to -50 nT (mean value of -54 nT)

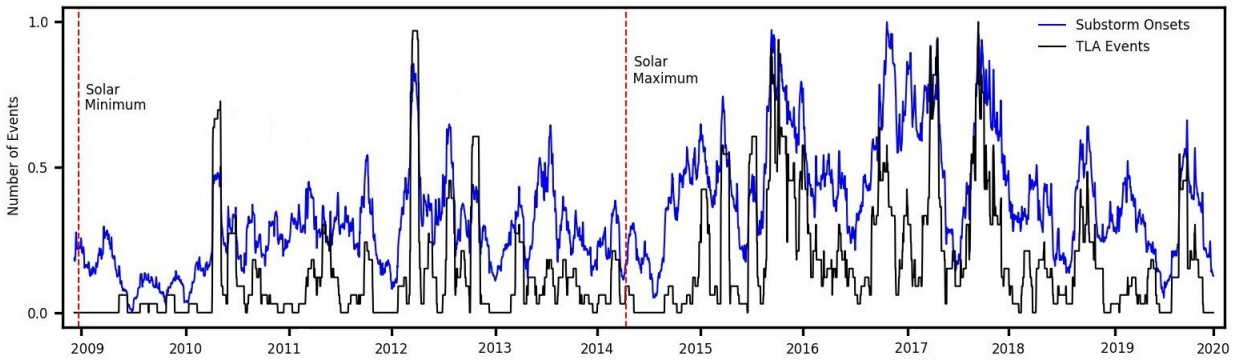

Figure 4.2: Number of substorm events (blue) and TLA events (black) per day from late 2009 to early 2020. Values have been averaged over a moving 30-day period and normalized.

with a larger standard deviation of 43 nT and a long tail that extends to -175 nT. While a majority of TLA events occur for only slightly elevated SMR values, this distribution shows that some TLA events are related to very active geomagnetic storms.

Figure 4.3b shows the probability distribution of all solar wind flow speed values, Vsw, for every minute throughout the solar cycle (red) compared with the solar wind flow speed during the minute of the maximum dB/dt interval during each TLA event (blue). The Vsw values are from the OMNI database (time shifted to the Earth's bow shock nose) (King and Papitashvili, 2020). These distributions show that Vsw peaks between 300-400 km/s, with a mean value of 412 km/s and Vsw during TLA events is much higher on average (mean of 578 km/s) and a majority of values from 450-700 km/s.

Figure 4.2 shows that TLA events occur more often during the declining phase of the solar cycle when substorm activity is increased and large geomagnetic storms driven by coronal mass ejections (CME) occur less often. This observation together with Figures 4.3a and 4.3b that show TLA events are more common during slightly elevated ring current activity and fast solar wind speeds, may indicate that TLA events may be related to weak geomagnetic storms caused by coronal holes and subsequent corotating interation regions (CIR) that are most frequent in the descending phase (Hajra and Sunny, 2022) and give rise to fast flow speeds that can cause mild ring current activations.

4.5 Latitude and Local Time Dependence

In this section, we examine the latitude and magnetic local time dependence (MLT) of TLA events. For these purposes, a subset of the full database of TLA events was created so that there are an equal number of stations used from each magnetic latitude range. This subset consists of TLA events identified in all 12 stations for the years of 2015-2019 only (excluding the two

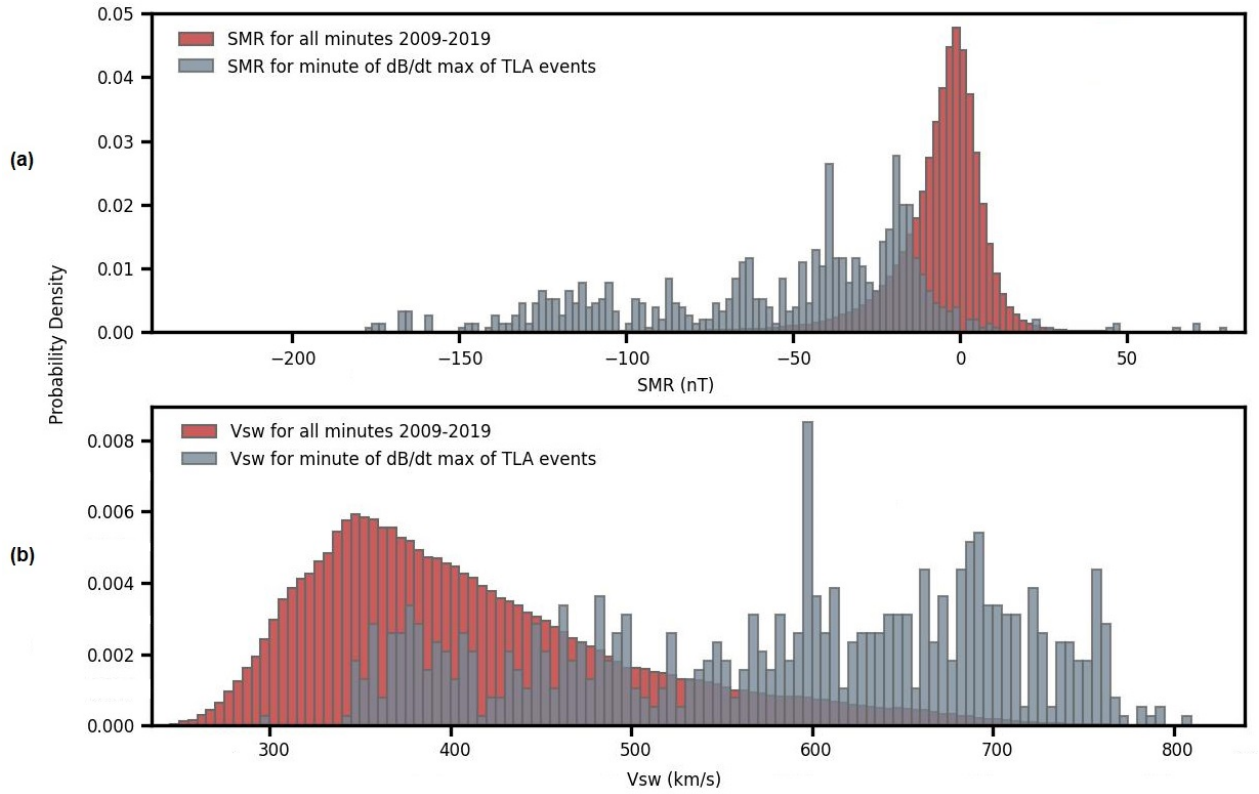

Figure 4.3: Number of the largest TLA events per year separated by the SMR value and the solar wind flow speed during the event.

AUTUMNX stations used in the event analysis of section 6.1, see Supporting Information Table S1). There are three stations in each magnetic latitude range: 61-64°, 65-69°, 71-74° and 75-78°. It is also important to note that we surveyed seven magnetometer stations in the mid-latitude region from 30-60° MLAT and three stations in the equatorial region below 30° MLAT for all years of the solar cycle and we found no geophysical TLA signatures at any magnetic latitudes lower than 60°.

Figure 4.4 shows two distributions of the number of TLA events based on the magnetic latitude at which they occurred (a) and the magnetic local time at which they occurred (b). Figure 4.4a shows that a majority of TLA events occurred in the 65-69° range with a slightly smaller population of events in the 71-74° range. The equatorward boundary of the auroral oval is nominally around 65°; during the expansion phase of substorms the auroral oval can extend to 62–64° and 68–70° in the midnight sector (Akasofu, 1964).

Figure 4.4b shows the local time distribution of TLA events for each hour of MLT. This plot shows that TLA events are primarily nighttime events, with two distinct local time populations. The majority of events occurred from 17-01 MLT and a much smaller number of TLA events occurred from 01-08 MLT. About 3% of the total TLA events from 2015-2019 occurred during the daytime (referred to here as those occurring from 08-17 MLT, outside of the two nighttime popula-

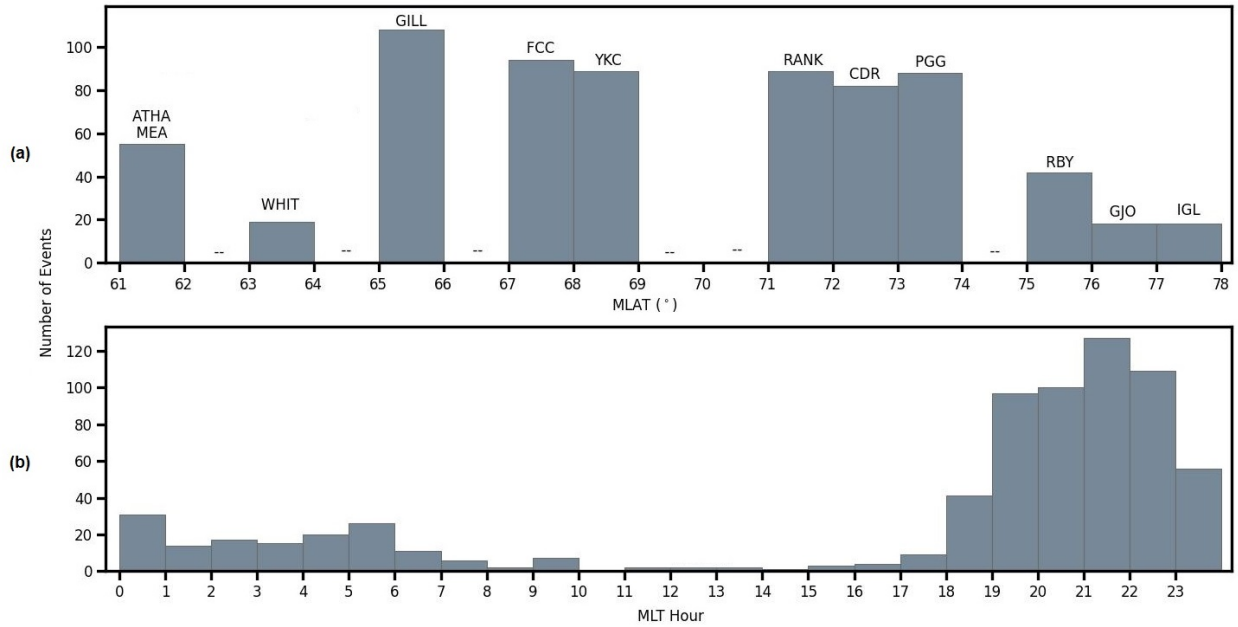

Figure 4.4: Histograms of (a) number of TLA events based on magnetic latitude range and (b) number of TLA events that occurred for every hour of magnetic local time.

tions). Daytime events were most commonly associated with geomagnetic storms (ten events were related to SCs, five occurred during the main phase and two during first day of recovery), however three daytime events are referred to as unrelated events that were not associated to a storm and occurred more than 60 minutes from a substorm onset. Unrelated events, that occurred more than 60 minutes from substorm onset and in the absence of a CME-driven geomagnetic storm, comprised just over 8% of the TLA events that occurred in the 2015-2019 subset. Note that unrelated events in Chapter 2 refers to those that were not associated to nighttime GMDs in addition to storms and substorms; here we refer to unrelated events as those that show no association to storms and substorms but may be related to nighttime GMDs (i.e., this would include the five TLA events related to nighttime GMDs but not storms and/or substorms in Figure 2.3).

4.6 Connection to Substorms and GMD Events

McCuen et al. (2021) analyzed TLA events solely from five MACCS stations for the year of 2015 and showed that they were strongly associated to GMD events. Nighttime GMDs are magnetic perturbations with amplitudes of hundreds of nT and periods of 5-10 minutes (Engebretson et al., 2019a). These events are generally localized to a $\sim$275 km radius and they occur in two distinct local magnetic time populations in the pre- and post-midnight regions (Engebretson et al., 2019b). GMDs are often associated to substorm onsets but substorms are not necessary to cause

them (Engebretson et al., 2021); the pre- and post-midnight populations show different temporal relations to onsets, indicating that there may be distinct M-I drivers for GMDs dependent on MLT.

GMDs have been observed to coincide with dipolarizations in the magnetotail and subsequent auroral streamers (Engebretson et al., 2019b) as well as omega bands (Engebretson et al., 2020). The SECS analysis of nighttime GMDs by Weygand et al. (2021) found that a majority of GMDs occurred underneath the westward electrojet (WEJ); many of the pre-midnight events occurred within the Harang current system while the remaining pre-midnight as well as many of the post-midnight events occurring underneath the downward region 1 or upward region 2 field-aligned current (FAC) systems.

In the present analysis, TLA events are analyzed in comparison with a dataset of GMD events that occurred at the RBY, CDR and PGG stations from 2015-2019 (Engebretson, 2023). In this subset of GMD events, there are 843 hour windows in which GMDs occurred and 236 of them exhibited associated TLA dB/dt intervals. The most extreme GMD events with derivative amplitudes exceeding 12 nT/s occurred within 154 hour windows and of the 154 hour windows of extreme GMD events, a large majority (124 windows, 81%) have TLA dB/dt intervals included within the hour window. For GMDs with derivative amplitudes over 20 nT/s, this percentage is even higher: from 2015-2019, 28 hour windows included GMDs $>$ 20 nT/s and 26 of these windows (93%) included TLA intervals as well.

Of those 124 hour windows with extreme GMDs and associated TLA dB/dt, there are 91 hour windows that consist of GMDs observed at multiple stations; 58 of these windows have the largest TLA dB/dt at the station location of the largest GMD. There are 78 cases of hour windows in which extreme GMDs occur at multiple stations and TLA dB/dt intervals occur at fewer station locations than the GMDs. In other words, TLA events were often even more localized than the spatial extent of the GMDs and further, when the nighttime GMDs commonly occurred at more than one station, the largest TLA dB/dt occurred at the specific location of the largest GMD.

To examine the relationship between substorms, nighttime GMDs and TLA dB/dt events, Figure 4.5 shows the number of TLA and GMD events that occurred from 2015-2019 based on their temporal proximity from the nearest substorm onset (a) and the longitudinal difference of the TLA and GMD events from the location of the substorm onset (b). These substorm onset times and locations are from the SuperMAG substorm event list defined by Newell & Gjerloev (2011). Because TLA events often consist of multiple dB/dt signatures, the time and location of each event is marked with the maximum dB/dt interval of each TLA event. The blue bars in Figure 4.5 show the number of all TLA events, the orange bars show TLA events that were related to GMDs within the same hour window, and the red bars show the number of TLA events related to extreme GMD events ($>$12 nT/s).

Figure 4.5a shows that TLA events most commonly occur within 20 minutes of substorm onset

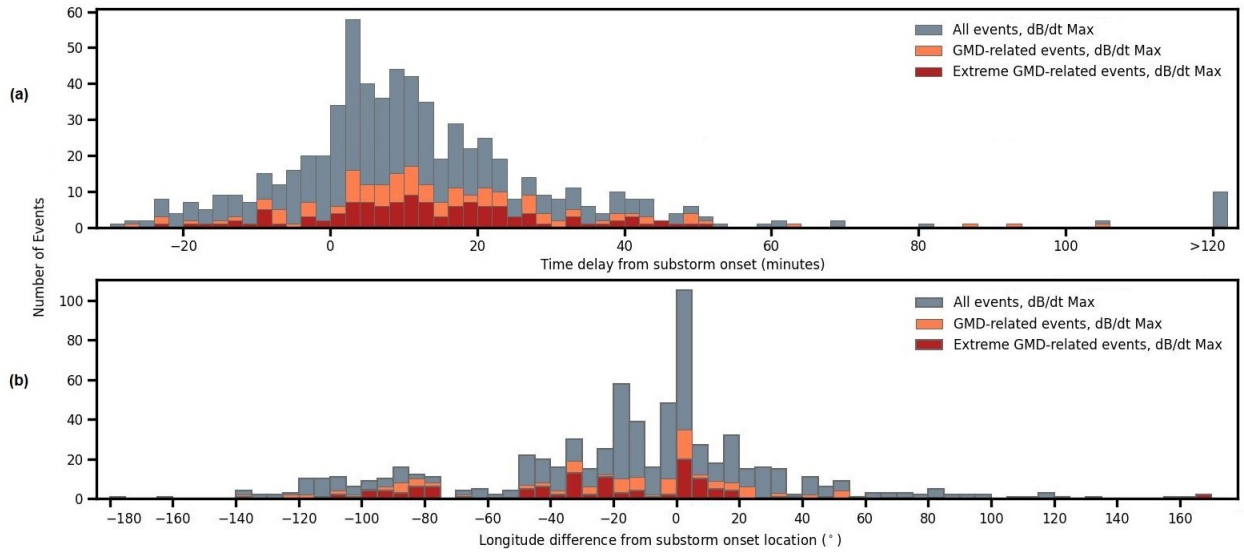

Figure 4.5: Number of 1-hour event windows from 2015-2019 that contain TLA events (blue), TLA events related to GMDs (orange) and TLA events related to extreme GMDs (red) as a function of the time delay from substorm onset (a) and the longitude difference (in geographic coordinates) from where the TLA event occurred to where the substorm onset occurred (b).

with average onset delay of 5.5 minutes. TLA events also occurred in the 30 minutes prior to onset but much less frequently than 30 minutes after onset. The distribution of hour windows containing GMD-related TLA events is much wider than that of the total TLA event population and shows that extreme GMD events with associated TLA intervals comprise about half of all GMD-related TLA events meaning that when GMD events occur with associated TLA dB/dt they are very likely to be the most extreme GMD events. This distribution also shows that hour windows containing extreme GMD events with associated intervals can occur well beyond 20 minutes from the most recent substorm onset, and a sizeable population of TLA intervals occur more than 2 hours from onset.

Figure 4.5b shows the number of hour windows that occurred for a given difference in longitude from the location of substorm onset identified by Newell & Gjerloev (2011) to the location of the maximum dB/dt of TLA events. Here, negative degrees of longitude difference signify that the location of the TLA and/or GMD events within the hour window occurred to the west of the location of the substorm onset. The distance conversion of longitudinal degrees to kilometers ranges from 65 km per 1° longitude at 54° geographic latitude (the geographic latitude of the lowest station) to 38 km per 1° longitude at 70° geographic latitude (geographic latitude of highest station), for an average of about 52 km per 1° longitude over this latitude range.

The distribution of Figure 4.5b shows that most TLA and TLA-related GMD events occurred within $\pm 20°$ longitude of the substorm onset, and more often occur $20°$ to the west of the onset

location rather than to the east. Further, Figure 4.5 shows that many hour windows containing extreme GMD events with associated TLA intervals occur very far from the location of the substorm onset, in many cases more than 80° of longitude west of the onset location. Taken together, these two figures show that a majority of TLA events are closely related to substorm activity, but also shows the distinction that many TLA events, especially those related to extreme GMDs, can have in both time and space from substorm onsets.

4.6.1 Analysis of September 30, 2016 GMD/TLA Events

Figure 4.6 shows GMD events that occurred at six stations on September 30, 2016. The data for each station are plotted from top to bottom in order of decreasing magnetic latitude. Within these GMDs, TLA intervals occurred at the RBY, CDR, and RANK stations, shown as open circles signifying the start of each interval and solid circles as the end. The TLA intervals first occurred at the RANK station from 01:26 to 01:28 UT, at CDR within the 01:33 UT minute, and then at RBY from 01:33 to 01:39 UT. The largest amplitude derivative (-12.29 nT/s) occurred at RBY in the z-component, lasting 44 seconds and spanning the minutes from 01:34-01:35 UT. The GMDs at CDR, RBY and SALU are all among very large events in the GMD database, with derivative amplitudes exceeding 12 nT/s. Figure 4.7 displays a zoomed-in view of the magnetic field data when the TLA dB/dt intervals occurred to show the specific TLA variations.

This event occurred during relatively quiet global geomagnetic conditions (the SMR index ranged from ∼-28 nT to 16 nT during the hour shown). A substorm onset occurred at 01:10 according to the method of Newell & Gjerloev (2011). Substorm auroral onsets are determined by major auroral intensifications (Akasofu, 1964; Nishimura et al., 2010); by this definition a small substorm auroral onset occurred at 01:05 UT and a larger onset occurred at 01:20 UT. The SML index increased ∼160 nT 01:00 to 01:10 UT, then decreased to the minimum value of -785 nT at 01:29 before increasing again to pre-onset values by the end of the hour, but did not show any distinction of the substorm auroral onset at 01:05 UT.

The average solar wind flow speed was 685 km/s and average solar wind dynamic pressure was around 2.4 nPa during this hour, both of which rose slightly at the time of onset (to 708 km/s and 2.8 nPa, respectively) and then returned to varying near the average. The IMF Bz turned southward (decreasing) from 01:05-01:21, 01:23-01:30 and 01:32-01:38 with sharp northward increases in between the intervals, and then increased slowly at 01:38 for the remainder of the hour.

In order to analyze the ionospheric behavior during this interval, the spherical elementary current systems (SECS) method developed by Amm & Viljanen (1999) and applied to magnetometers in North America and Greenland by Weygand et al. (2011) was used to analyze the horizontal equivalent ionospheric currents and the vertical current amplitudes during this interval. The

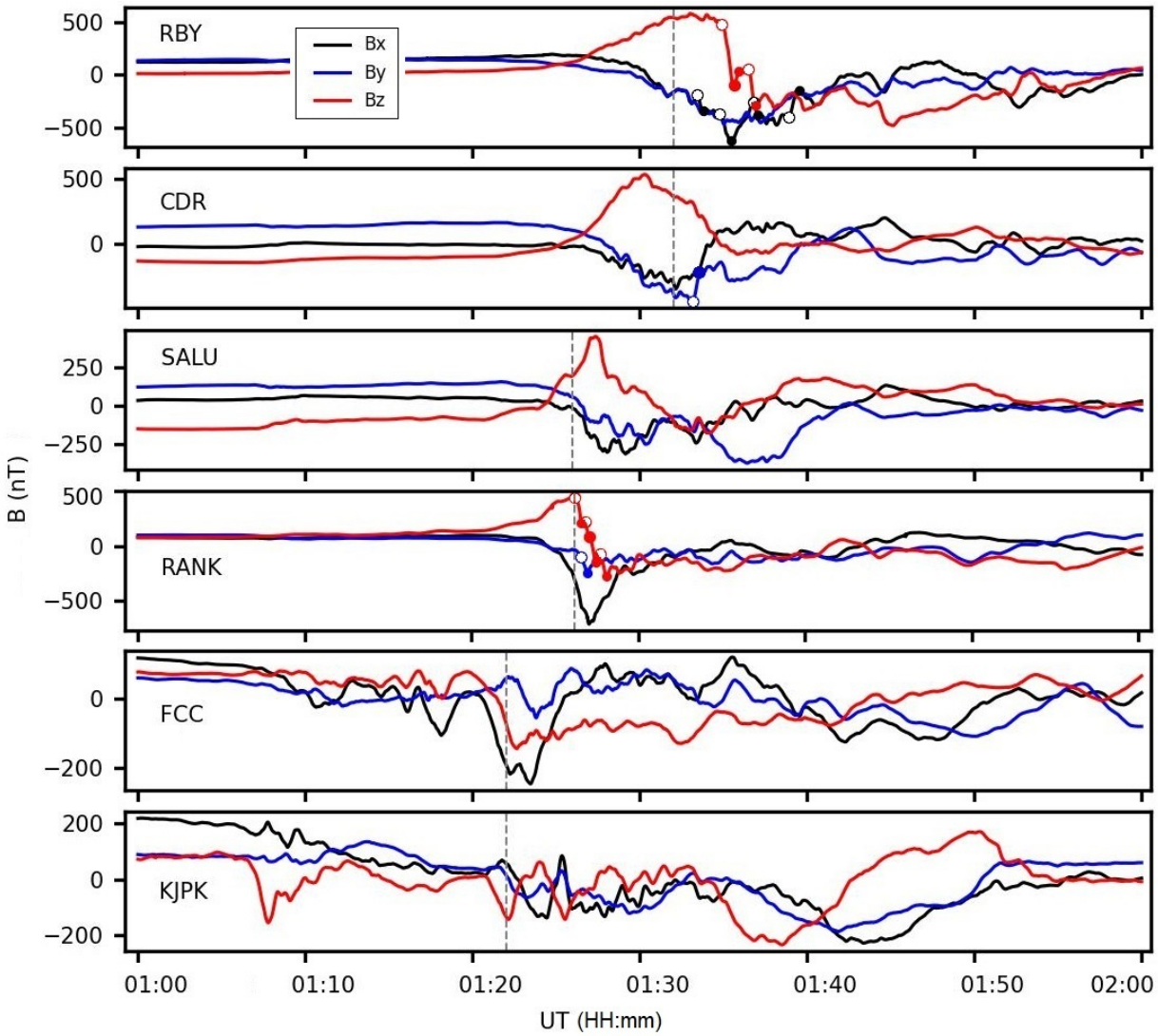

Figure 4.6: Magnetic field data from six stations on September 30, 2016. The Bx component is displayed in black, By in blue and Bz in red. The TLA intervals that occurred within some of the events are signified by hollow circles denoting the start of the interval and filled circles denoting the end of the interval. The dashed vertical lines signify the times that correspond to the SECS maps in Figures 4.8 and 4.9. The mean B value in each component for the interval shown has been subtracted.

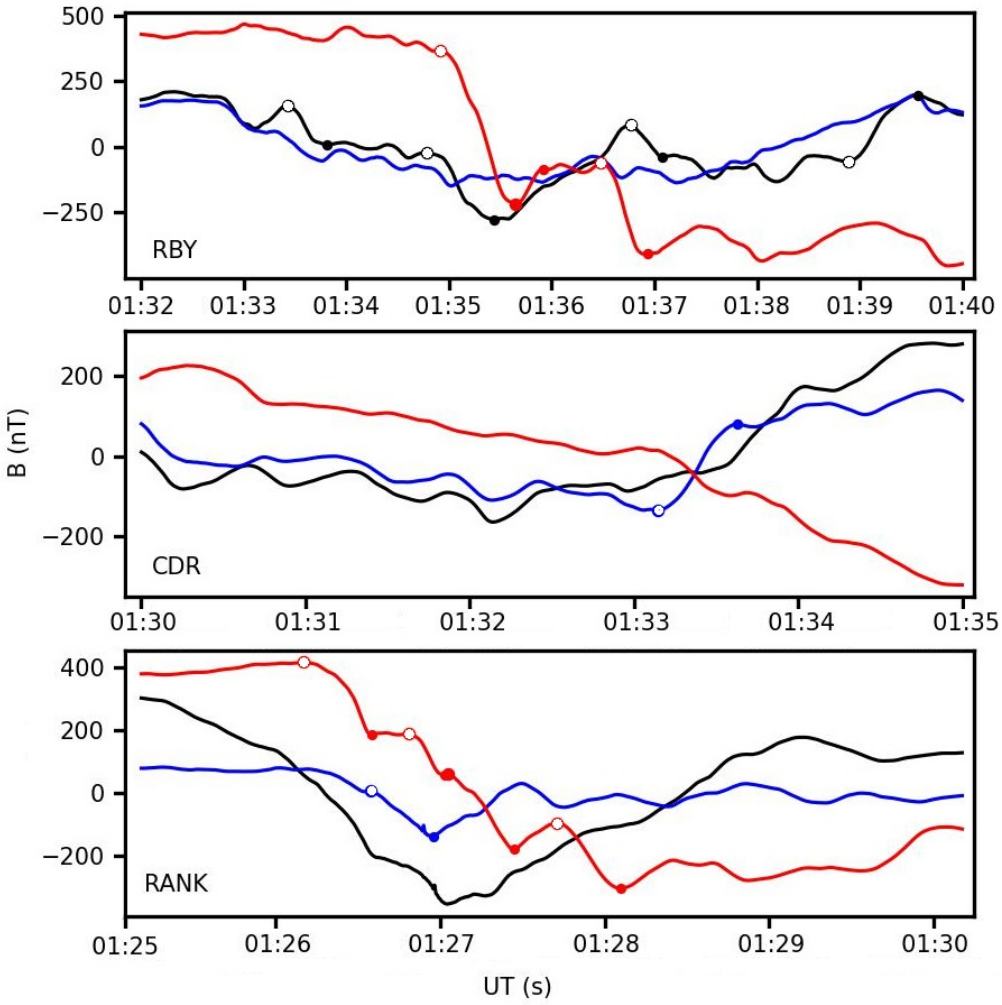

Figure 4.7: Zoomed view of magnetic field data intervals where TLA dB/dt occurred on September 30, 2016. The Bx component is displayed in black, By in blue and Bz in red. The TLA intervals are signified by hollow circles denoting the start of the interval and filled circles denoting the end of the interval.

SECS method calculates equivalent ionospheric currents by expanding the ground magnetic field effects of two spherical elementary current systems: a curl-free system (field-aligned currents) and a divergence-free system (entirely ionospheric currents).

Figure 4.8 and 4.9 display SECS maps for pertinent minutes throughout this event, with the stations in Figure 4.6 marked as colored circles. The red shaded regions indicate locations of upward FAC and the blue shaded regions indicate downward currents, with the degree of shading signifying the strength of the current. Further, the movie of file "thg_asi_mosaic_201609300100kuuj.mpeg" in the data repository for this research (doi.org/10.7302/9par-f788) shows a mosaic composition of images from THEMIS All-Sky Imagers (ASI) at four stations in this region for the hour interval in which this event occurs.

The two southern-most stations, FCC and KJPK, measured slight disturbances near the time of the substorm onset ∼01:10 UT. The SECS map at 01:10-01:11 UT (not shown) indicate a slight and localized intensification of the upward current and mild south-eastward horizontal currents above the FCC and GILL stations. At 01:22 (Figure 4.8a, and marked as a dashed line in the KJPK and FCC panels of Figure 4.6), an up-down current pair appeared spanning from East to West over Hudson Bay, shown in the SECS map of Figure 4.8a. At this time, the RANK and SALU stations (mauve and orange, respectively) are both underneath the downward R1 currents, and RANK and FCC both lie within the Harang current system. A moderate westward horizontal current is shown in the shear region between the up-down current pair. Magnetic disturbances were observed at FCC and KJPK near this time, most notably at FCC but not at the stations north of FCC.

At 01:26 (Figure 4.8b, and marked in RANK and SALU panels of Figure 4.6), the SECS maps show that the current pair begins to extend northward. GMDs were seen at RANK and SALU, with TLA intervals in the By- and Bz-component at RANK. At this time, SALU is still underneath the downward R1 currents while RANK is located in the boundary region between downward and upward R1 currents. From about 01:26-01:28, strong westward currents are observed in the SECS maps extending over SALU that turn slightly northward to the north of RANK and southward to the south of RANK.

At 01:32-01:33 (Figure 4.9a, and marked in CDR and RBY panels of Figure 4.6), the upward portion of the current pair in red (to the south of the downward portion in blue) separates into two separate localized upward FAC systems on either side of the north edge of the Hudson Bay. At this time, WNW horizontal currents are enhanced overhead of the upward current lobes. GMDs were recorded at the two northern-most stations, CDR and RBY, with peaks near 01:32-01:33 and TLA intervals in the x-component at CDR and x- and z- components at RBY. While there are large positive excursions in the z-components at both CDR and RBY around 01:33 UT, the SECS maps show that the these disturbances appear to be caused by separate, localized upward FAC systems overhead each station on either side of the northern Hudson Bay. Over the next ten minutes from

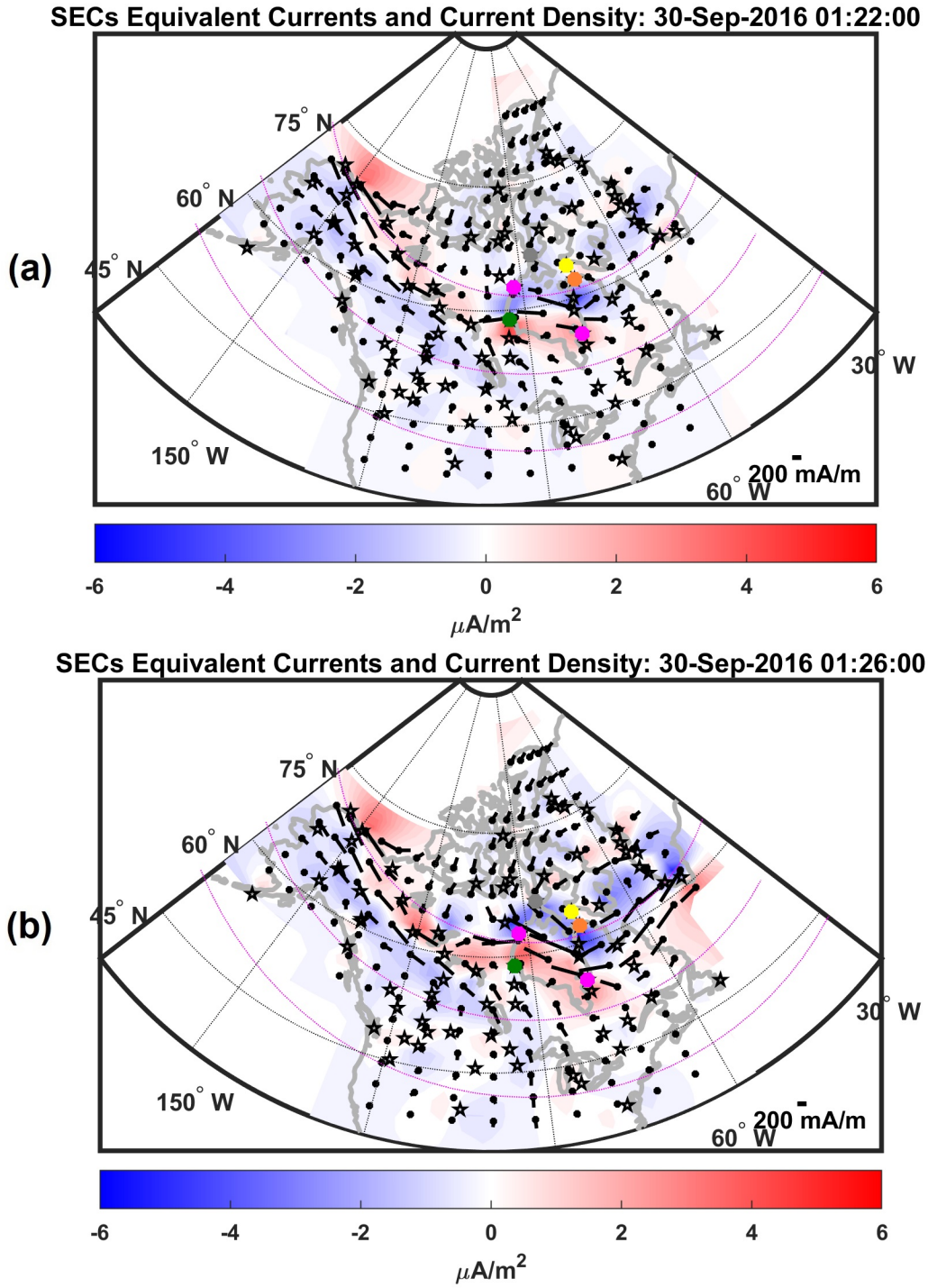

Figure 4.8: SECS maps during the 30 September 2016 event at 01:22 UT (a) and 01:26 UT (b) in geographic coordinates (dotted black lines) and geomagnetic coordinates (dotted pink lines). Each panel shows the combined field-aligned like current densities and equivalent currents. The dots indicate the points at which the equivalent current was determined and the vector gives the magnitude and direction. The stars mark the stations with usable data on that day. The key for the equivalent current is given in the lower right corner, and the color bar indicates the current density values. The colored circles mark CDR (yellow), RBY (gray), SALU (orange), RANK (mauve), FCC (green), and KJPK (pink).

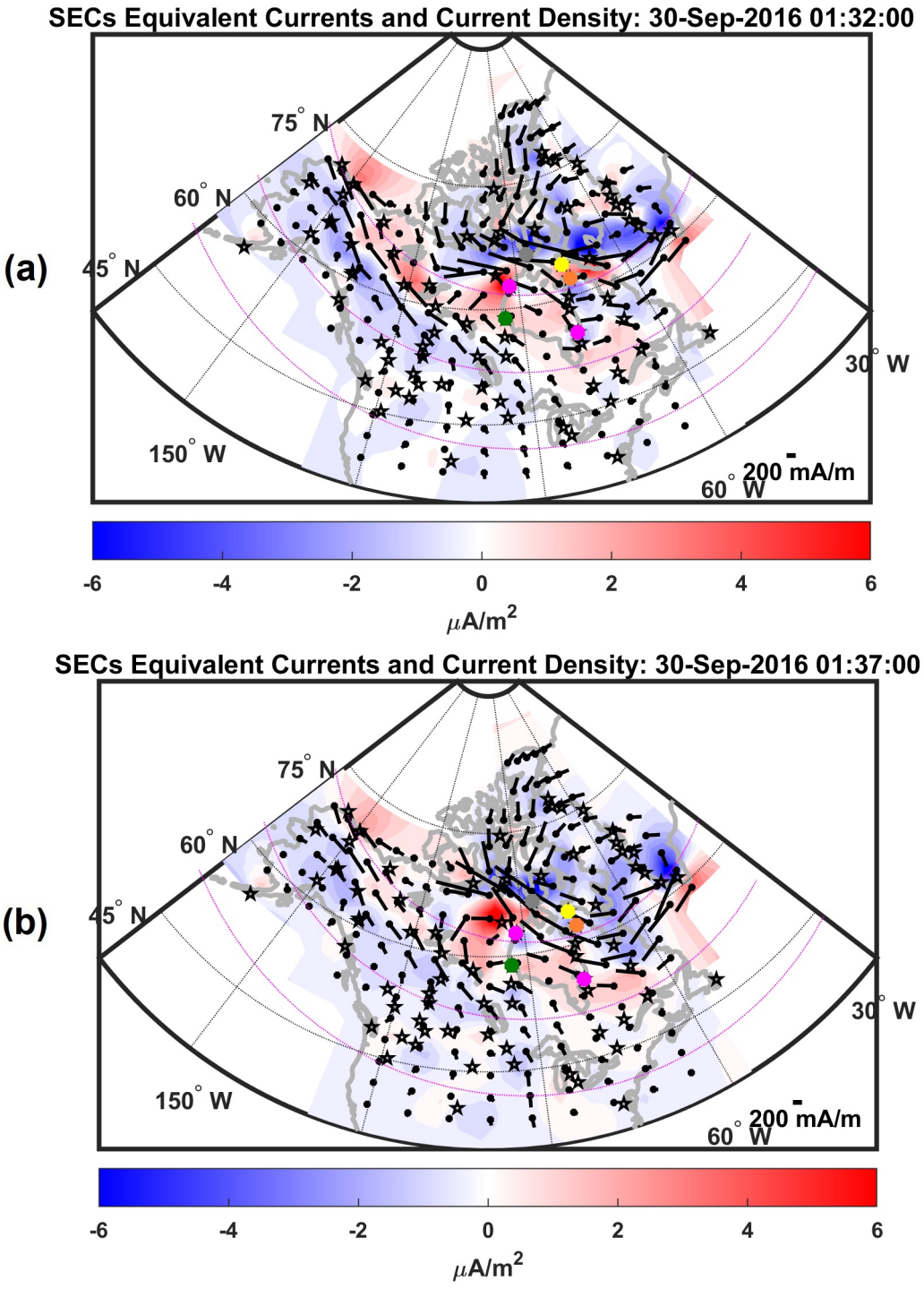

Figure 4.9: SECS maps during the 30 September 2016 event at 01:32 UT (a) and 01:37 UT (b), formatted the same as in Figure 4.8. The key for the equivalent current is given in the lower right corner, and the color bar indicates the current density values. The colored circles mark CDR (yellow), RBY (gray), SALU (orange), RANK (mauve), FCC (green), and KJPK (pink).

01:32 to 01:42, the upward current on the east side weakens, while the the upward current to the west moves slightly north west and intensifies at 01:37 (Figure 4.9b) when TLA dB/dt are measured at RANK (Figure 4.6 top panel) before weakening at 01:39 when the GMDs at all of the four northern stations begin to subside.

The ASI data images ("thg_asi_mosaic_201609300100kuuj.mpeg" of the data repository located at doi.org/10.7302/9par-f788) are consistent with the magnetic field data and SECS maps. A relatively stationary east-west auroral arc appeared just north of KJPK soon after the time of the first substorm auroral onset and extended across the bay over FCC by 01:18. The second substorm auroral onset started at 01:20 and initiated a series of brightenings. An intensification occurred at 01:22 and the arc began moving poleward, then from 01:25 to 01:26:30 auroral streamers emerged from the arc in two distinct parts: (a) one to the west of SALU over RANK and (b) another part to the south of SALU.

The arc portion (a) over RANK continued moving poleward and began to break up at 01:29 into a smaller part to the north and a longitudinally extending streamer to the south. The streamer north of RANK continued moving poleward and began to fade at 01:32. The streamer to the south of RANK intensified at 01:29:30, moved equatorward and dissipated by 01:31.

The arc portion (b) south of SALU at 01:26:30 had two portions within it, one to the south and extending slightly west of SALU and a stronger part SE of SALU. By 01:27:30 these two features were more distinct, extending in the NW-SE direction. The part south of SALU reached SALU at 01:27:45 while the eastern part moved equatorward. Both portions then retreated equatorward and faded away by 01:29. At this same time, a new streamer appeared NE of SALU, intensified as it moved equatorward and dissipated by 01:31. From 01:31:30, a small streamer appeared over RANK and moved equatorward while extending longitudinally at 01:32:30 and then fading. During this time, another intensification occurred NE of SALU and streamers moved equatorward, then faded by 01:35:45.

Figure 4.10 shows magnetic field data measured by the GOES-13 spacecraft during this event. The field-line footprint of GOES-13 at this time is shown in Figure 4.1. Here, Bz (plotted in red) is parallel to the Earth's rotation axis, positive northward, Bx is in the Earthward direction perpendicular to Bz, and By is in the eastward direction perpendicular to Bx and By. The sharp increases in Bz (highlighted as gray panels) signify dipolarization fronts (DF) in the magnetotail at geosynchronous orbit, the timing of which coincide with the timing of ionospheric current enhancements and subsequent GMDs measured on the ground.

The first substorm auroral onset occurred at 01:05 UT and a second onset occurred at 01:20 UT, both with DFs that occurred $\sim$2-3 minutes after. Perturbations were measured at the two southernmost stations, KJPK and FCC, corresponding closely with these DFs. An east-west auroral arc appeared around 01:12 north of KJPK and south of SALU. The arc brightened around 01:22 after

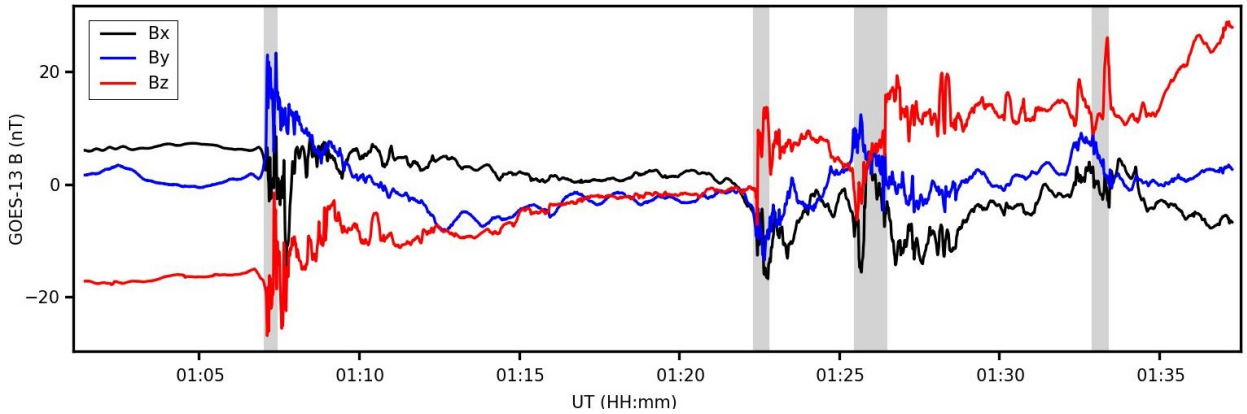

Figure 4.10: Magnetic field data measured by the GOES-13 spacecraft during the GMD/TLA event. The Bx component is measured

the second substorm onset and DF; the SECS maps show an E-W, up-down current pair extended across the southern Hudson Bay, westward horizontal currents increased in this region, and an GMD occurred at FCC. At about 01:26, a third DF occurred and the auroral arc began to move poleward and split into two separate parts over RANK and SALU, with auroral streamers that emerged from the arc and moved equatorward. The SECS maps show the up-down vertical current pair moved northward as well and the horizontal currents increased in the northwest direction; GMDs were observed at RANK and SALU with TLA intervals within the GMD at RANK, but not at SALU. Then around 01:33, another DF occurred at geosynchronous orbit as auroral patches were observed over RANK and SALU, developing into longitudinally localized streamers that moved equatorward; two distinct localized upward FACs enhanced on either side of the northern Hudson Bay and strong WNW horizontal currents extended over the region. During this time, GMDs occurred at CDR and RBY, with TLA intervals within the GMDs at both stations.

The auroral poleward expansion shown in the ASI data corresponds well with the poleward progression of GMDs and the timing of the largest ionospheric currents. DFs are the leading edge of dipolarizing flux bundles (DFB) (Nakamura et al., 2002), defined as transient ($\sim$ 40 s), localized ($\lesssim 3R_E$ in X_{GSM} and Y_{GSM}) flux tubes carrying strong northward magnetic field (Liu et al., 2018a). DFBs typically propagate at high speeds from the near-Earth reconnection region, efficiently transporting magnetic flux in short flow bursts referred to as bursty bulk flows (BBF). Auroral streamers emerging from poleward boundary intensifications (PBI) are considered to be the auroral signatures of BBFs (Henderson et al., 1998; Sergeev et al., 1999). Although there is no available plasma flow velocity data in the magnetotail during this time, the DFs at GOES-13 in the magnetotail paired with the PBI and streamers in the ionosphere appear to be evidence of a BBF event. Further, the double auroral onset nature of this case may indicate that the first auroral onset was a pseudo-breakup: a small, localized, substorm-like activation of auroral brightening that often

precedes a full-scale substorm. Pseudo-breakups can be associated with localized dipolarization in the tail that does not cause a global reconfiguration of the magnetotail (Akasofu, 1964) but can generate a localized current wedge (Pulkkinen, 1996; Pulkkinen et al., 1998).

We suggest that the cause of the poleward progression in this event is the tailward retreat of the magnetotail reconnection region due to successive DFBs. As the magnetic field dipolarizes, the reconnection region shifts downtail and this corresponds to the poleward shift of the larger magnetic footprint. Further, the Earthward propagation of fast flows in the plasma sheet cause the PBIs to extend equatorward and align in the north-south (NS) direction, forming auroral streamers (Nakamura et al., 2011; Ieda et al., 2016).

The overall structure of the GMDs are observed progressing northward; the peaks are measured closely in time for stations with similar magnetic latitudes, but the TLA intervals present are observed to be more longitudinally localized. For instance, RANK and SALU are about a degree separate in latitude and see relatively simultaneous peaks in all three components as the vertical current pair and auroral arc move northward, however TLA dB/dt are measured only at RANK. Then, CDR and RBY show a similar peaks in time but many more TLA intervals are observed at RBY than CDR. The stations on the western region of the Hudson Bay (RANK, RBY) where the localized upward FAC structure was stronger, exhibited the majority of TLA intervals in this event. It appears that while the GMDs at each station are a response to the larger-scale (roughly 1000 km) ionospheric currents, the TLA dB/dts are smaller-scale features of more localized FACs and auroral intensifications. Further, the SML index in this case does not reflect the the timing of the TLA dB/dt that align fairly closely with the auroral enhancements and features of the SECS maps. This discrepancy is likely due to the localization and rapidity of the ionospheric variations causing the TLA dB/dt; the SME index uses 1-minute cadence magnetic field data with a sliding 30-minute buffer that may not capture the small-scale ionospheric enhancements.

4.7 Discussion

Engebretson et al. (2019b) analyzed three separate GMD events that occurred during 2015. It was shown that all three of these events occurred within 1-hour of a substorm onset as well as a dipolarization at GOES-13, indicating that these events were generally related to fast flows from the magnetotail that penetrated the near-Earth plasma sheet. These events all exhibited a northward and westward spatial progression, and SECS maps during these events showed coinciding regions of localized horizontal current enhancements with $\sim$275 km radius. Two of these three events had TLA dB/dt intervals within the GMD: Event 1 on November 11, 2015 and Event 3 on October 9, 2015. In Event 1, TLA events occurred at two of the four stations that measured GMDs and in Event 3, TLA dB/dts occurred at one of the four stations. In both Events 1 and 3, the locations of

the GMDs that had associated TLA dB/dt are where the largest GMDs (>12 nT/s) occurred over the spatial extent of the disturbance; Event 2 exhibited no extreme GMDs and had no associated TLA signatures.

The TLA-related GMD events of the present study show some consistency with the spatial progression of those in Engebretson et al. (2019b): many TLA intervals occurred prior to the GMD at a more southern station (as shown in Figures 1.3 and 4.6) indicating northward progression of a fast ionospheric event. However, in comparison to substorm onsets, many TLA-related GMD events occurred to the west of the location of substorm onset defined by Newell & Gjerloev (2011), indicating an eastward progression in some cases. Rather than an eastward progression, this could be due to the overall northward progression of a larger ionospheric disturbance, but with more longitudinally localized variations (i.e., auroral streamers) causing the rapid TLA signatures at only some of the stations, as in the event analyzed in section 6.1.

Wei et al. (2021) presented an analysis of intense dB/dt events on the ground that occurred on January 7, 2015 . The perturbations occurred from 08:40-09:20 at 24 stations in mid- to high-latitude North America. During this event, large GMDs with TLA intervals within them occurred at SALU and KJPK. The study by Wei et al. (2021) included seven other stations that were also analyzed in the present study, but only four of these stations exhibited TLA signatures (ATHA, MEA, GILL, and RANK, temporally in that order). The larger perturbations and the TLA events showed a northward progression. This event occurred just after a substorm onset and in close temporal response to a BBF event carrying multiple DFs that were detected by the Cluster spacecraft at geosynchronous orbit in the magnetotail. It is suggested in Wei et al. (2020) that during this event, the large-scale substorm current wedge (SCW) system is composed of multiple localized R1-sense FAC structures driven by multiple BBFs, as has been previously proposed (Birn and Hesse, 2014; Liu et al., 2013) and demonstrated (Liu et al., 2015, 2018a).

Weygand et al. (2021) analyzed GMDs during 2015 and 2017 at CDR and KJPK and found that a majority of the events occurred within the westward electrojet and the pre-midnight events often occurred beneath the Harang current system. In section 6.1, The pre-midnight event on 30 September 2016 is consistent with these observations: the SECS maps at 01:22 and 01:26 (Figures 4.8a and 4.8b) show that FCC and KJPK were within the upward Harang current with the WEJ flowing between this region and the downward Region 1 currents to the north, overhead RANK and SALU. Then at 01:32 UT (Figure 4.9a), localized and transient upward FACs appear separately above RANK to the west and CDR to the east; the upward FAC lobe on the west strengthened near RBY when TLA dB/dt were measured at 01:37 UT (Figure 4.9b). These localized FACs were likely caused by an instability in the inner plasma sheet, as evidenced by the dipolarization observed at GOES-13. The TLA dB/dt at RANK (01:26 UT) appeared when the station was located in a boundary region between upward and downward currents, as was the case for the TLA dB/dt

that occurred at CDR near 01:32 UT and at RBY near 01:32 and 01:37 UT.

4.8 Summary & Conclusions

In this chapter, we have shown that TLA dB/dt events occurred primarily at night, preferentially in the pre-midnight sector. These high-frequency perturbations occurred only in the high magnetic latitude region above 60° MLAT, with a majority in the 65-74° MLAT band where substorm onset and expansion occurs. TLA events most often occurred within 60 minutes of substorm onsets but there is also a subset referred to as unrelated events that occurred more than 60 minutes after substorm onset and in the absence of a CME-driven geomagnetic storm.

TLA dB/dt events occurred most often during the declining phase of the solar cycle when the yearly mean sunspot number decreases but the number of substorm onsets per year increases from solar maximum. TLA events were most common during intervals of mild SuperMAG ring current activity and fast solar wind flow speeds. This may indicate a relationship between TLA and GMD events with weak CIR-driven storms due to fast solar wind flow speeds emanating from coronal holes. Future work includes an investigation of this potential association, especially for the so-called unrelated TLA events.

We have shown in this chapter that many TLA events during 2015-2019 were associated with GMDs, often preceding the event or occurring within the overall disturbance. Not only were TLA-related GMD events common, but as GMD amplitudes increased, the likelihood that TLA intervals were associated with the GMD vastly increased: 81% of hour windows with extreme, $>$12 nT/s GMDs had associated TLA intervals, and 93% of even larger GMDs $>$20 nT/s included TLA intervals. Engebretson et al. (2019a, b; 2021) and Weygand et al. (2021) all show that GMDs have an effective radius of $\sim$300 km. The results presented here show that high-frequency intervals of the magnetic field can be even more localized: TLA dB/dt intervals often occurred at fewer stations than the extent of the GMDs were measured, as shown in Figure 1.3, the event on September 30, 2016, Events 1 and 3 of Engebretson et al. (2019b) and the January 7, 2015 event of Wei et al. (2021). While TLA dB/dt are commonly more localized than GMD events, the locations of the largest TLA dB/dt most often signify the locations of the largest GMDs.

This chapter has presented multiple cases of TLA dB/dt correlated with magnetotail dipolarizations, as well as localized FAC structures, PBIs and auroral streamers; one of which also included measurements of bursty Earth-directed plasma flows in the magnetotail (Wei et al., 2021). We show that TLA events are closely associated with substorm activity, but they also occur many tens of minutes and even hours apart from substorm onsets, as well as in locations very far from the location of the onsets. The spatial and temporal separation of some TLA events from substorms indicates that TLA events are driven by M-I processes that are often, but not always related to sub-

storms. Additionally, TLA events may be the ground manifestations of highly localized pseudo-breakups and/or localized substorm current wedgelets driven by individual closed-field line DFBs as in Liu et al. (2015, 2018), and these could have GIC-driving potential but are not reflected in large-scale geomagnetic activity indices like SME.

Strong magnetic perturbations and Pi 2 pulsations are closely correlated with auroral intensifications followed by streamers driven by DFs and fast flow bursts in the magnetotail (Kepko and Kivelson, 1999; Lyons et al., 2012; Nishimura et al., 2012). This study has shown that disturbances in the Pi 1 frequency range are often present in these situations as well. TLA magnetic perturbations appear to have complex M-I drivers, but they are likely the result of small-scale ionospheric current phenomena coupled to the magnetotail that often but do not always occur during substorms. Because these high-frequency signatures are very often associated with the most extreme nighttime GMDs that can drive GICs on Earth (and even though magnetic variations with Pi 1 and short Pi 2 periods do not drive GICs directly), TLA dB/dt and the associated M-I phenomena such as BBFs are important to take into account when investigating the complex dynamics that can give rise to GIC. Future work includes a broader investigation of the ionospheric currents, magnetotail dynamics- especially fast plasma flows in the tail- and solar wind drivers of TLA-related GMD events. Identification and analysis of TLA dB/dt in association with nighttime GMDs will continue to provide insight on their M-I drivers and their behavior from the ionosphere to the ground, where GMDs with associated TLA intervals pose the greatest threat of hazardous GICs.

CHAPTER 5

Conclusions and Future Work

5.1 Discussion of Results and Impacts

5.1.1 Results and Impacts of Chapter 2

In Chapter 2, we presented an introductory discovery study on high-frequency TLA signatures and provided evidence for their importance in the context of GICs. The chapter initially addresses the first part of Guiding Question 1 that asks how often do TLA signatures occur and what are their characteristics and provides a broad answer to Guiding Question 3 that asks what relationship TLA events have to other GIC-causing space weather events.

Chapter 2 investigated the occurrence of TLA events with a set of TLA dB/dt intervals identified in six MACCS stations throughout 2015. We identified a substantial number of TLA events, many with very large derivative amplitudes ($>$ 10 nT/s). We found that these rapid dB/dt signatures occur primarily during local magnetic nighttime and in the Fall-Winter months. Further, TLA events were relatively localized, more often occurring at just one of the six MACCS stations. We showed that TLA events exhibit a strong association to substorm activity and nighttime GMDs and a significant portion of the largest $>$ 10 nT/s GMD events in 2015 had associated TLA intervals.

An important impact of the research in Chapter 2 is our finding that the main driver for TLA dB/dt was not SCs that were previously considered to be the cause of the most rapid and large-amplitude perturbations on the ground, but rather that TLA dB/dt were more closely related to small-scale processes and conjunctions of small-scale space weather events (i.e., GMDs and substorms). This suggests that there are more localized and small-scale ionospheric phenomena responsible for giving rise to TLA events. Further, we found a subset of TLA events that occurred in the absence of a geomagnetic storm phase and more than 60 minutes from the most recent substorm onset; this suggests that some small-scale M-I processes that can give rise to large dB/dt and subsequent GICs on the ground can occur during relatively quiet geomagnetic conditions.

5.1.2 Results and Impacts of Chapter 3

In Chapter 3, Guiding Question 2 is answered: we presented an automated process for identifying high-frequency dB/dt intervals in ground magnetometer data. This method combines 1) a filtering process derived from a statistical analysis of noise-type and geophysical dB/dt intervals with 2) an SVM classification of the filtered intervals to return a list of all the second-timescale, large-amplitude (>6 nT/s) perturbations in a set of magnetic field data, each with a classification of either noise-type or geophysical.

A key finding from the performance analysis of the identification process is that common techniques for the identification and removal of magnetic noise are insufficient, motivating the need for the use of the automated process we have developed. The data processing procedure used by the SuperMAG data service incorporates both resampling the data as well as automated and manual data cleaning to remove noise signatures. We showed in Chapter 3 that despite this procedure, the magnetic field data are still contaminated with signatures of noise interference. Our method performs very well (HSS = 0.94) at identifying these intervals of data and correctly classifies them.

The automated geomagnetic disturbance classifier described in Chapter 3 provides a valuable technique that can be easily applied to massive magnetic field databases. As discussed in Chapter 1.4, the need for high-resolution magnetic field data is growing, but the use of such data presents challenges in dealing with data contamination. Higher-temporal resolution data helps to improve accuracy for GIC forecasting and other magnetic field studies, as well as preserves the relevant TLA signatures introduced in Chapter 2, that could be altered or removed with common data cleaning procedures. The method we presented provides a solution to this problem, targeting high-frequency noise intervals in magnetic field data, while retaining important high-frequency signatures relevant to M-I phenomena.

5.1.3 Results and Impacts of Chapter 4

In Chapter 4, we presented a comprehensive analysis on a large database of TLA events that occurred at 12 stations in the high-latitude region above 60° MLAT. With this study, we extended the research conducted in Chapter 1 to more definitively respond to Guiding Questions 1 and 3.

We showed in Chapter 4 that TLA events occur throughout the duration of the solar cycle, but were most frequent in the declining phase during intervals of decreased global geomagnetic activity and increased solar wind flow speed. TLA events only occur in the high-latitude region and were not identified in magnetometer data measured at middle and equatorial magnetic latitudes. We provided supporting evidence for the strong association of TLA events with substorm activity and nighttime GMDs, and we also showed a large number of unrelated TLA/GMD events that can occur in the absence of CME-driven geomagnetic storms and substorm activity.

There is a clear correlation between TLA dB/dt intervals and the largest ($>$ 12 nT/s) GMD events. We stated that nearly all of the most extreme GMD events ($>$ 20 nT/s) had associated TLA dB/dt intervals. TLA perturbations were often even more localized than the spatial extent of the GMDs. Often when GMDs occurred at more than one station, TLA dB/dt were measured at fewer stations and the stations where TLA dB/dt were measured were the locations of the most extreme GMDs. These behaviors imply the usefulness of TLA intervals to understand the evolution of small-scale ionospheric perturbations that pose a threat of GIC-driving. TLA dB/dt could be used as an indicator for the location of the most extreme geomagnetic disturbances, and/or as an indicator for the timing of a growing perturbation. As GIC research becomes more focused on the localized nature of the geomagnetic field, TLA dB/dt can be used to gain a more explicit understanding of geomagnetic perturbations on small spatial and temporal scales and ultimately more accurately predict where and when the greatest GIC threat will occur.

Finally, in Chapter 4 we illustrate that GMD events with associated TLA dB/dt are related to dipolarizations of the nightside geomagnetic field at geosynchronous orbit and fast plasma flows toward Earth that result in localized FAC structures and subsequent PBIs and auroral streamers. In the September 30, 2016 event analyzed in Chapter 4.6.1, we showed that TLA dB/dt were measured when the stations were located in boundary regions between upward and downward currents, suggesting ionospheric flow shear may be involved. In extended research of Chapter 4 (see Appendix C.3), we discuss post-midnight TLA-related GMD events related to omega band auroras that can also be produced by fast Earthward flows and provide an example of such an event. The results of the Engebretson et al. (2020) study showed that during GMD events, a current generator model was favored over a voltage generator, suggesting that excitation of resonant field-line oscillations coincide with GMDs.

Our results from Chapter 4 and Appendix C.3 suggest that fast flows from the magnetotail are involved in exciting oscillations in the Pi 1 and short Pi 2 range and that these excitations are not always related to substorm activity. Such fast flow events cause small-scale FACs that couple to the ionosphere, causing transient auroral features like PBIs and streamers and subsequent rapid and localized high-frequency TLA dB/dt on the ground. These perturbations are a key component in extreme nighttime GMDs that can drive GICs.

5.1.4 Caveats

TLA dB/dt were grouped into separate events based on 1-hour intervals in order to analyze all TLA dB/dt that may be related to one another. Further, as highlighted in Chapter 2.2, the study of Chapter 2 referred to TLA events if they occurred within the same hour at multiple stations, whereas the studies in Chapters 3 and 4 separated TLA events by each station. These methods of

separating TLA events based on their occurrence at more than one station introduce a source of discrepancy in the statistics of TLA events. However, an examination of the effect of separating by station for the TLA events from 2015-2019 found that this effect is not significant enough to alter the statistical characteristics of TLA events we have examined in this dissertation. From 2015-2019, there were 598 hour event windows containing TLA dB/dt at any station. Separating into distinct events based on station location resulted in 702 events (i.e., about 100 of those hour event windows contained TLA events at more than one station). Because TLA events were commonly localized at one station, the station separation of events did not greatly impact the statistical results.

Another potential source of statistical discrepancy is the event window timescale of 1-hour. Because TLA intervals often occur prior to or within a nighttime GMD that lasts 5-15 minutes, we chose to group all TLA dB/dt that occur within the GMD as well as in the 15-20 minutes prior to and after the GMD. As mentioned in Chapter 3.3, extending the length of an event window would not change the number of TLA events (unless changed to event windows lasting multiple hours or days). However, grouping TLA dB/dt by a shorter timescale of 15-20 minutes instead may introduce some differences in the statistical results. As in the example shown in Figure 1.3 where multiple GMDs occur within 1-hour, there may be some instances where TLA dB/dt could be related to separate GMDs within a 1-hour window. It is presumed that a shorter-timescale grouping may produce slight differences in the number of TLA events, but would likely not greatly impact the overall statistical results of this dissertation research. Investigation of the impact of shorter-timescale grouping of TLA dB/dt should be a part of future studies on GMD events with associated TLA intervals.

5.2 Future Work

TLA dB/dt are magnetic pulsations with frequencies in the Pi 1-2 range. Until now, Pi 1/2 have been considered as key components of substorm dynamics (Heacock and Hunsucker, 1981), but they have not been thought to have much importance in the context of GICs. From the research presented in this dissertation, we have shown that they are an important feature of almost all of the most extreme GMDs. As many TLA dB/dt precede larger, longer GMDs or occur in the location of the largest GMD, the occurrences of these signatures indicates that some physical M-I process has been triggered that can result in GICs. Further, it has been shown that TLA-related GMDs are related to fast Earthward plasma flows and can occur without geomagnetic storm and/or substorm activity. A continued study of the M-I dynamics involved in causing these unrelated events and an assessment of the GICs that can be caused by TLA/GMD events during all levels of geomagnetic activity is recommended moving forward.

BBFs have been associated to Pi 2 (Kepko et al., 2001) and Ps 6/Pi 3 pulsations (Opgenoorth

et al., 1983), and these ULF wave frequencies have been related to omega bands, PBIs and streamers. These auroral structures have gained attention for their usefulness in determining the spatial and temporal behavior of dB/dt that may have high impact on GIC research and forecasting (Zou et al., 2022). We have shown that dB/dt in the Pi 1 range also occur in association to BBFs and all three of the resultant auroral structures mentioned above. Further investigation of fast flows, magnetotail instabilities and Alfvén wave coupling is important to understand the role Pi 1-2 range perturbations have in M-I coupling and within events with GIC-driving potential.

Continued investigation of TLA events requires ionospheric and magnetospheric data at higher temporal and spatial resolutions. Analysis of the specific TLA dB/dt in comparison to ASI data and SECS maps with higher temporal resolution will provide more specific connections to ionospheric dynamics. Further, measurements of the magnetic field by multiple spacecraft spaced close together at the relative width of BBFs (2-3 R_E) would allow for a more comprehensive investigation of substorm current wedgelets driven by multiple BBFs.

Inclusion of these higher frequency components in dB/dt studies will add more detailed understanding of the ground geomagnetic response to ionospheric disturbances that could cause large GICs. A more precise view of the ground magnetic field may prove useful in improving dB/dt forecasting and modeling in an effort to predict and mitigate GICs. Further, it is suggested that going forward, BBFs are considered as a potential magnetospheric driver for GICs on the ground; we suggest that BBFs and the ionospheric responses are investigated more thoroughly to better understand their role in generating rapid and extreme surface dB/dt and assess the threat of GICs.

Finally, measurement of the effective geomagnetically induced currents is necessary to evaluate the potential impact on small-scale electronics and sensors on Earth caused by TLA dB/dt intervals of the surface magnetic field as well as the resulting geoelectric peaks caused by extreme GMDs with associated TLA dB/dt.

APPENDIX A

Chapter 2 Appendix

A.1 Supporting Information

The information provided here details the station locations used in the study of Chapter 2. Table A.1 lists the geographic latitude and longitude, and the corrected geomagnetic latitude and longitude of the six MACCS stations used in this study. Figure A.1 shows these six stations at their respective geomagnetic coordinates. These corrected geomagnetic coordinates were calculated for the year of 2015 with the IGRF transformation tool of the World Data Center (WDC) for Geomagnetism, Kyoto.

Station Code	Geographic Latitude	Geographic Longitude	Corrected Geomagnetic Latitude	Corrected Geomagnetic Longitude
IGL	69.3	278.2	78.63	343.3
GJO	68.6	264.2	76.86	320.5
RBY	66.5	273.8	75.62	322.33
PGG	66.1	294.2	75.53	11.16
CDR	64.2	283.4	73.70	353.8
NAN	56.2	298.3	65.67	14.80

Table A.1: Locations of MACCS stations used in the study of Chapter 2.

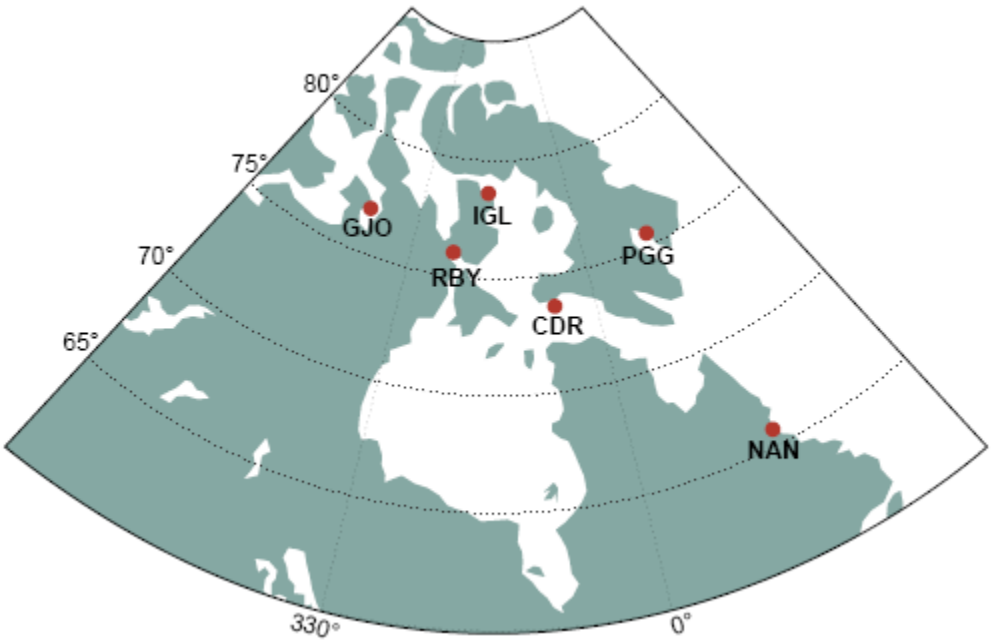

Figure A.1: Map of MACCS stations used in this study with lines of corrected geomagnetic latitude.

APPENDIX B

Chapter 3 Appendix

B.1 Extended Research: Machine Learning Algorithm Tuning

B.1.1 Introduction

This section provides supplemental information to the research described in Chapter 3. Three machine learning algorithms are outlined and the tuning process that lead to the selection of the SVM classifier in Chapter 3 is described. We provide background information on these other three classification algorithms, define the hyper-parameters that were cross-validated, and provide accuracy scores on the test data set to show evidence for the determination that the SVM classifier performed the best out of the four algorithms.

B.1.2 Tuning Process

For this study, four machine learning algorithms were analyzed to determine the model that performed the highest accuracy score on the test data. Each of the four algorithms were tuned with the tuning process outlined below and tested on a dB/dt test set from the eight stations for the year of 2016. The machine learning classification algorithms that were analyzed are the decision tree, random forest, support vector machine (SVM), and Gaussian process classifier (GPC).

A Gaussian process classifier (GPC) is similar to an SVM in that it also relies on a kernel function, but uses this kernel differently. A GPC classifies data by predicting possible functions that fit the training data (Rasmussen and Williams, 2006). The initial assumptions for the functions that may possibly fit the training data are determined by the kernel function which represents the probability distribution over these functions. The model assumes a prior probability distribution of these functions via the kernel function and then updates this probability distribution based on information from the training set and using Bayesian inference methodology. In the tuning process, four different kernel functions were analyzed to determine the kernel function that performs the

best on the training data: the radial basis function (RBF), the dot product function, the Matern function and the rational quadratic function.

A decision tree predicts classes by splitting the data into subsamples based on true/false requirements until every sample is isolated into a class (Song and Lu, 2015). Every time the model splits the dataset, a node is created and each group that the data was split into is referred to as a leaf. The loss function for a decision tree is a function that informs the model of the quality of each split, usually by comparing the class distribution before and after the split via the gini or entropy functions- these are the "criterion" hyper-parameters in Table B.1. Each time a node is split into subsets, the depth of the tree increases up until the maximum allowable depth specified (max depth parameter in Table B.1). The max features parameter is the maximum number of features used to determine each split, the Min samples/split parameter represents the minimum number of dB/dt samples required in order to make another split and min samples/leaf is the minimum number of dB/dt samples required to be in each group (leaf) after splitting.

A random forest is an ensemble of decision tree predictors whose majority vote determines the output prediction. Each tree is built with a random subset of the training data (with the same distribution as the overall training set) as well as a random combination of the features (the number of which is less than the total number of features and designated by the 'maximum features' hyper-parameter) and the final prediction is the popular vote of these trees (Breiman, 1996).

Each tree in a random forest is built with the same hyper-parameters, but not necessarily the same training data. In addition to the decision tree's hyper-parameters, a random forest has a setting to determine how many trees will be built in the ensemble. The random forest also has the bootstrap hyper-parameter: if True, each tree is built with a random but equally sized subset of the training data with replacement (i.e. each random subset is taken from the full data set so some trees have the same samples) and if False each tree is built from the entire data set (Breiman, 2001).

The general tuning process is as follows: the training data were split into separate but equally proportional sets (referred to as a "fold" of the data) and then a model with a combination of of hyper-parameters was trained and tested on each of the partitioned data sets and the model that scored the highest is selected for those hyper-parameters. The number of combinations of hyper-parameters to be trained and tested on was based on each models required hyper-parameters and the computation time to fit each model with each combination of parameters. The number of separate folds each model was split into, as well as the number of combinations of hyper-parameters and the overall number of fits of the model are listed in Table B.1. The specific hyper-parameters that resulted in the best model for each type of model are also listed in Table B.1.

Each of the four models were tuned and cross-validated with the specific number of folds and fits shown in Table S1. The optimal hyper-parameters determined are listed. Each model is then fit to the training data with the optimal hyper-parameters, then the model is tested on the test data

set that consists of data from each of the eight stations for the year of 2016, the test scores are listed at the bottom of Table S1. The results in Table S1 show that the SVM model had the highest accuracy and Heidke skill score on the test set. While the POD score was slightly higher for the random forest, the SVM classifier was chosen because the average of the three test scores for SVM was higher than tht of the random forest. Thus, the SVM was chosen as the best classifier for high-frequency dB/dt signatures in magnetic field data.

Model		SVM	GPC	Decision Tree	Random Forest
Tuning	Folds	10	5	10	5
	Candidates	49	4	2700	2880
	Fits	490	20	27000	14400
Optimal hyper-parameters		Kernel = RBF γ = 1 C = 10	Kernel = Matern length scale = 1 ν = 1.5	Criterion = entropy Max depth = 8 Max features = 3 Min samples/leaf = 3 Min samples/split = 9	Criterion = gini Max depth = 10 Max features = 5 Min samples/leaf = 2 Min samples/split = 3 Number of trees = 200 Bootstrap = True
Accuracy		0.9825	0.9784	0.9677	0.9627
POD		0.9112	0.9043	0.8497	0.9590
HSS		0.8688	0.8422	0.7671	0.7607

Table B.1: Table detailing the tuning, training and testing information for four machine learning algorithms

B.1.3 Discussion of Hyper-parameter Selection in SVM Classifier

As discussed in Chapter 3, the SVM classifier with the radial basis function requires the specification of the γ and C hyper-parameters. The γ parameter controls the radius of influence, or similarity radius, of samples used as support vectors. A smaller value of γ means a larger similarity radius. The C parameter determines how much the model can decrease the margin of the decision boundary in return for a larger number of correct classifications. A large value of C means that the decision boundary can be much closer to the training samples if more samples are classified correctly.

Figure B.1 is a visualization of the decision function on an example classification problem with two input features and two target classes. Each box in the 4x3 grid is an example feature space for a different combination of hyper-parameters with increasing values of γ downward and increasing values of C to the right. These plots were created using the example code available at scikit-learn.org/stable/auto_examples/svm/plot_rbf_parameters.

html#sphx-glr-download-auto-examples-svm-plot-rbf-parameters-py.

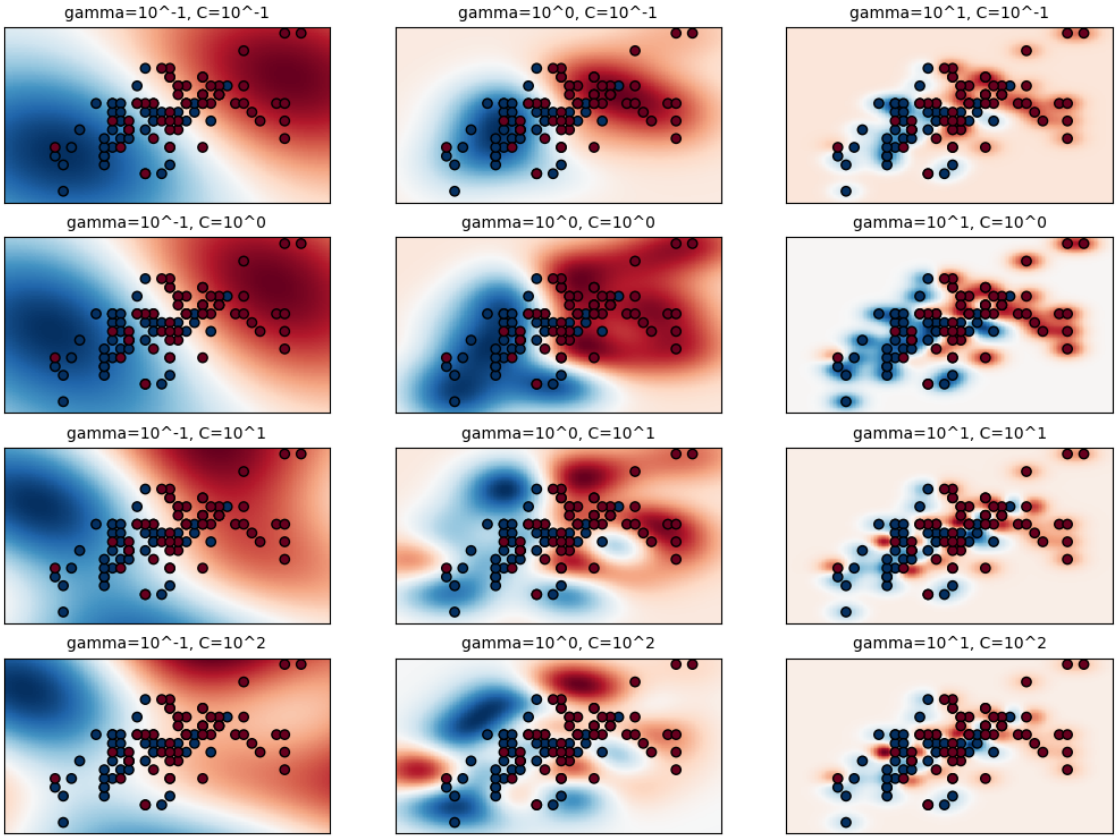

Figure B.1: Grid of example feature spaces and decision functions for various combinations of γ and C in the RBF kernel of the SVM classifier. The blue and red circles represent exampel target classes and the blue and red shading represents the regions where the decision function classifies the targets as blue or red.

When gamma is small, the similarity radius for grouping samples and classifying them is larger. This means that the shape of the data cannot be properly identified and the decision boundary is too broad. When gamma is large, the opposite occurs and the SVM overfits to the data, capturing the exact shape of the training data and resulting in an inability to generalize to new data. When C is small, the margin for the decision boundary can be large regardless of the amount of misclassified samples and the margin decreases for increasing C.

The top left box of Figure B.1 shows the decision function when γ and C are both small. The similarity radius is very large and the margin of the decision boundary is large, so the decision function in this case is just a linear separator between classes. The bottom right box shows the opposite case where γ and C are both large, the decision boundary is overfitting the samples, classifying all samples correctly but with no ability to generalize to new data in this feature space.

When gamma is small and C is large (bottom left), the similarity radius is large so the SVM

groups data in a broad area of the feature space, but there is a penalty for incorrect classifications so the decision boundary margin is reduced and the classification region is relocated so there are less misclassified samples. When gamma is large and C is small (top right), the similarity radius is small so the region of influence of each sample is small and thus classification regions are small. Then, because C is large, the margin of the decision boundary to the samples is very small and the model incorrectly generalizes and thus only samples extremely close to the blue circles are labeled blue, and *everywhere* else is labeled more likely red.

For this two-dimensional feature space, the two best performing models are those in the center of the grid (located at (2,2) and (3,2)). These classifiers balance the size of the similarity radius and the decision boundary margin to obtain the largest number of correctly classified samples. The RBF kernel with γ = 1 and C = 10 is what is used for the geomagnetic disturbance developed and described in section 3.7. The model has an intermediate value of γ and a slightly higher value for C resulting in a slight reduction of the boundary margin in return for more specific classification of the targets. The result is that less geomagnetic TLA dB/dt intervals would be misclassified at noise-type events.

The value for Gamma is intermediate so the model is able to define a similarity radius that effectively captures the shape of the sample groups in the feature space; the value for C is slightly higher than the median of the typical range for C, so the decision boundary margin is slightly closer to the samples in order to maximize the number of correctly classified samples, indicating that some of the samples of each classification are quite close to one another in the feature space. Comparison of the two best performing example classifiers in Figure B.1 shows that these hyper-parameters tune the model to have a more distinct decision function in the feature space than both γ and C values of 1.

The SVM classifier for geomagnetic and noise-type dB/dt has input features of dB, dB/dt, dt, time of day, day of year, and magnetic latitude of the station. The filters described in section 3.6 removed a large number of noise-type intervals and narrowed the training samples to a more defined range of dB, dt and dB/dt values. Thus, the dB, dB/dt and dt features are all quite similar to one another for the noise-type and geomagnetic dB/dt. From our further analysis of longer-term temporal trends and spatial behavior of TLA dB/dt from the study in Chapter 4, we know that TLA dB/dt occur more often at nighttime and is strongly associated with substorm activity that is more common around the equinoxes. Further, TLA dB/dt occur only at high-latitudes and most commonly from 65-74° MLAT. Noise-type dB/dt can occur at any location and at any time, however some stations are more noisy at random times due to instrumental error and/or during daylight hours due to station location relative to human interference.

This information paired with the behavior of hyper-parameter combinations shown in Figure B.1 and the resultant high performance of the SVM classifier developed in section 3.7 suggests

that the decision function identifies some distinctions and nuances of the temporal and spatial characteristics of geomagnetic and noise-type dB/dt. Because the model still makes some incorrect classifications of both types of dB/dt intervals, this suggests that there are some noise-type and geomagnetic dB/dt that are virtually identical or that there are some intervals with typical amplitude and timescale characteristics of one type but occur at a magnetic latitude or at a time that is more common for the opposite type of interval.

B.2 Identification of the F2 Trace in Ionosonde Data with U-net Approach

This section details research conducted during an internship with Air Force Research Laboratory (AFRL) at Kirtland Air Force Base in Albuquerque, New Mexico. This internship was a joint effort between AFRL and the National Science Foundation, and began September 2021 and ended May 2022. While this project did not directly contribute to the research on TLA events that are the topic of this dissertation as a whole, the research described in this section aided in a broader understanding of machine learning applications to space weather that did contribute to the development of the automated TLA classification method of Chapter 3. The data and transmitter/receiver locations described in this section are classified and so are represented with arbitrary labels. Collaborators of this work are: Kathleen Shurkin (AFRL Advisor), Eugene Dao (Team Member), John Carilli (Team Member), Capt. Tyler Hussey (Team Member).

Approved for public release; distribution is unlimited. Public Affairs release approval: AFRL20232104.

B.2.1 Background & Motivation

An ionogram is the displayed data recorded from an ionosonde: an instrument set that surveys ionospheric conditions by transmitting and receiving high-frequency radio waves through the ionosphere and measuring their parameters (i.e., frequency and time of travel). The resulting ionogram is a plot of the time of arrival (or altitude) as a function of the frequencies reflected by the ionosphere and effectively maps the main parameters of the ionospheric layers present. An oblique (OB) ionogram refers to ionosonde data that was recorded at a receiver that is some ground range distance from the transmitter; a vertical incidence (VI) ionogram is created from data recorded at a receiver at the same location as the transmitter. The traces in an oblique ionogram appear ”stretched” along the frequency axis because of the frequency shift due to the angle of incidence upon the ionosphere (Picquenard, 1974).

Beyond trace transformations due to the degree of obliqueness, the ionogram shows ionospheric anomalies and disturbances like the presence of the sporadic-E layer: a thin, highly-ionized layer in the E region that blankets the ionosphere above (Whitehead, 1989) or the spread-F phenomenon that occurs due to plasma instabilities in the F-layer (Herman, 1966). For many reasons, it is useful to observe and analyze the radiative state of the ionosphere: one common motivation being that these space weather disturbances can significantly impact radio communications. For decades, image analysis techniques have been used to analyze ionograms in an effort to classify or extract the various features of the ionogram traces (Tsai and Berkey, 2000).

The research project detailed in this report consists of analyzing the quality of a convolutional neural network (CNN) model to identify the F2 trace within ionosonde data. Further, a central goal of this research is to determine how well such a model performs when classifying ionograms of varying degrees of obliqueness and estimate the amount of data required for optimal performance of the model. More specifically, our goal was to use a U-net architecture (Ronneberger et al., 2015) to identify the F2 trace within the ionograms independently of the degree of obliqueness of the data.

B.2.2 Method & Data

One of the central goals of this research project is to determine the efficacy of a convolutional neural network with a U-net architecture to effectively identify the F2 trace in ionograms. To accomplish this goal, a U-net model was trained on ionogram images with labels (or masks) that include only the pixels of the image that are classified as the F2 trace. The model scores were evaluated to determine the optimal number of epochs required to achieve the best performing model. The best performing model in this case was determined when the binary cross-entropy loss function (a function that measures the error in the model) does not decrease for 25 epochs.

The training data used in this study are 296 images created from oblique ionosonde data recorded at a receiver, R1. The transmission site for these ionogram data is located approximately 1100 km away at tranmission site T2. In order to test the U-net model performance with more training data, images from the "Pink data set" were labeled and added to the training data in multiples of the original 296 from 2x to 5x. The Pink data set is created from ionograms from multiple transmitters that are anonymous so there is a mix of degrees of obliqueness within the added data. The test set for the model is comprised of 274 ionogram images and masks from the R1 receiver and three transmitter sites: T1, T2, T3. T1 is located about 100 km from the R1 receiver, T2 is $\sim$1100 km from R1 and the T3 site with ground range $\sim$2700 km to R1.

All of the ionogram images used for training and testing are black and white (i.e., single channel), 200 x 200 pixels, padded with 28 pixels on all sides so that the final image size input to the

model is 256 x 256.

The specific U-net architecture was constructed by Capt. Tyler Hussey (Deputy Branch Chief - RVBX) and was modeled after the original U-net description by Ronneberger (2015). A typical convolutional layer of a CNN takes an input image and performs matrix multiplication (or dot product) with the image and a filter (a matrix of weights used to detect some part of the image) that is applied to a portion of the image. The output value is stored in the output of the layer. Then, the filter is shifted to the next portion of the image and another value is added to the output until all portions of the image have been covered with the filter and a complete output has been constructed. The CNN is informed by a loss function to determine how well the weights performed at identifying the feature and then the model updates the weights in the next epoch to optimize (decrease) the loss function.

The configuration of the U-net model is shown in Figure B.2. The principle behind a U-net architecture is to perform convolutions as a typical neural network, however it is followed by an expansive path which performs transposed convolutions that upsample the image back to the input image size. The final output of the model are image predictions with equal size as the input (256 x 256); the model predicts for every pixel in the input image the likelihood (a value between 0 and 1) that it is part of the F2 trace. Pixel predictions of $\geq$0.5 are part of the F2 trace. This model will be referred to as the Tyler Hussey (TH) model. The loss function used for this model is the binary cross-entropy loss.

To evaluate the model performance, the Mean IoU and Dice coefficient are used. The accuracy represents the total number of correctly predicted pixels; the loss is a metric that indicates how poorly the model predicted a single pixel. A common problem in image segmentation occurs when the target pixel group is small relative to the image size so the model can predict all zero (i.e., "not in target group") and accomplish a relatively high accuracy classification. For this reason, the Mean Intersection over Union (IoU) and Dice coefficient are used to better evaluate the model training performance. Mean IoU is a common metric used in image segmentation problems.

IoU (also referred to as Jaccard index (Jaccard, 1912), shown in Equation 1) is a measure of the intersection of the pixels in the true mask and predicted mask divided by the union of the pixels. The Mean IoU is the average of the IoU values for every sample in the training batch or test set. The IoU equation is,

$$IoU = \frac{|A \cap B|}{|A \cup B|} = \frac{TP}{(TP + FP + FN)} \tag{B.1}$$

where A represents the mask and B represents the predicted image. Here, TP = True Positive predictions, FP = False Positive predictions, and FN = False Negative predictions. "True Positive" means that the model predicted a pixel to be Positive (i.e., $\geq$ 0.5, part of F2 trace) and was correct

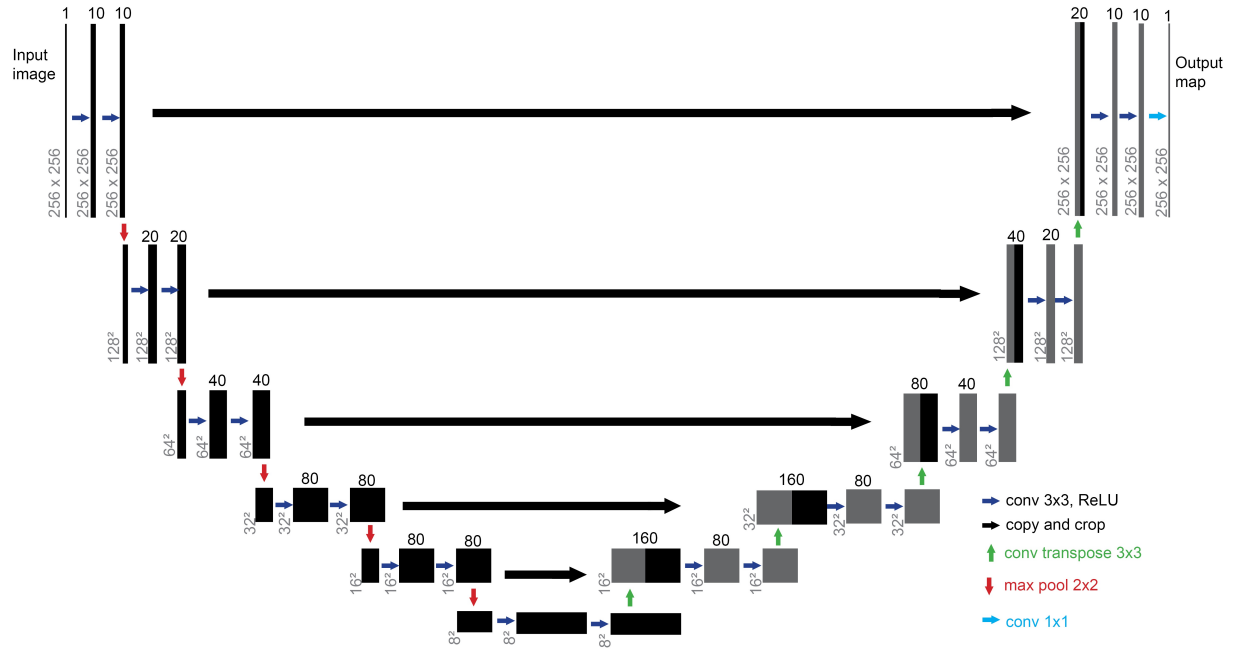

Figure B.2: U-net architecture created by Capt. Tyler Hussey and modeled after the original U-net of Ronneberger (2015). The numbers above each rectangle are the number of filters used for the convolution and the vertical numbers on the bottom left of each rectangle are the dimensions of the output image of the layer.

(i.e., prediction was *True*); False Positive means that the model predicted Negative (i.e., < 0.5, *not* part of F2 trace) and was incorrect, and so on. The Dice coefficient (Equation 2) indicates how close the predicted image is to the mask compared to the similarity of the two by chance Dice (1945). In other words, the dice coefficient is the ratio of twice the intersection of the mask and predicted image to the total pixels in both the mask and predicted image.

$$Dice = \frac{2|A \cap B|}{(|A| + |B|)} = \frac{2TP}{(2TP + FP + FN)} \tag{B.2}$$

B.2.3 Results

The TH model was trained on the original data set of 296 images (with 80/20 train/validation split) until the loss function reached a minimum and stopped decreasing for 25 epochs; this occurred after 500 epochs. The accuracy score for the training and validation sets as well as the loss and validation loss are shown in Figure B.3 (left). As mentioned previously, the accuracy is initially high and converges quickly. A better representation of the learning performance of the model is shown in Figure B.3 (right): the mean IoU and dice coefficients for the training and validation data sets. This shows that after 500 epochs when the loss was no longer decreasing, the validation

Mean IoU (green) and validation Dice score (red) both began to plateau around their maxima from 400-500 epochs. From these training results, 500 was chosen to be the optimal number of training epochs.

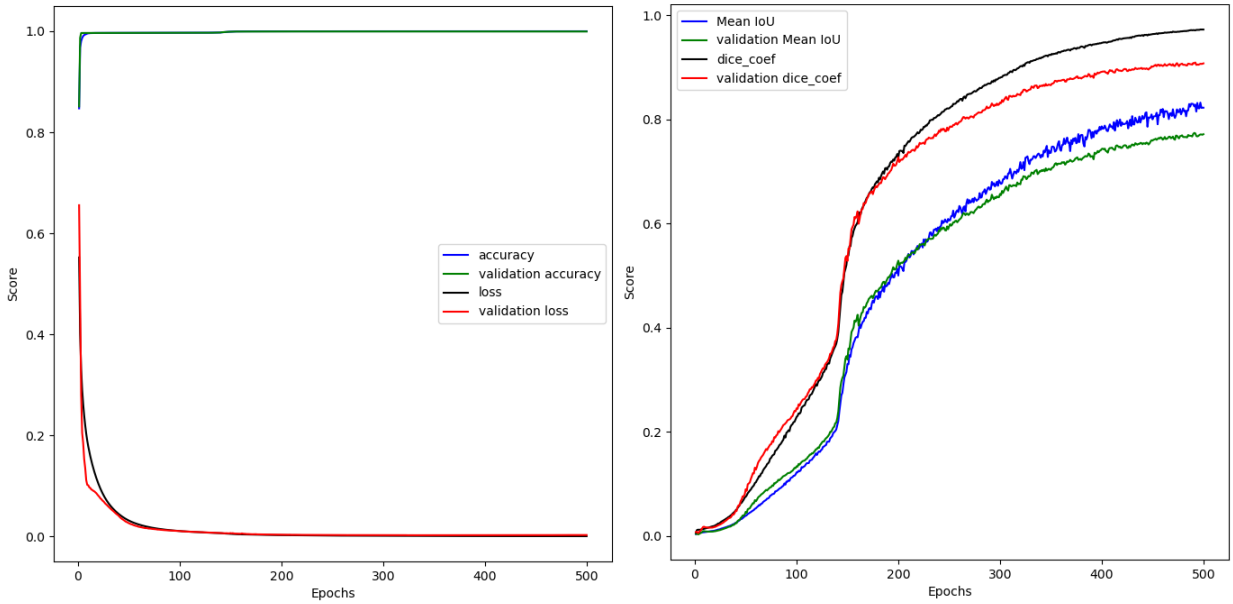

Figure B.3: (Left): Plot of the learning curves of accuracy and loss scores for the training and validation sets for 500 epochs of training the TH model. (Right): Learning curves of Dice and Mean IoU values for training and validation sets for 500 epochs of training.

The model was tested on the full test data set (274 images from T1, T2, T3) as well as on test sets consisting of images for each of the transmitter sites individually. Then, the TH model was trained for 500 epochs on increased training data sets consisting of multiples of 296 up to 5x and tested again on the full test set as well as on the individual transmitter site test sets. The Dice coefficient scores for the full test are compiled in Table B.2 with the scores for the TH model trained on expanded data set multiples (i.e., each multiple training data set contains the same images and masks as the previously trained models with an added 296 samples and an 80/20 train/validation split). Table B.2 shows that for the full test set, the test Dice score increases more than 10% upon doubling the original training data set and then increases in smaller increments from 2x to 5x data sets. The test scores are highest for the T2 test images for all data set multiples; this was expected because the model was trained on images from the T2 transmitter site. The model scored the lowest in all cases for the ionogram images from the T1 site, these scores increase from 1x to 4x training sets and then slightly decrease on the 5x training set.

The differences in test scores observed for each of the transmitter sites is likely due to the secant law: the reflected frequency in an oblique ionogram is shifted from the critical frequency (in a VI

	1x 296	2x	3x	4x	5x
Full test set	0.4966	0.6182	0.6427	0.6618	0.6731
T1	0.0516	0.1609	0.3377	0.4458	0.4241
T2	0.7171	0.7067	0.7133	0.7204	0.7233
T3	0.3304	0.6581	0.6554	0.6628	0.6977

Table B.2: Dice scores for each test set and each model.

ionogram) by a factor of the secant of the incident angle on the ionosphere $sec(\theta_i)$ (Picquenard, 1974). While the rate of change of $sec(\theta_i)$ increases from 0° to 90°, the geometry of oblique ionosonde data collection is such that most ground ranges are far enough away that θ_i is from 85-90° and thus $sec\theta_i$ is within a similar range for most oblique ionograms, but is very different for much smaller values of θ_i (i.e., short-range oblique ionograms).

For example, for a ray path to the bottom-side ionosphere at h = 100 km and a flat ground, beyond a ground range of about 1000 km, the angle of incidence is around 85° or greater. This means that for oblique ionograms with ground ranges beyond about 1000 km, the degree of obliqueness (i.e., the amount of frequency shift) changes much less than it does for ground ranges less than 1000 km. In other words, degree of obliqueness is more similar for ionograms with ground ranges of 1000 km and 10,000 km than for ground ranges of 1000 km and 100 km. The effect of this is observed in the model: the frequencies in the oblique ionogram training set from T2 are more similar to frequencies in the T3 test set than the T1 test set, despite the closer range between T2 and T1. Essentially, the model learns the similarity of the long-range oblique ionograms much more efficiently than the similarity of long-range and short-range oblique ionograms.

The performance on the short-range ionogram images is the primary weakness of the model, this can also be seen in Figure B.4, a plot of the Dice scores for the model trained on each multiple of training data that are listed in Table B.2. The decrease in the T1 Dice value for the 4x model while the test scores on the other sites are still increasing indicates that more short-range or VI ionogram training data is necessary. Because these scores are the lowest of the three transmission sites, adding even 1x more VI or short-range oblique ionogram data could greatly increase the performance of the model overall.

While the model exhibited lower scores for the short-range oblique ionograms from T1, the increase from 1x to 5x training data is still clear from Figure B.4. An example of the actual ionogram image output of the model trained on 5x training data is shown in Figure B.5. Figure B.5 (a) is the original ionogram image from the T1 training set, Figure B.5 (b) is the mask which is the exact pixels from (a) that are part of the target F2 trace and Figure B.5 (c) is the output prediction of the model. Figure B.5 shows that while there are some performance issues with the VI ionogram images, the model still does perform moderately well on classifying the F2 trace.

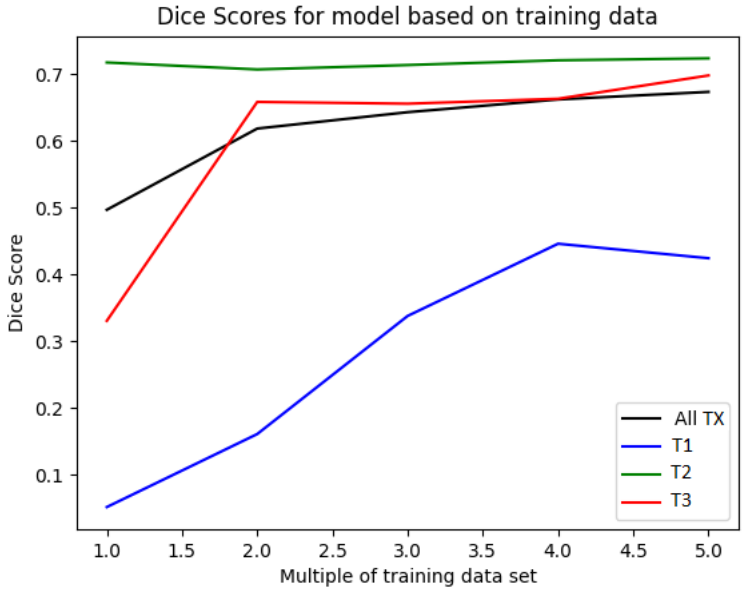

Figure B.4: Plot of the dice scores separated by Full Test Set and the individual transmission sites for each model trained.

Another example of the final model output is shown in Figure B.6, the same format as in Figure B.5, these are ionogram image (a), mask (b), and prediction output (c) for an ionogram from the T2 transmitter site. This ionogram has traces of the F1 layer and the E layer; it shows that not only can the model predict the F2 trace in a short-range ionogram where the only other traces are multiple hop traces of F2, but the model also can distinguish the F2 trace from other ionospheric layer traces in an oblique ionogram. However, the test scores in Table B.4 show that it does not predict every F2 trace in the T2 test set so well, as the final score is only 0.67. There are some cases where the model predicts most but not all of the F2 trace pixels correctly and others where the F2 trace is more ambiguous or the ionogram data are corrupted with noise and the model outputs no F2 trace prediction pixels at all (i.e., a blank output image).

Figure B.5: (a): Original ionogram image from T1 test data set, (b): mask of ionogram image, with only the pixels of original image that are labeled as F2 trace and (c): model output prediction image, with pixels predicted as F2 trace.

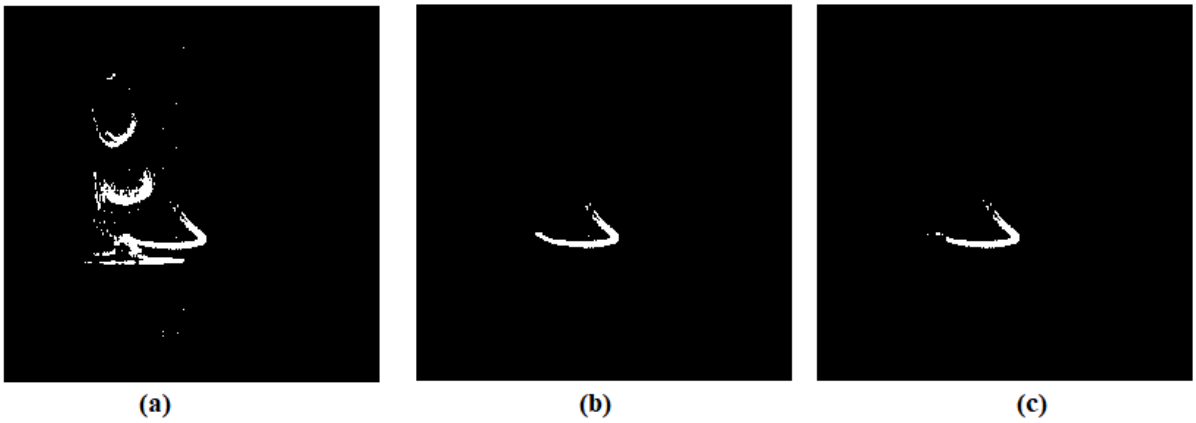

Figure B.6: (a): Original ionogram image from T2 test data set, (b): mask of ionogram image, with only the pixels of original image that are labeled as F2 trace and (c): model output prediction image, with pixels predicted as F2 trace.

B.2.4 Discussion & Conclusions

The goals of this project were to a) determine if the TH U-net model can identify the F2 trace in ionogram image data and find the optimal number of epochs to train the model on a baseline dataset, b) determine how well the model performs on ionogram images with various degrees of obliqueness and c) determine how much added training data is necessary to sufficiently identify the F2 trace in ionograms for any degree of obliqueness. The results outlined above show that the TH model can identify the F2 trace, but the test scores of the model could still be greatly improved.

The test scores on the final model trained on a 5x training set are highest on new ionogram

images that are from the same T2 transmitter site. The test scores on the T3 data are slightly lower but in close range to those of T2, and lowest on the short-range images from the T1 transmitter site. The similar scores of the T2 and T3 site around 0.70 despite the greater distance between the two ($\sim$1600 km) as opposed to T2 and T1 ($\sim$1000 km) indicates that the model has great potential to identify the F2 trace in ionograms images and to do so regardless of the ground range between transmitter and receiver (i.e. degree of obliqueness). It is hypothesized that the final 5x model would perform similarly to the 0.70 test score for ionograms with ground ranges much greater than 2700 km The lower scores of the short-range from T1 and the decrease in the scores from the 4x to 5x model indicates that the model requires more VI and short-range oblique ionogram training data in order to sufficiently identify F2 traces in all ionogram types. Future work on this research project involves adding more short-range and VI training data and then testing the model on ground ranges $<<$1000 km and $>>$2700 km.

Overall, the main goals of this project have been met. This research proves the concept for F2 trace identification with a U-net convolutional neural network architecture, however more training data of both VI and oblique ionogram images are necessary to improve the performance of the model.

APPENDIX C

Chapter 4 Appendix

C.1 Magnetometer Data Availability

Station	2009	2010	2011	2012	2013	2014	2015	2016	2017	2018	2019
IGL	0	0	175	0	0	0	354	293	338	287	337
GJO	0	0	307	0	0	0	327	272	255	0	152
RBY	0	0	299	0	0	0	343	213	343	303	342
PGG	0	0	323	0	0	0	306	185	305	342	345
CDR	0	0	174	0	0	0	343	228	337	334	337
RANK	350	348	336	238	280	352	342	100	361	363	341
YKC	356	361	364	366	365	363	358	344	341	365	178
FCC	85	365	361	362	349	354	360	335	351	349	247
GILL	365	365	358	365	286	353	361	300	362	343	214
WHIT	321	357	333	256	335	364	350	357	219	36	282
ATHA	356	362	365	364	355	358	359	210	323	364	323
MEA	365	365	365	365	365	365	365	355	363	365	200
SALU	-	-	-	-	-	-	-	1	-	-	-
KJPK	-	-	-	-	-	-	-	1	-	-	-

Table C.1: Magnetometer station data availability per year for 2009-2019.

C.2 Other Data Use Acknowledgements

The magnetic footprint of GOES-13 was determined using tools provided by SSCWEB (https://sscweb.gsfc.nasa.gov/).

The OMNI data were obtained from the GSFC/SPDF OMNIWeb interface at https://omniweb.gsfc.nasa.gov.

GOES magnetometer data are available online (https://satdat.ngdc.noaa.gov/sem/goes/data/full/).

C.3 Extended Research: Interhemispheric Comparisons of Large Nighttime Magnetic Perturbation Events Relevant to GICs

In this section, we summarize a study that I was a co-author of titled "Interhemispheric Comparisons of Large Nighttime Magnetic Perturbation Events Relevant to GICs" published in JGR: Space Physics (Engebretson et al., 2020). Then we discuss the relevance of the findings of this study to the results of Chapter 4.

C.3.1 Summary

In this study, four nighttime GMD events observed from 2015-2018 are analyzed using conjugate high-latitude magnetometer stations. The data used are from 1) PGG and IQA in eastern Nunavut, Canada of the MACCS (Engebretson et al., 1995) and CANMOS (Nikitina et al., 2016) programs respectively, paired with the magnetically conjugate south pole station in Antarctica (Engebretson et al., 1997) and 2) the Greenland West Coast Chain (www.space.dtu.dk/MagneticGroundStation) and magnetically conjugate stations in Antarctica of the Autonomous Adaptive Low-Power Instrument Platform (AAL-PIP) chain (Clauer et al., 2014) and the British Antarctic Survey (BAS) Low Power Magnetometer (LPM) chain (Kadokura et al., 2008). The events were identified using the semi-automatic routine described in detail in Engebretson et al. (2019a).

Of the four GMD events, three of them were pre-midnight events and one was a post-midnight event. The pre-midnight GMDs showed fair hemispheric conjugacy in the timing of Bx excursions (which were the largest perturbations for pre-midnight events), latitudinal profiles and amplitude peaks. For the post-midnight interval, highly localized GMDs occurred independently in time over an approximate 1.5 hour period at each station in both hemispheres and the largest amplitude perturbations were in the By component. Auroral images from the DMSP spacecraft (orbiting at $\sim$840 km) were used to confirm the presence of omega bands in the auroras during the post-midnight interval.

Omega band auroral structures resemble an inverted Greek letter, Ω with scale size from a few hundreds to a thousand kilometers (Jorgensen et al., 1999). They generally appear in the morning sector during substorm recovery; they are formed by an eastward-moving ($\sim$1 km/s) train of alternating upward and downward small-scale FAC that causes undulations of the westward electrojet. Thus, a quasi-sinusoidal pulsations embedded in an electrojet bay is the magnetic field response on the ground.

Comparison of magnetic perturbation amplitudes with ionospheric conductances via the AMIE

procedure (Cousins et al., 2015) showed that the GMD amplitudes did not correspond well to the ionospheric conductances, concluding that a current generator model was favored over a voltage generator model as a M-I electrodynamic driver of these events. The current generator model corresponds to the excitation of resonant field line oscillations.

C.3.2 Connection to the Research Presented in Chapter 4

In Chapter 4, we have shown that many of the characteristics of TLA events are similar to that of nighttime GMDs. The magnetic local time dependence of both types of events are very similar, with two distinct populations in the pre- and post-midnight sectors. The dependence on both ring current activity and solar cycle dependence, as well as auroral electrojet activity and the distribution of time delay from substorm onset are all very similar to nighttime GMDs. It is understandable that there are so many shared chatacteristics of nighttime GMDs and TLA events because they often occur concurrently, and/or in the near vicinity of one another.

As one of the key findings of Engebretson et al. (2020) is that conjugate post-midnight GMDs were associated with omega bands, and following from the simultaneity of many TLA and GMD events, it is reasonable to assume that post-midnight TLA events may be associated with auroral omega bands as well. To explore this assumption, we have examined THEMIS ASI data during some of the post-midnight TLA-related GMD events.

Of the set of 33 TLA-related GMD events that occurred from 2015-2019 during the post-midnight interval from midnight to 6 MLT, there were seven events that clearly coincided with omega band structures in the ASI images. An example of one of these events is shown in Figure 1.3; the figure shows magnetic field data at four stations on 17 December, 2017 and TLA dB/dt that occurred at RANK near 06:10 UT preceding GMDs at stations to the north.

The ASI images at RANK for three-second intervals during the minute of 06:10 UT is shown in Figure C.1. These images show a clear omega band structure in the auroras that starts to form in the first second, moves slightly eastward and dissipates by the end of the minute. A separate omega band structure was observed in the minute prior that also dissipated by the start of the interval shown in Figure C.1.

C.3.3 Discussion

Zesta et al. (2000) have shown that there is a one-to-one correlation between PBIs and BBFs in the tail. Henderson et al. (2002) showed that PBIs and auroral streamers can evolve directly into omega bands, suggesting a strong relationship between BBFs and omega bands. The relationship between fast flows and omega bands in the auroras has since been reinforced by Partamies et al. (2017).

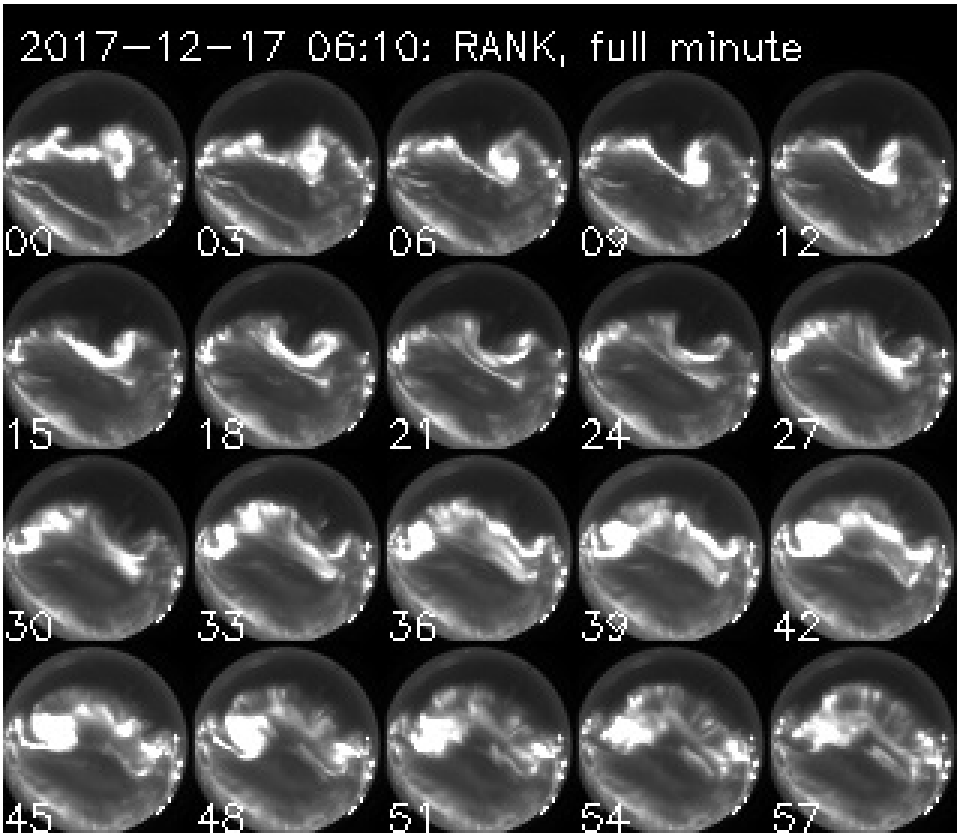

Figure C.1: THEMIS ASI data at the RANK station at from 06:10-06:11 UT on 17 December, 2017.

It is known that Ps6/Pi3 magnetic pulsations (quasi-periodic sequences of GMDs with ∼5-40 minute periods (Opgenoorth et al., 1983)) often accompany omega band structures. Multiple sources have asserted that omega bands and associated Ps6/Pi3 pulsations are very effective at driving large GIC (Kozyreva et al., 2019; Apatenkov et al., 2020; Chinkin et al., 2021). The Engebretson et al. (2020) study summarized in this section gave an example of a post-midnight GMD associated with omega bands; we have presented another example of a GMD with TLA dB/dt intervals that coincides with omega bands in the ionosphere. These results emphasize the relationship between nighttime GMD/TLA events and omega bands in the aurora and reinforce the potential for these events to drive GICs at Earth's surface.

BIBLIOGRAPHY

Akasofu, S. I. (1964). The development of the auroral substorm. *Planetary and Space Science*, 12(4):273–282.

Amm, O. and Viljanen, A. (1999). Ionospheric disturbance magnetic field continuation from the ground to the ionosphere using spherical elementary current systems. *Earth, Planets and Space*, 51(6):431–440.

Angelopoulos, V., Baumjohann, W., Kennel, C. F., Coroniti, F. V., Kivelson, M. G., Pellat, R., Walker, R. J., Lühr, H., and Paschmann, G. (1992). Bursty bulk flows in the inner central plasma sheet. *Journal of Geophysical Research*, 97:4027.

Apatenkov, S. V., Pilipenko, V. A., Gordeev, E. I., Viljanen, A., Juusola, L., Belakhovsky, V. B., Sakharov, Y. A., and Selivanov, V. N. (2020). Auroral Omega Bands are a Significant Cause of Large Geomagnetically Induced Currents. *Geophysical Research Letters*, 47(6):1–8.

Arnoldy, R. L., Rajashekar, R., Cahill, L. J., Engebretson, M. J., Rosenberg, T. J., and Mende, S. B. (1987). Simultaneous measurement of aurora-related, irregular magnetic pulsations at northern and southern high latitudes. *Journal of Geophysical Research*, 92(A11):12221.

Atkinson, G. (1967). The current system of geomagnetic bays. *Journal of Geophysical Research*, 72:6063–6067.

Baumjohann, W. and Glassmeier, K. H. (1984). The Transient Response Mechanism and Pi2 Pulsations at Substorm Onset- Review and Outlook.

Belakhovsky, V., Pilipenko, V., Engebretson, M., Sakharov, Y., and Selivanov, V. (2019). Impulsive disturbances of the geomagnetic field as a cause of induced currents of electric power lines. *Journal of Space Weather and Space Climate*, 9:1–19.

Birn, J. and Hesse, M. (2014). The substorm current wedge: Further insights from MHD simulations. *Journal of Geophysical Research: Space Physics*, 119(5):3503–3513.

Bobra, M. G. and Couvidat, S. (2015). Solar flare prediction using SDO/HMI vector magnetic field data with a machine-learning algorithm. *Astrophysical Journal*, 798(2).

Bolduc, L., Langlois, P., Boteler, D., and Pirjola, R. (1998). A study of geoelectromagnetic disturbances in Québec, 1. General results. *IEEE Transactions on Power Delivery*, 13:1251–1256.

Borovsky, J. E. and Yakymenko, K. (2017). Substorm occurrence rates, substorm recurrence times, and solar wind structure. *Journal of Geophysical Research: Space Physics*, 122:2973–2998.

Boteler, D. H. (2006). The super storms of August/September 1859 and their effects on the telegraph system. 38(September 1859):159–172.

Boteler, D. H. (2019). A 21st Century View of the March 1989 Magnetic Storm. *Space Weather*, 17:1427–1441.

Boteler, D. H. and Beek, G. J. V. (1999). August 4, 1972 revisted: A new look at the geomagnetic disturbance that caused the L4 cable system outage. *Geophysical Research Letters*, 26(5):577–580.

Boteler, D. H., Pirjola, R. J., and Nevanlinna, H. (1998). The effects of geomagnetic disturbances on electrical systems at the Earth's surface. *Advances in Space Research*, 22(1):17–27.

Breiman, L. (1996). Bagging predictors. *Machine Learning*, (24):123–140.

Breiman, L. (2001). Random Forests. *Machine Learning*, 45:5–32.

Chinkin, V. E., Soloviev, A. A., Pilipenko, V. A., Engebretson, M. J., and Sakharov, Y. A. (2021). Determination of vortex current structure in the high-latitude ionosphere with associated GIC bursts from ground magnetic data. *Journal of Atmospheric and Solar-Terrestrial Physics*, 212(October 2020):105514.

Clauer, C. R., Kim, H., Deshpande, K., Xu, Z., Weimer, D., Musko, S., Crowley, G., Fish, C., Nealy, R., Humphreys, T. E., Bhatti, J. A., and Ridley, A. J. (2014). An autonomous adaptive low-power instrument platform (AAL-PIP) for remote high-latitude geospace data collection. *Geoscientific Instrumentation, Methods and Data Systems*, 3(2):211–227.

Connors, M., Schofield, I., Reiter, K., Chi, P. J., Rowe, K. M., and Russell, C. T. (2016). The AUTUMNX magnetometer meridian chain in Québec, Canada. *Earth, Planets and Space*, 68(1).

Cortes, C. and Vapnik, V. (1995). Support-Vector Networks. *Machine Learning*, (20):273–297.

Cousins, E. D., Matsuo, T., and Richmond, A. D. (2015). Mapping high-latitude ionospheric electrodynamics with SuperDARN and AMPERE. *Journal of Geophysical Research: Space Physics*, 120(7):5854–5870.

Dice, L. R. (1945). Measures of the Amount of Ecologic Association Between Species. *Ecology*, 26:297–302.

Dimmock, A. P., Rosenqvist, L., Welling, D. T., Viljanen, A., Honkonen, I., Boynton, R. J., and Yordanova, E. (2020). On the Regional Variability of dB/dt and Its Significance to GIC. *Space Weather*, 18(8):1–20.

Engebretson, M. J. (2023). Solar Cycle Dependence of Very Large Nighttime Geomagnetic Disturbances (GMDs) Observed in Eastern Arctic Canada: Data [Data set]. *University of Michigan - Deep Blue Data*.

Engebretson, M. J., Araki, T., Arnoldy, R. L., Carpenter, D. L., Doolittle, J. H., and Fukunishi, H., e. a. (1997). The United States automatic geophysical observatory (AGO) program in Antarctica. In M. Lockwood, M. N. Wild, H. J. Opgenoorth (Eds.). *ESA-SP-1198*, pages 65–99.

Engebretson, M. J., Cahill, L. J., Arnoldy, R. L., Mende, S. B., and Rosenberg, T. J. (1983). Correlated Irregular Magnetic Pulsatoins and Optical Emissions Observed at Siple Station, Antarctica. 88:4841–4852.

Engebretson, M. J., Hughes, W. J., Alford, J. L., Zesta, E., Cahill, L. J., Arnoldy, R. L., and Reeves, G. D. (1995). Magnetometer array for cusp and cleft studies observations of the spatial extent of broadband ULF magnetic pulsations at cusp/cleft latitudes. *Journal of Geophysical Research*, 100(A10):19371.

Engebretson, M. J., Kirkevold, K. R., Steinmetz, E. S., Pilipenko, V. A., Moldwin, M. B., McCuen, B. A., Clauer, C. R., Hartinger, M. D., Coyle, S., Opgenoorth, H., Schillings, A., Willer, A. N., Edwards, T. R., Boteler, D. H., Gerrard, A. J., Freeman, M. P., and Rose, M. C. (2020). Interhemispheric Comparisons of Large Nighttime Magnetic Perturbation Events Relevant to GICs. *Journal of Geophysical Research: Space Physics*, 125(8):1–24.

Engebretson, M. J., Lessard, M. R., Bortnik, J., Green, J. C., Horne, R. B., Detrick, D. L., Weatherwax, A. T., Manninen, J., Petit, N. J., Posch, J. L., and Rose, M. C. (2008). Pc1-Pc2 waves and energetic particle precipitation during and after magnetic storms: Superposed epoch analysis and case studies. *Journal of Geophysical Research: Space Physics*, 113.

Engebretson, M. J., Pilipenko, V. A., Ahmed, L. Y., Posch, J. L., Steinmetz, E. S., Moldwin, M. B., Connors, M. G., Weygand, J. M., Mann, I. R., Boteler, D. H., Russell, C. T., and Vorobev, A. V. (2019a). Nighttime Magnetic Perturbation Events Observed in Arctic Canada: 1. Survey and Statistical Analysis. *Journal of Geophysical Research: Space Physics*, 124(9):7442–7458.

Engebretson, M. J., Pilipenko, V. A., Steinmetz, E. S., and Moldwin, M. B. (2021). Nighttime magnetic perturbation events observed in Arctic Canada: 3. Occurrence and amplitude as functions of magnetic latitude, local time, and magnetic disturbance indices.

Engebretson, M. J., Steinmetz, E. S., Posch, J. L., Pilipenko, V. A., Moldwin, M. B., Connors, M. G., Boteler, D. H., Mann, I. R., Hartinger, M. D., Weygand, J. M., Lyons, L. R., Nishimura, Y., Singer, H. J., Ohtani, S., Russell, C. T., Fazakerley, A., and Kistler, L. M. (2019b). Nighttime Magnetic Perturbation Events Observed in Arctic Canada: 2. Multiple-Instrument Observations. *Journal of Geophysical Research: Space Physics*, 124(9):7459–7476.

Engebretson, M. J., Zanetti, L., Potemra, T., Baumjogann, W., Luhr, H., and Acuna, M. (1987). Simultaneous observations of Pc3-4 pulsations in the solar wind and in the Earth's magnetosphere. *Journal of Geophysical Research*.

Finley, M. G., Bowen, T. A., Pulupa, M., Koval, A., and Miles, D. M. (2023). Statistical Decomposition and Machine Learning to Clean In-Situ Spaceflight Magnetic Field Measurements.

Gannon, J. L., Birchfield, A. B., Shetye, K. S., and Overbye, T. J. (2017). A Comparison of Peak Electric Fields and GICs in the Pacific Northwest Using 1-D and 3-D Conductivity. *Space Weather*, 15:1535–1547.

Gao, Y. F., Chi, P. J., Le, G., Russell, C. T., Yang, D. M., Zhou, X., Yang, S. F., Angelopoulos, V., and Chun, F. K. (2000). Sino-Magnetic Array at Low Latitudes (SMALL) including initial results from the sister sites in the United States. *Advances in Space Research*, 25(7-8):1343–1351.

Gjerloev, J. W. (2012). The SuperMAG data processing technique. *Journal of Geophysical Research: Space Physics*, 117(9):1–19.

Gosling, J. T. (1993). The solar flare myth. *Journal of Geophysical Research*, 98.

Goss, H. (Published on 28 July 2020.). The Rise of Machine Learning. *Eos*, 101.

Grawe, M. A., Makela, J. J., Butala, M. D., and Kamalabadi, F. (2018). The Impact of Magnetic Field Temporal Sampling on Modeled Surface Electric Fields. *Space Weather*, 16:1721–1739.

Hajra, R. and Sunny, J. V. (2022). Corotating Interaction Regions during Solar Cycle 24: A Study on Characteristics and Geoeffectiveness. *Solar Physics*, 297.

Heacock, R. R. and Hunsucker, R. D. (1981). Type Pi 1-2 Magnetic Field Pulsations.

Heidke, P. (1926). Berechnung Des Erfolges Und Der Güte Der Windstärkevorhersagen Im Sturmwarnungsdienst. *Geografiska Annaler*, 8(4):301–349.

Henderson, M. G., Kepko, L., Spence, H. E., Connors, M., Sigwarth, J. B., Frank, L. A., Singer, H. J., and Yumoto, K. (2002). The evolution of north-south aligned auroral forms into auroral torch structures: the generation of omega bands and Ps6 pulsations via flow bursts.

Henderson, M. G., Reeves, G. D., and Murphree, J. S. (1998). Are north-south aligned auroral structures an ionospheric manifestation of bursty bulk flows? *Geophysical Research Letters*, 25(19):3737–3740.

Herman, J. R. (1966). Spread F and ionospheric F-region irregularities. *Reviews of Geophysics*, 4:255–299.

Hoffmann, A. P. and Moldwin, M. B. (2022). Separation of Spacecraft Noise From Geomagnetic Field Observations Through Density-Based Cluster Analysis and Compressive Sensing. *Journal of Geophysical Research: Space Physics*, 127.

Hughes, W. and Engebretson, M. (1997). MACCS: Magnetometer array for cusp and cleft studies. *Satellite - Ground Based Coordination Sourcebook. ESA SP-1198*, (1):119.

Ieda, A., Nishimura, Y., Miyashita, Y., Angelopoulos, V., Runov, A., Nagai, T., Frey, H. U., Fairfield, D. H., Slavin, J. A., Vanhamäki, H., Uchino, H., Fujii, R., Miyoshi, Y., and Machida, S. (2016). Stepwise tailward retreat of magnetic reconnection: THEMIS observations of an auroral substorm. *Journal of Geophysical Research: Space Physics*, 121(5):4548–4568.

Jaccard, P. (1912). The Distribution of the Flora in the Alpine Zone. *New Phytologist*, 11(2):37–50.

Jacobs, J. A., Kato, Y., Matsushita, S., and Troitskaya, V. A. (1964). Classification of Geomagnetic Micropulsations. *Journal of Geophysical Research*, 69(1):180–181.

Jacobs, J. A., Kato, Y., Matsushita, S., and Troitskaya, V. A. (1994). Classification of Geomagnetic Micropulsations. *Journal of Geophysical Research*, 69(1):180–181.

Jorgensen, A. M., Spence, H. E., Hughes, T. J., and McDiarmid, D. (1999). A study of omega bands and Ps6 pulsations on the ground, at low altitude and at geostationary orbit. *Journal of Geophysical Research: Space Physics*, 104(A7):14705–14715.

Kadokura, A., Yamagishi, H., Sato, N., Nakano, K., and Rose, M. C. (2008). Unmanned magnetometer network observation in the 44th Japanese Antarctic Research Expedition: Initial results and an event study on auroral substorm evolution. *Polar Science*, 2(3):223–235.

Kappenman, J. G. (2005). An overview of the impulsive geomagnetic field disturbances and power grid impacts associated with the violent Sun-Earth connection events of 29-31 October 2003 and a comparative evaluation with other contemporary storms. *Space Weather*, 3(8).

Kappenman, J. G. (2006). Great geomagnetic storms and extreme impulsive geomagnetic field disturbance events - An analysis of observational evidence including the great storm of May 1921. *Advances in Space Research*, 38(2):188–199.

Kataoka, R. and Ngwira, C. (2016). Extreme geomagnetically induced currents.

Keiling, A. (2009). Alfvén waves and their roles in the dynamics of the Earth's magnetotail: A review. *Space Science Reviews*, 142:73–156.

Kepko, L. and Kivelson, M. (1999). Generation of Pi2 pulsations by bursty bulk flows. *Journal of Geophysical Research: Space Physics*, 104(A11):25021–25034.

Kepko, L., Kivelson, M. G., and Yumoto, K. (2001). Flow bursts, braking, and Pi2 pulsations. *Journal of Geophysical Research: Space Physics*, 106(A2):1903–1915.

Khomutov, S. Y., Mandrikova, O. V., Budilova, E. A., Arora, K., and Manjula, L. (2017). Noise in raw data from magnetic observatories. *Geoscientific Instrumentation, Methods and Data Systems*, 6(2):329–343.

King, J. and Papitashvili, N. E. (2020). OMNI 1-min Data Set [Data set]. *NASA Space Physics Data Facility*.

Kivelson, M. G. and Russel, C. T. (1995). *Introduction to Space Physics*. Cambridge University Press.

Kozyreva, O., Pilipenko, V., Krasnoperov, R., Baddeley, L., Sakharov, Y., and Dobrovolsky, M. (2019). Fine structure of substorm and geomagnetically induced currents. *Annals of Geophysics*, 62(June).

Le, G., Slavin, J. A., and Strangeway, R. J. (2010). Space Technology 5 observations of the imbalance of regions 1 and 2 field-aligned currents and its implication to the cross-polar cap Pedersen currents. *Journal of Geophysical Research: Space Physics*, 115(A7):1–14.

Lessard, M. R., Lund, E. J., Jones, S. L., Arnoldy, R. L., Posch, J. L., Engebretson, M. J., and Hayashi, K. (2006). Nature of Pi1B pulsations as inferred from ground and satellite observations. *Geophysical Research Letters*, 33(14):7–10.

Lester, M., Hughes, J., and Singer, H. J. (1983). Polarization Patterns of Pi 2 magnetic Pulsations and the Substorm Current Wedge. *Journal of Geophysical Research*, 88(A10):7958–7966.

Liemohn, M. W., McCollough, J. P., Jordanova, V. K., Ngwira, C. M., Morley, S. K., Cid, C., Tobiska, W. K., Wintoft, P., Ganushkina, N. Y., Welling, D. T., Bingham, S., Balikhin, M. A., Opgenoorth, H. J., Engel, M. A., Weigel, R. S., Singer, H. J., Buresova, D., Bruinsma, S., Zhelavskaya, I. S., Shprits, Y. Y., and Vasile, R. (2018). Model Evaluation Guidelines for Geomagnetic Index Predictions. *Space Weather*, 16(12):2079–2102.

Liu, J., Angelopoulos, V., Chu, X., Zhou, X. Z., and Yue, C. (2015). Substorm current wedge composition by wedgelets. *Geophysical Research Letters*, 42(6):1669–1676.

Liu, J., Angelopoulos, V., Runov, A., and Zhou, X. Z. (2013). On the current sheets surrounding dipolarizing flux bundles in the magnetotail: The case for wedgelets. *Journal of Geophysical Research: Space Physics*, 118(5):2000–2020.

Liu, J., Angelopoulos, V., Yao, Z., Chu, X., Zhou, X. Z., and Runov, A. (2018a). The Current System of Dipolarizing Flux Bundles and Their Role as Wedgelets in the Substorm Current Wedge. pages 323–337.

Liu, J., Lyons, L. R., Archer, W. E., Gallardo-Lacourt, B., Nishimura, Y., Zou, Y., Gabrielse, C., and Weygand, J. M. (2018b). Flow Shears at the Poleward Boundary of Omega Bands Observed During Conjunctions of Swarm and THEMIS ASI. *Geophysical Research Letters*, 45(3):1218–1227.

Love, J. J. and Finn, C. A. (2017). Real-time geomagnetic monitoring for space weather-related applications: Opportunities and challenges. *Space Weather*, 15(7):820–827.

Lyons, L. R., Nishimura, Y., Xing, X., Runov, A., Angelopoulos, V., Donovan, E., and Kikuchi, T. (2012). Coupling of dipolarization front flow bursts to substorm expansion phase phenomena within the magnetosphere and ionosphere. *Journal of Geophysical Research: Space Physics*, 117(2):1–16.

Mann, I. R., Milling, D. K., Rae, I. J., Ozeke, L. G., Kale, A., Kale, Z. C., Murphy, K. R., Parent, A., Usanova, M., Pahud, D. M., Lee, E. A., Amalraj, V., Wallis, D. D., Angelopoulos, V., Glassmeier, K. H., Russell, C. T., Auster, H. U., and Singer, H. J. (2008). The upgraded CARISMA magnetometer array in the THEMIS era. *Space Science Reviews*, 141:413–451.

McCuen, B. A., Moldwin, M. B., and Engebretson, M. (2021). Characterization of Transient-Large-Amplitude Geomagnetic Perturbation Events. *Geophysical Research Letters*, 48(15).

McCuen, B. A., Moldwin, M. B., Engebretson, M. J., Weygand, J. M., and Nishimura, Y. (2023a). Magnetosphere-Ionosphere Drivers of Transient-Large-Amplitude Geomagnetic Disturbances: Statistical Analysis and Event Study. *Submitted to: Journal of Geophysical Research: Space Physics*.

McCuen, B. A., Moldwin, M. B., Steinmetz, E. S., and Engebretson, M. J. (2023b). Automated High-Frequency Geomagnetic Disturbance Classifier: A Machine Learning Approach to Identifying Noise While Retaining High-Frequency Components of the Geomagnetic Field. *Journal of Geophysical Research: Space Physics*, 128.

McGranaghan, R. M., Mannucci, A. J., Wilson, B., Mattmann, C. A., and Chadwick, R. (2018). New Capabilities for Prediction of High-Latitude Ionospheric Scintillation: A Novel Approach With Machine Learning. *Space Weather*, 16(11):1817–1846.

McPherron, R. L. (1979). Magnetospheric Substorms. *Reviews of Geophysics*, 17(4):657–681.

McPherron, R. L. (2005). Magnetic pulsations: Their sources and relation to solar wind and geomagnetic activity. *Surveys in Geophysics*, 26(5):545–592.

McPherron, R. L., Russell, C. T., and Aubry, M. P. (1973). Satellite studies of magnetospheric substorms on August 15, 1968: 9. Phenomenological model for substorms. *Journal of Geophysical Research*, 78(16):3131–3149.

Milling, D. K., Rae, I. J., Mann, I. R., Murphy, K. R., Kale, A., Russell, C. T., Angelopoulos, V., and Mende, S. (2008). Ionospheric localisation and expansion of long-period Pi1 pulsations at substorm onset. 35:3–7.

Mitchell, T. (1997). *Machine Learning*, volume 45. McGraw-Hill Science/Engineering/Math.

Mitra, P. P., Araya-polo, M., Byrd, D., and Akhiyarov, D. (2020). Machine Learning-based Anomaly Detection with Magnetic Data.

Nakamura, R., Baumjohann, W., Klecker, B., Bogdanova, Y., Balogh, A., Rème, H., Bosqued, J. M., Dandouras, I., Sauvaud, J. A., Glassmeier, K. H., Kistler, L., Mouikis, C., Zhang, T. L., Eichelberger, H., and Runov, A. (2002). Motion of the dipolarization front during a flow burst event observed by Cluster. *Geophysical Research Letters*, 29(20):2–5.

Nakamura, R., Baumjohann, W., Panov, E., Petrukovich, A. A., Angelopoulos, V., Volwerk, M., Magnes, W., Nishimura, Y., Runov, A., Russell, C. T., Weygand, J. M., Amm, O., Auster, H. U., Bonnell, J., Frey, H., Larson, D., and McFadden, J. (2011). Flux transport, dipolarization, and current sheet evolution during a double-onset substorm. *Journal of Geophysical Research: Space Physics*, 116(5).

Neska, A., Reda, J., Neska, M., and Sumaruk, Y. (2013). On the influence of DC railway noise on variation data from Belsk and Lviv geomagnetic observatories. *Acta Geophysica*, 61(2):385–403.

Newell, P. T. and Gjerloev, J. W. (2011). Evaluation of SuperMAG auroral electrojet indices as indicators of substorms and auroral power. *Journal of Geophysical Research: Space Physics*, 116:1–12.

Newell, P. T. and Gjerloev, J. W. (2012). SuperMAG-based partial ring current indices. *Journal of Geophysical Research: Space Physics*, 117(5):1–15.

Nguyen, N., Muller, P., and Collin, J. (2020). The Statistical Analysis of Noise in Triaxial Magnetometers and Calibration Procedure. *2019 16th Workshop on Positioning, Navigation and Communications (WPNC)*, pages 1–6.

Ngwira, C. M., Pulkkinen, A., McKinnell, L. A., and Cilliers, P. J. (2008). Improved modeling of geomagnetically induced currents in the South African power network. *Space Weather*, 6(11).

Ngwira, C. M., Pulkkinen, A. A., Bernabeu, E., Eichner, J., Viljanen, A., and Crowley, G. (2015). Characteristics of extreme geoelectric fields and their possible causes: Localized peak enhancements. *Geophysical Research Letters*, 42(17):6916–6921.

Ngwira, C. M., Sibeck, D., Silveira, M. V., Georgiou, M., Weygand, J. M., Nishimura, Y., and Hampton, D. (2018). A Study of Intense Local dB/dt Variations During Two Geomagnetic Storms. *Space Weather*, 16(6):676–693.

Nikitina, L., Trichtchenko, L., and Boteler, D. H. (2016). Assessment of extreme values in geomagnetic and geoelectric field variations for Canada. *Space Weather*, 14(7):481–494.

Nishimura, Y., Lyons, L., Zou, S., Angelopoulos, V., and Mende, S. (2010). Substorm triggering by new plasma intrusion: THEMIS all-sky imager observations. *Journal of Geophysical Research: Space Physics*, 115(7):1–14.

Nishimura, Y., Lyons, L. R., Kikuchi, T., Angelopoulos, V., Donovan, E., Mende, S., Chi, P. J., and Nagatsuma, T. (2012). Formation of substorm Pi2: A coherent response to auroral streamers and currents. *Journal of Geophysical Research: Space Physics*, 117(9):1–12.

Oguti, T., Meek, J. H., and Hayashi, K. (1984). Multiple Correlation Between Auroral and Magnetic Pulsations. *Journal of Geophysical Research*, 89(A4):2295–2303.

Opgenoorth, H. J., Oksman, J., Kaila, K. U., Nielsen, E., and Baumjohann, W. (1983). Characteristics of Eastward Drifting Omega Bands in the Morning Sector of the Auroral Oval. *Journal of Geophysical Research*, 88(A11):9171–9185.

Opgenoorth, H. J., Schilling, A., and Hamrin, M. (2020). GIC Drivers- Characteristics of Storm-time Rapid Geomagnetic Variations. *EGU General Assembly 2020*, pages Online, 4–8 May 2020, EGU2020–5667.

Oyedokun, D., Heyns, M., Cilliers, P., and Gaunt, C. T. (2020). Frequency components of geomagnetically induced currents for power system modelling. *2020 International SAUPEC/RobMech/PRASA Conference, SAUPEC/RobMech/PRASA 2020*.

Partamies, N., Weygand, J. M., and Juusola, L. (2017). Statistical study of auroral omega bands. *Annales Geophysicae*, 35(5):1069–1083.

Pedregosa, F., Varoquaux, G., Gramfort, A., Michel, V., Thirion, B., Grisel, O., Blondel, M., Prettenhofer, P., Weiss, R., Dubourg, V., Vanderplas, J., Passos, A., Cournapeau, D., Brucher, M., Perrot, M., and Duchesnay, E. (2011). Scikit-learn: Machine Learning in Python. *Journal of Machine Learning Research*, 12:2825–2830.

Picquenard, A. (1974). *Radio Wave Propagation*. Macmillan Education UK.

Pinto, V. A., Keesee, A. M., Coughlan, M., Mukundan, R., Johnson, J. W., Ngwira, C. M., and Connor, H. K. (2022). Revisiting the Ground Magnetic Field Perturbations Challenge: A Machine Learning Perspective. *Frontiers in Astronomy and Space Sciences*, 9(May):1–13.

Pulkkinen, A., Bernabeu, E., Eichner, J., Viljanen, A., and Ngwira, C. (2015). Regional-scale high-latitude extreme geoelectric fields pertaining to geomagnetically induced currents. *Earth, Planets and Space*, 67(1).

Pulkkinen, A., Bernabeu, E., Thomson, A., Viljanen, A., Pirjola, R., Boteler, D., Eichner, J., Cilliers, P. J., Welling, D., Savani, N. P., Weigel, R. S., Love, J. J., Balch, C., Ngwira, C. M., Crowley, G., Schultz, A., Kataoka, R., Anderson, B., Fugate, D., Simpson, J. J., and MacAlester, M. (2017). Geomagnetically induced currents: Science, engineering, and applications readiness. *Space Weather*, 15(7):828–856.

Pulkkinen, A., Rastätter, L., Kuznetsova, M., Singer, H., Balch, C., Weimer, D., Toth, G., Ridley, A., Gombosi, T., Wiltberger, M., Raeder, J., and Weigel, R. (2013). Community-wide validation of geospace model ground magnetic field perturbation predictions to support model transition to operations. *Space Weather*, 11(6):369–385.

Pulkkinen, A., Viljanen, A., and Pirjola, R. (2006). Estimation of geomagnetically induced current levels from different input data. *Space Weather*, 4(8).

Pulkkinen, T. I. (1996). Pseudobreakup or substorm? *Proceedings of the Third International Conference on Substorms, ESA SP-389*, pages 285–293.

Pulkkinen, T. I., Baker, D. N., Wiltberger, M., Goodrich, C., Lopez, R. E., and Lyon, J. G. (1998). Pseudobreakup and substorm onset: Observations and MHD simulations compared. *Journal of Geophysical Research: Space Physics*, 103(A7):14847–14854.

Rasmussen, C. E. and Williams, C. K. I. (2006). *Gaussian processes for machine learning*. MIT Press.

Reiss, M. A., Möstl, C., Bailey, R. L., Rüdisser, H. T., Amerstorfer, U. V., Amerstorfer, T., Weiss, A. J., Hinterreiter, J., and Windisch, A. (2021). Machine Learning for Predicting the Bz Magnetic Field Component From Upstream in Situ Observations of Solar Coronal Mass Ejections. *Space Weather*, 19(12).

Roldugin, V. C., Roldugin, A. V., and Pilgaev, S. V. (2013). Pc1-2 auroral pulsations. *Journal of Geophysical Research: Space Physics*, 118:74–81.

Ronneberger, O., Fischer, P., and Brox, T. (2015). U-Net: Convolutional Networks for Biomedical Image Segmentation. *IEEE Access*, 9:16591–16603.

Rooney, W. J. and Sherman, K. L. (1934). Earth-current measurements at the College-Fairbanks Polar-Year Station. *Terrestrial Magnetism and Atmospheric Electricity*, 39(3):187–199.

Russell, C. T., Chi, P. J., Dearborn, D. J., Ge, Y. S., Kuo-Tiong, B., Means, J. D., Pierce, D. R., Rowe, K. M., and Snare, R. C. (2008). THEMIS ground-based magnetometers. *Space Science Reviews*, 141(1-4):389–412.

Russell, C. T. and Mcpherron, R. L. (1973). The Magnetotail and Substorms. *Space Science Reviews*, 15:205–266.

Santarelli, L., Palangio, P., and De Lauretis, M. (2014). Electromagnetic background noise at L'Aquila Geomagnetic Observatory. *Annals of Geophysics*, 57(2).

Sergeev, V. A., Liou, K., Meng, C. I., Newell, P. T., Brittnacher, M., Parks, G., and Reeves, G. D. (1999). Development of auroral streamers in association with localized impulsive injections to the inner magnetotail. *Geophysical Research Letters*, 26(3):417–420.

Song, Y.-y. and Lu, Y. (2015). Decision tree methods: applications for classification and prediction.

St-louis, C. B., Rasson, J., Schwarz, G., and Shanahan, T. (2014). INTERMAGNET Technical Note. pages 1–7.

Suthaharan, S. (2016). *Machine Learning Models and Algorithms for Big Data Classification*. Springer.

Tõth, G., Meng, X., Gombosi, T. I., and Rastätter, L. (2014). Predicting the time derivative of local magnetic perturbations. *Journal of Geophysical Research: Space Physics*, 119(1):310–321.

Tsai, L. C. and Berkey, F. T. (2000). Ionogram analysis using fuzzy segmentation and connectedness techniques. *Radio Science*, 35:1173–1186.

Viljanen, A. (1997). The relation between geomagnetic variations and their time derivatives and implications for estimation of induction risks. *Geophysical Research Letters*, 24(6):631–634.

Viljanen, A. (1998). Relation of geomagnetically induced currents and local geomagnetic variations. *IEEE Transactions on Power Delivery*, 13(4):1285–1290.

Walker, A. D. (1981). The Kelvin-Helmholtz instability in the low-latitude boundary layer. *Planetary and Space Science*, 29(10):1119–1133.

Wei, D., Dunlop, M. W., Yang, J., Dong, X., Yu, Y., and Wang, T. (2021). Intense dB/dt Variations Driven by Near-Earth Bursty Bulk Flows (BBFs): A Case Study. *Geophysical Research Letters*, 48(4).

Weygand, J. M., Amm, O., Viljanen, A., Angelopoulos, V., Murr, D., Engebretson, M. J., Gleisner, H., and Mann, I. (2011). Application and validation of the spherical elementary currents systems technique for deriving ionospheric equivalent currents with the North American and Greenland ground magnetometer arrays. *Journal of Geophysical Research: Space Physics*, 116(3):1–8.

Weygand, J. M., Engebretson, M. J., Pilipenko, V. A., Steinmetz, E. S., Moldwin, M. B., Connors, M. G., Nishimura, Y., Lyons, L. R., Russell, C. T., Ohtani, S. I., and Gjerloev, J. (2021). SECS Analysis of Nighttime Magnetic Perturbation Events Observed in Arctic Canada. *Journal of Geophysical Research: Space Physics*, 126:1–25.

Whitehead, J. D. (1989). Recent work on mid-latitude and equatorial sporadic-E.

Xu, X., Huang, L., Liu, X., and Fang, G. (2020). DeepMAD: Deep Learning for Magnetic Anomaly Detection and Denoising. *IEEE Access*, 8:121257–121266.

Zesta, E., Lyons, L. R., and Donovan, E. (2000). The auroral signature of Earthward flow bursts observed in the Magnetotail. *Geophysical Research Letters*, 27(20):3241–3244.

Zhang, J. J., Wang, C., and Tang, B. B. (2012). Modeling geomagnetically induced electric field and currents by combining a global MHD model with a local one-dimensional method. *Space Weather*, 10(5):1–11.

Zou, Y., Dowell, C., Ferdousi, B., Lyons, L. R., and Liu, J. (2022). Auroral Drivers of Large dBdt During Geomagnetic Storms. *Space Weather*, 20(11):1–19.